Application of ocean colour data to study the oceanographic and atmospheric features off the southwest coast of India with special reference to upwelling

Thesis submitted to the
Cochin University of Science and Technology

In partial fulfillment of the requirement for the award of the degree of
Doctor of Philosophy
Under the
Faculty of Marine Sciences
By

SHALIN SALEEM (Reg. No. 3635)
Naval Physical and Oceanographic Laboratory
Kochi – 682 021

October 2012

To
Abba and Ummi

DECLARATION

I, Shalin Saleem hereby declare that the Doctoral thesis entitled ***"Application of ocean colour data to study the oceanographic and atmospheric features off the southwest coast of India with special reference to upwelling"*** *is my own work and that, to the best of my knowledge and belief, it contains no material previously published or written by another person nor material which has been accepted for the award of any other degree or diploma from any universities or institutes of higher learning.*

Kochi-21 SHALIN SALEEM
October 2012

भारत सरकार - रक्षा मंत्रालय
रक्षा अनुसंधान तथा विकास संगठन
नौसेना भौतिक तथा समुद्रविज्ञान प्रयोगशाला
तृक्काक्करा डा.घ., कोच्चि - 682 021, भारत
Government of India, Ministry of Defence
Defence Research & Development Organisation
NAVAL PHYSICAL & OCEANOGRAPHIC LABORATORY
Thrikkakara P.O. , Kochi – 682 021, India

Phone : 0484 - 2571000
Fax : 0484 - 2424858
E-mail : sanilkv@npol.drdo.in

CERTIFICATE

This is to certify that this thesis entitled ***“Application of ocean colour data to study the oceanographic and atmospheric features off the southwest coast of India with special reference to upwelling”*** *is an authentic record of research work carried out by Ms. Shalin Saleem (Reg. No. 3635) under my supervision and guidance at Naval Physical and Oceanographic Laboratory, Kochi-21, towards the partial fulfilment of the requirements for the award of Ph. D degree of the Cochin University of Science and Technology in the faculty of Marine Sciences and that no part thereof has previously formed the basis for the award of any degree, diploma or associateship in any university.*

Kochi – 682 021
16 October 2012

Dr. KV Sanil Kumar
Scientist – ‘F’
(Supervising Guide)

Acknowledgments

In the name of the most merciful and graceful almighty, I acknowledge those special names without which this endeavour would not have been possible.

*First and foremost, I express my sincere gratitude to **Dr. KV Sanil Kumar, Scientist, NPOL**, for his expert guidance, suggestions and encouragement throughout the tenure of this study. Without his timely advice in the proper order the completion of this work would not have been materialised. Indeed, it is my honour to be his student.*

*The work was carried out under NPOL / SAC – II Project with funding from **Space Application Centre (SAC), Ahmedabad**. I am thankful to SAC for providing **research fellowship**.*

*I express my sincere thanks to **Mr. Anantha Narayanan, Director, NPOL; Dr. CV K. Prasada Rao, Associate Director, NPOL** for providing necessary facilities.*

I thank data centers of ocean colour, APDRC, SSMI, PODAAC, AVISO for providing data on ocean colour data, SST, surface current, surface wind, SSH in the public domain, which are utilised in this work. Thanks are due to the Officers and crew of INS Sagardhwani and Scientists from NPOL, who toiled at sea to collect in situ data sets, which are also utilised in this work. I also thank Ocean colour site for SeaDAS software, Air Resource Laboratory, NOAA for providing HYSPLIT and Giovanni site for GOCART.

*I also thank my Doctoral Committee members for their valuable suggestions. I'm grateful to **Dr. K K Balachandran,** Scientist, NIO, Kochi; Dr. C V K Prasada Rao, Associate Director, NPOL and Dr. Harikrishnan, Scientist, NPOL for critically reviewing my thesis.*

*I express my heartful gratitude from the very bottom of my heart to all Officers and staff of NPOL for the love and help they extended during the past three years. **Mr. Suseelan P.**, NPOL is acknowledged for his immense help in conducting the Ph. D. Qualifying examination. Thanks are also due to **Mr. Naveen Das T P, Mr. Mohanan T K, Mr. Balachandran K P, Mr. Subish P S**, **Mr. Sanjay Bharti, Dr. Sunil T**; Dr. Shukla R K and Manas Kumar Das for providing me a conducive environment to carry out research . I thank each and every person who had directly or indirectly helped me to complete this thesis in time.*

*Dr. Roland Draxler, NOAA is acknowledged for clarifying my doubts regarding the HYSPLIT model. I am grateful to Mr. Golla Nagasewara Rao for providing ferret software and support for its execution. My gratitude extends to **Mr. Rajeevan K**, JRF, IIT Delhi, Sreekala P P, JRF, IISC, Rajesh P V, Himansu Pradhan, JRF, IIT Delhi, for their help in providing* *reference materials. I thank Mr. Sivaprasad, Research Scholar, CUSAT for information on HYSPLIT model. I'm also thankful to my colleagues* ***Ms. Shyni T N****, Ms. Sudha A K,* ***Ms. Anoopa Prasad C.****, Mr. Umesh P A, Mr. Pramod V P and Chinnu S for their kindness and support during the tenure.*

The most important blessing to me is my parents ***Abba*** *(my father) and* ***Ummi*** *(my mother), without their support and encouragement it would have been impossible even to think of this endeavour. I am greatly indebted to Shiraz (my brother) and all other family members who always prayed for me and gave their generous support.*

SHALIN SALEEM

Acronyms and abbreviations

ADEOS	ADvanced Earth Observing Satellite
AOD	Aerosol Optical Depth
AQUA	a NASA Earth Satellite
AVHRR	Advanced Very High Resolution Radiometer, space-borne sensor
AVISO	Archiving, Validation and Interpretation of Satellite Oceanographic data (France)
‘c’	Beam attenuation coefficient
Chl *a*	Chlorophyll ‘a’
Chl *a* / K_d	Chl *a* and diffuse attenuation coefficient
Chl_M	Chl *a* of MODIS_AQUA
Chl_S	Chl *a* of SeaWiFS
CMODIS	Chinese Moderate Resolution Imaging Spectroradiometer
CNES	Centre National d’Etudes Spatiales (National Center for Space Studies, France)
CNSA	China National Space Administration
COCTS	Chinese Ocean Colour and Temperature Scanner
COMS	Communication, Ocean and Meteorological Satellite
CTD	Conductivity-Temperature-Depth
CZCS	Coastal Zone Colour Scanner
CZI	Coastal Zone Imager, it is a multispectral pushbroom CCD instrument
DAS	Data Assimilation System
DLR	Deutsche Forschungsanstalt für Luft und Raumfahrt (German agency)
DMI	Dipole Mode Index
DOC	Dissolved Organic Carbon
DOD	Department of Defense's
ECMWF	European Centre for Medium-Range Weather Forecasts
EICC	East India Coastal Current
El Nino	A tropical weather phenomenon that warms the surface of the Eastern Pacific Ocean, which affects the global climate
EMD	Empirical Mode Decomposition
ENSO	El Niño/La Niña–Southern Oscillation
ENVISAT	Environmental Satellite
EOS	Earth Observing Satellite
EPTOMS	Earth Probe Total Ozone Mapping Spectrometer
err %	error percentage
ERS	European Remote sensing Satellite
ERSST.v3b	Extended Reconstructed Sea Surface Temperature, provided by NOAA
ESA	European Space Agency
FOV	Field Of View
FY	Feng Yun (Wind and cloud) name of satellite (China)
GAC	Global Area Coverage

GLI	Global Imager
GOCART	Goddard Global Ozone Chemistry Aerosol Radiation and Transport
GOCI	Geostationary Ocean Color Imager
GPS	Global Positioning System
HDF	Hierarchical Data Format
HICO	Hyperspectral Imager for the Coastal Ocean
HY	Haiyang (Ocean) Satellite (China)
hPa	hectoPascal
HYSPLIT	Hybrid Single-Particle Lagrangian Integrated Trajectory
IMF	Intrinsic Mode Functions
In situ	latin phrase which translates literally to ‘In position’
IOD	Indian Ocean Dipole
IR	Infra-Red
IRS	Indian Remote Sensing Satellite
ISRO	Indian Space Research Organisation
JAMSTEC	Japan Agency for Marine-earth Science and TEChnology
JASON	TOPEX follow-on (not abbreviation)
JEM-EF	Japanese Experiment Module- Exposed Facility
KARI	Korea Aerospace Research Institute
K_d	Diffuse attenuation coefficient
Kd_M	Diffuse attenuation coefficient of MODIS_AQUA
Kd_S	Diffuse attenuation coefficient of SeaWiFS
KOMPSAT	KOrea Multi-Purpose SATellite
KORDI	Korea Ocean Research & Development Institute
La Nina	coupled ocean-atmosphere phenomenon that is the counterpart of El Nino
MERIS	MEdium Resolution Imaging Spectrometer
MERSI	MEdium Resolution Spectral Imager
MISR	Multi-angle Imaging SpectroRadiometer
MLD	Mixed layer Depth
MODIS	MODerate resolution Imaging Spectroradiometer
MODIS_AQUA	MODIS sensor carried on AQUA satellite
MODIS_TERRA	MODIS sensor carried on TERRA satellite
MODTRAN	Program for calculation of atmospheric transmissivity
MOS	Moderate Optoelectrical Scanner
NASA	National Aeronautics and Space Administration (US)
NASDA	National Space Development Agency (Japan)
NCEP / NCAR	National Centers for Environmental Prediction / National Center for Atmospheric Research
NEC	a multinational company formerly called Nippon Electric Co., Ltd. (Japan)
NIOD	Negative Indian Ocean Dipole
NIR	Near Infra-Red
NOAA	National Oceanic and Atmospheric Administration (US)
NOMAD	NASA bio optical Marine Algorithm Data

NPOESS	National Polar orbiting operational Environmental Satellite System
NPP	National Preparatory Project (US)
OCI	Ocean Color Imager
OCM	Ocean Color Monitor
OCTS	Ocean Color Temperature Scanner
ONR	Office of Naval Research
OSMI	Ocean Scanning Multispectral Imager
Parasol	Polarization & Anisotropy of Reflectances for Atmospheric Sciences coupled with Observations from a Lidar
PIOD	Positive Indian Ocean Dipole
POLDER	POLarization and Directionality of the Earth's Reflectances
QuikSCAT	QUIcK SCATterometer, an EOS launched by NASA to estimate wind speed and direction over oceans
r^2	coefficient of determination
RMSD	Root Mean Square Deviations
ROCSAT	Republic of China Satellite
SAC - D	Satelite de Aplicaciones Cientificas – D (Spanish)
SAR	Synthetic Aperture Radar
SeaDAS	SeaWiFS Data Analysis System
SeaWiFS	Sea-viewing Wide Field-of-view Sensor
SETIO	South Eastern Tropical Indian Ocean
SPM	Suspended Particulate Matter
SSHA	Sea Surface Height Anomaly
SST	Sea Surface Temperature
SZ	Shen Zhou satellite (China)
TIROS	Television InfraRed Observation Satellites
TMI	TRMM Microwave Imager
TOPEX	TOPography EXperiment, satellite altimetry mission
VIIRS	Visible Infrared Imager Radiometer Suite
WICC	West India Coastal Current
WTIO	Western Tropical Indian Ocean

Symbols

ε	atmospheric correction parameter
θ	solar viewing angle
λ	Wavelength
$L_A(\lambda)$	radiance due to aerosol
$L_R(\lambda)$	radiance due to Rayleigh
$L_{RA}(\lambda)$	radiance due to mixed Rayleigh-aerosol scattering
$L_T(\lambda)$	Total radiance due to atmospheric interactions, sea surface and subsurface interactions
$L_w(\lambda)$	water leaving radiance
Rrs	Remote sensing reflectance
$tL_f(\lambda)$	reflections whitecaps
$TL_G(\lambda)$	reflections from glint
$tL_w(\lambda)$	radiance backscattered out of the water due to surface interactions
t	diffused atmospheric transmittance
T	direct solar transmittance

TABLE OF CONTENTS

Preface

Satellite remote sensing is being effectively used in monitoring the ocean surface and its overlying atmosphere. Technical growth in the field of satellite sensors has made satellite measurement an inevitable part of oceanographic and atmospheric research. Among the ocean observing sensors, ocean colour sensors make use of visible band of electromagnetic spectrum (shorter wavelength). The use of shorter wavelength ensures fine spatial resolution of these parameters to depict oceanographic and atmospheric characteristics of any region having significant spaio-temporal variability.

Off the southwest coast of India is such an area showing very significant spatio-temporal oceanographic and atmospheric variability due to the seasonally reversing surface winds and currents. Consequently, the region is enriched with features like upwelling, sinking, eddies, fronts, etc. Among them, upwelling brings nutrient-rich waters from subsurface layers to surface layers. During this process primary production enhances, which is measured in ocean colour sensors as high values of Chl *a*. Vertical attenuation depth of incident solar radiation (K_d) and Aerosol Optical Depth (AOD) are another two parameters provided by ocean colour sensors. K_d is also susceptible to undergo significant seasonal variability due to the changes in the content of Chl *a* in the water column. Moreover, K_d is affected by sediment transport in the upper layers as the region experiences land drainage resulting from copious rainfall. The wide range of variability of wind speed and direction may also influence the aerosol source / transport and consequently AOD.

The present doctoral thesis concentrates on the utility of Chl *a*, K_d and AOD provided by satellite ocean colour sensors to understand oceanographic and atmospheric variability off the southwest coast of India. The thesis is divided into six Chapters with further subdivisions.

In the first Chapter, a review on the principle of ocean colour remote sensing and the oceanographic and atmospheric conditions off the southwest coast of India are discussed. The objective of the thesis is also brought out in the Chapter.

Chapter 2 describes various datasets and methodologies used in this study. Global Area Coverage data sets on Chl *a*, K_d and AOD from SeaWiFS (September 1997 – December 2010) and MODIS_AQUA (July 2002 – March 2012) are utilised along with *in situ* SST observations off Kochi during 1998 – 2009. Apart from the above, Sea Surface Height Anomaly (SSHA), ocean surface currents form ship drift observations / ECMWF model, surface winds from NCEP / NCAR and QuikSCAT are also used as supporting data sets.

The spatial distribution of Chl *a*, K_d and AOD off the southwest coast of India on monthly climatological scale is examined in Chapter 3. This Chapter brings out seasonal as well as regional scale variability on these parameters with maximum ranges of the variability during the southwest monsoon period.

The fourth Chapter deals with temporal variability on Chl *a*, K_d and AOD off the southwest coast of India in general and also in two sub-areas of sizes 3^o longitude x 3^o latitude grids and another six areas of still smaller sizes of 0.5^o longitude x 0.5^o latitude grids within the main study area, but geographically different locations. The response of Chl *a*, K_d and AOD anomaly to climatic oscillations are also examined. The variation of aerosol source at surface (1000 hPa) and higher (700 hPa) levels during the specific epochs of climatic oscillations is studied using HYSPLIT model. Various oscillatory modes embedded in time series data of Chl *a*, K_d and AOD are delineated utilising Empirical Mode Decomposition (EMD) method.

Chapter 5 makes an attempt to bring out the underlying relationship between Chl *a* / K_d and Sea Surface Temperature (SST) during the southwest monsoon period off the southwest coast of India and its variability. In this regard, regression analysis is carried out utilising both satellite and *in situ* data sets. The study brings out the feasibility of inverting back the SST from satellite Chl *a* and K_d in the study area.

Finally, the Chapter 6 summarizes the important results and conclusions. Future scope of the study is also highlighted in this Chapter.

LIST OF FIGURES

LIST OF TABLES

Chapter 1

Introduction

Satellite remote sensing is the science of acquiring physical and other environmental information covering large areas utilising onboard sensors. Instant coverage over large area makes satellite data an inevitable source of information, especially the large marine dynamic environment. Thus, satellites are ‘eyes in the sky’ constantly observing the earth and delivering the data as they go round the orbit.

1. 1 Satellite remote sensing of Earth’s surface

The beginning of Earth Observing Satellite (EOS) was with the launch of Television InfraRed Observation Satellites (TIROS-1) by NASA on April 1, 1960. TIROS-1 was designed to capture television images of weather patterns and despite its short period of operation (78 days), it was successful in demonstrating satellite utility for surveying atmospheric conditions. This success paved the way for the launch of many EOS equipped with sensors ranging from fine resolution radar to coarse scatterometers and altimeters. Different types of EOS sensors provides a global ocean picture in terms of Sea Surface Temperature (SST), ocean colour, sea surface winds, sea surface elevation and surface roughness (Martin, 2004). In addition to these parameters, sea surface salinity measurement started with the launch of Aquarius sensor on SAC-D satellite during 10 June 2011 (http://podaac.jpl.nasa.gov).

SST is measured from satellite using Infra-Red (IR) and microwave radiometers. Compared to microwave radiometer, IR provides fine spatial SST (Table

1.1). However, cloud coverage limits IR measurement which is unaffected on microwave radiometers. SST provides a better understanding of regional variability and global climate change. It is an important estimator of heat flux at the air-sea interaction and is used to assess current system, eddies, fronts, upwelling feature and detection of cyclogenesis (Kelkar, 2007).

Scatterometer observation provides sea surface wind speed and direction, which is the major driving source of ocean circulation and generation of waves and surface currents (Table 1.1). It is an important parameter affecting air-sea interaction, upwelling and hence is an input to many numerical models of ocean circulation and wave forecast. In addition to scatterometer data, wind speed from passive microwave aids oceanographic and atmospheric research (Martin, 2004).

Satellite altimeter measurements are used extensively for characterising the ocean surface topography (Table 1.1). These datasets are used to study temporal and spatial scales of ocean variability, eddies, properties of Rossby waves and seafloor topography (Ali, 2003; Fu et al., 2010; Wunsch and Stammer, 1998).

Synthetic Aperture Radar (SAR) provides a variety of information about oceanographic and sea ice processes. SAR images are utilised to identify ocean eddies, surface wave fields, ship wakes, internal waves, surface waves and snow and ice movement (Martin, 2004; Rees, 2005).

Apart from all the above sensors, ocean colour sensors utilises the visible and near infra-red radiance reflected from the sea surface. The sensor captures surface Chlorophyll ‘a’ (Chl *a*), decay matter, particulate organic matter, suspended sediment and light attenuation in addition to the Aerosol Optical Depth (AOD) and Angstorm coefficient of atmosphere (Table 1.1). Among all the passive sensors, ocean colour sensor has the maximum resolution power (250 m), due to the short wavelength of the radiated energy. The resolution of an optical sensor is directly related to its wavelength (Bless, 1996). Hence to resolve finer features, shorter wavelengths are to be used.

Table 1.1. Particulars of various satellite sensors

Passive sensors	Wavelength	Retrieved parameters	Major environmental parameters derived	Maximum available resolution
Ocean colour sensor	0.4-1 µm	Solar radiation reflected from Earth's surface	chlorophyll, suspended sediments, decay matter, attenuation, aerosol optical depth, angstrom coefficient	250 m
Infra-red radiometer	~ 10 µm	Thermal emission of the Earth	SST	1.1 km
Microwave radiometer	1.5-300 mm	Thermal emission of the Earth in microwave	SST, rain rate, snow rate, wind speed	25 km
Active sensors				
Altimeters	3-30GHZ	Travel time of source energy	Sea level	36 km
Scatterometer	3-30GHZ	Change in shape of source wave	Sea surface wind speed and direction	25 km
Synthetic Aperture Radar	3-30GHZ	Change in shape of source wave synthesised from sequential images	Sea surface waves	3 – 100 m

All the parameters derived from ocean colour sensors can be used to study the different features of the oceanic / atmospheric environment (Banse, 1987; Patra et al., 2006; Pradhan et al., 2004; Prasad et al., 2002; Santos, 2010; Sarangi et al. 2005; Shalin and Sanilkumar, 2013; Tassan, 1994; Watts et al., 2005). Many of the civilian / defence applications require high resolution ocean colour data to monitor the ocean properties such as surface currents, eddies, fronts, convergence / divergence zones, etc., where the thermal homogeneity precludes the use of SST. Thus, the application of ocean colour sensor becomes an inevitable part of navy, fisheries, port and ocean engineering (IOCCG, 2007). Since the earth observing system operates in the visible band, the environmental features delineated using ocean colour sensors provide better spatial resolution (Table 1.1).

1. 2 Ocean colour remote sensing

The variations in the magnitude and quality of the radiance reflected from the sea surface are analysed to quantify specific ocean constituents (IOCCG, 2000). Colour of the ocean varies due to the scattering and absorption of visible light with substances or particles present in the upper column of the ocean viz. phytoplankton, suspended sediments and decay matter. Each of these constituents imparts a characteristic feature on the reflected spectrum through absorption or scattering. Thus, the ocean constituents can be estimated from the reflected radiance between specific wavelengths. This information is carried by the water leaving radiance.

While the infra-red and micro-wave radiations have shallow penetration (1-100 micro-m and 1-3 mm), the visible radiance can penetrate 50 – 100 m depending on the water transparency (Martin, 2004). Thus, the water-leaving radiance in the visible band carries information on different constituents, which are utilised in ocean colour radiometry. Since the aerosol and molecular scattering of visible range dominate atmospheric attenuation, the water leaving radiance will be only 10% of the total radiance (Gordon, 1997). This means that removal of atmospheric contribution is crucial for obtaining surface information. Hence, the atmospheric correction plays an important role in ocean colour data processing.

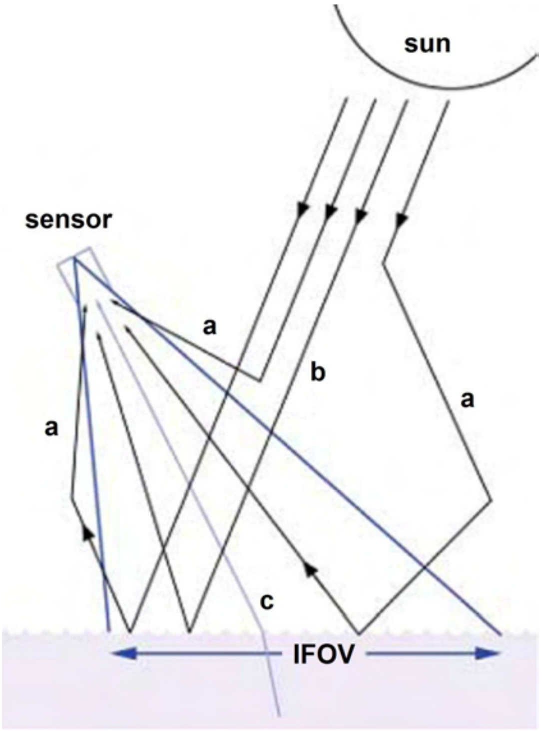

Figure 1.1. Pathways of light reaching the remote sensor. (a) Light scattered in the atmosphere, (b) reflection of direct sunlight at the sea surface, (c) Water leaving radiance. (Modified from IOCCG, 2000)

1.2.1 Atmospheric correction

Atmospheric correction includes the removal of radiances associated with sun glint and foam, ozone attenuation, Rayleigh and aerosol path radiances to yield water leaving radiance from the total radiance measured by the sensor. The reflectance exceeding the preset threshold value of near infra-red (NIR) pixel is classified as cloud and the atmospheric correction is applied for every cloud-free pixel. Each of these components is discussed at the end of this section. However, computation of interference due to aerosol path radiance is very difficult (Martin, 2004).

Total radiance received at the satellite ($L_T(\lambda)$) is the sum of radiance due to atmospheric interactions including Rayleigh, aerosol and mixed Rayleigh-aerosol scattering, surface reflections from sun glint and whitecaps and subsurface interactions and can be represented as

$$L_T(\lambda) = L_R(\lambda) + L_A(\lambda) + L_{RA}(\lambda) + TL_G(\lambda) + t(L_F(\lambda) + L_w(\lambda)), \quad \ldots\ldots (1.1)$$

where, $L_R(\lambda)$, $L_A(\lambda)$ and $L_{RA}(\lambda)$ are respectively the radiance due to Rayleigh, aerosol and mixed Rayleigh-aerosol scattering; $TL_G(\lambda)$ and $tL_F(\lambda)$ are the reflections from glint and whitecaps (T is the direct solar transmittance and t is the diffused atmospheric transmittance); $L_w(\lambda)$ is the water leaving radiance and $tL_w(\lambda)$ is the radiance backscattered out of the water due to surface interactions. Different stages of atmospheric correction are discussed below.

(a) Radiance due to Ozone – Seasonal variation on atmospheric transmittance shows small (~ 0.005) dependence on ozone between the wavelengths 500 and 700 nm. Since, all terms in Eqn(1.1) depend on the solar irradiance, seasonal and latitudinal variation due to ozone should be considered during atmospheric correction. The SeaWiFS and MODIS_AQUA bands utilise the Earth Probe Total Ozone Mapping Spectrometer (EPTOMS) to determine the distribution of ozone and its attenuation (Martin, 2004; http://oceandata.sci.gsfc.nasa.gov/).

(b) Radiance due to sun glint – This refers to the reflection of incoming solar radiation from the ocean surface. In a still ocean surface, the sun glint occurs at one point where the zenith angles between sun and sensor are identical while their azimuth angles are opposite. However, the ocean surface is never flat, as strong surface winds increases the sun glint. Pixels affected by sun glint are to be removed to obtain the real oceanic and atmospheric optical properties. From the SeaWiFS and MODIS_AQUA image, application of the wave facet model allows calculation of the sun glint (Martin, 2004; Wang and Bailey, 2001).

(c) Radiance due to whitecaps – The presence of whitecaps on the ocean surface makes the aerosol radiance estimation more difficult. The whitecap includes foam, streaks and underwater bubbles, but the reflectance decreases substantially in the NIR (Frouin et al. 1996). The surface foam is dependent on wind speed, atmospheric stability, stratification and composition of water, but if $tL_F(\lambda)$ is too large, the pixel is discarded.

(d) Radiance due to Rayleigh scattering – This is the major part of the radiance under clear atmospheric condition, contributing ~ 80% of the total radiance at the blue band and ~ 50% at NIR band (Wang, 2002). $L_R(\lambda)$ depends on the wavelength, viewing geometry, atmospheric pressure and other physical state of the ocean surface (Gordon and Wang, 1992). It is estimated from Rayleigh table, surface winds and solar viewing geometry (Cox and Munk, 1954; Wang, 2002). For processing of SeaWiFS data, the surface winds from NCEP / NCAR at 1^o resolution is interpolated to 1 km (Sayer et al., 2012).

(e) Radiance due to aerosol – For computing of aerosol radiance, the radiance due to ozone, sun glint, foam reflection and Rayleigh scattering are removed. For $\lambda > 700$ nm, when NIR subsurface reflectance and water-leaving radiances is zero, $L_T(\lambda) = L_A(\lambda)$. The aerosol radiance thus obtained in the NIR is compared with radiances that are numerically calculated using different aerosol models. If the observed and calculated radiance agree, then it is used for extrapolating the visible aerosol radiances from the corresponding observations in NIR. The extrapolated radiances are then removed from $L_T(\lambda)$, leaving only the attenuated water-leaving reflectance $tL_w(\lambda)$. Finally, t is removed to obtain $L_w(\lambda)$ (Martin, 2004).

(f) Radiance due to diffuse transmittance – Radiance received by the sensor from ocean surface also contains some background radiance from surrounding. If the FOV is close to land, the radiance received becomes land-contaminated, so that the ocean colour algorithm breaks down within a few pixels of the coast (Martin, 2004).

1.2.2 Water leaving radiance

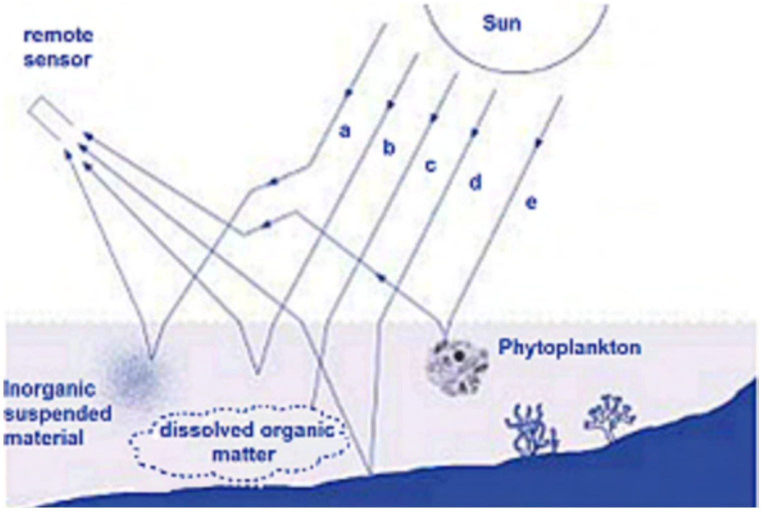

Figure 1.2. Factors that influence upwelling light leaving the sea surface. (a) upward scattering by inorganic suspended material; (b) upward scattering from water molecules; (c) absorption by the dissolved organic matter (d) reflection off the bottom; and (e) upward scattering from the phytoplankton component. (Modified from IOCCG, 2000)

The water leaving radiance, $L_w(\lambda)$ reaching the satellite contains information about coloured water constituents and hence, it is influenced by absorption and scattering of water molecules, suspended particles and dissolved materials. The magnitude and quality of the water-leaving radiations are used in the ocean colour remote sensing analyses to quantify the composition of substances present in the water (IOCCG, 2000).

1.2.3 Parameters measured by the sensor

The ocean colour sensor captures signatures of different constituents of coloured water, which are given below.

(a) Phytoplankton - These are microscopic, free-floating, ubiquitous organisms found in the illuminated surface layers of the ocean which forms the base of the aquatic food web. Chlorophyll 'a' (Chl *a*) is the dominant photosynthetic pigment found in phytoplankton cells and hence, Chl *a* is a proxy of phytoplankton concentration. Chl *a* is expressed in milligrams per meter cube, its range from 0.01 to 60 mg.m^{-3} (http://oceandata.sci.gsfc.nasa.gov/).

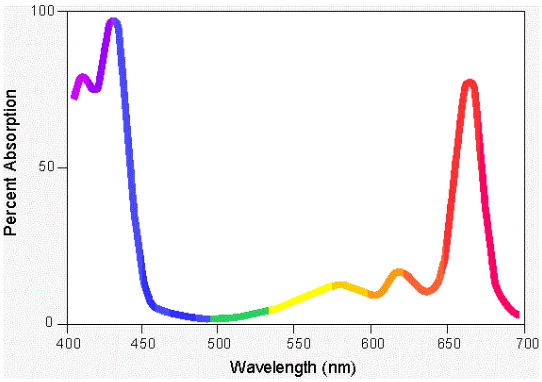

Figure 1.3. Absorption spectrum of Chl *a* (Source: http://www.ch.ic.ac.uk)

Chl *a* absorbs light in the blue portion of the electromagnetic spectrum, followed by red portion and hence, has two major absorption peaks corresponding to 440 nm (blue) and 665 nm (red) (Figure 1.3). In most of the cases, the blue peak is about three times greater than the red peak (Mobley, 1994). The absorption approaches zero between 450 and 650 nm (Figure 1.3; Kirk, 1994). These properties of visible light are utilised to identify and quantify Chl *a* concentration.

(b) Suspended Particulate Matter (SPM) and Dissolved Organic Carbon (DOC) – The coastal oceanographic processes such as tides, waves, river discharge and wind stress play an important role in the transport and distribution of suspended sediments. DOC is produced due to degradation of phytoplankton. Both suspended particles and decay matter absorb strongly in blue wavelength to impart a brownish yellow colour to water (Hoepffner and Sathyendranath, 1993). Ocean colour remote sensing is found to be effective in identifying and quantifying the above parameters (Pradhan et al., 2004; Prasad et al., 2002; Tassan, 1994).

Apart from the water constituents, satellite ocean colour remote sensing provides diffuse attenuation coefficient (K_d), aerosol optical depth (AOD) and angstrom coefficient.

(c) Diffuse attenuation coefficient (K_d) - It is an indicator of water clarity and is defined as the rate of change of irradiance with depth in the water column. It is expressed in m^{-1}. Chlorophyll and suspended sediment in water increases light attenuation and hence, K_d. A low value of K_d implies deep mixed layer, while a high value is an indicator of turbid, shallow mixed layer. Hence, this parameter is an important input to 1-dimensionl ocean models. Also, K_d serves as an important parameter to calculate visibility of the water column, which is important for diving. Hence this parameter has applications in navy for detecting underwater targets.

$$\text{Visibility} = 4/\,(c+K_d.\cos(\theta)) \;\ldots\ldots\ldots\ldots\ldots\ldots\ldots\; (1.2)$$

where, c is beam attenuation coefficient and θ is the solar viewing angle.

Both K_d and θ are provided by satellite and hence if 'c' is known it can be utilised to derive visibility. 'c' and K_d are related, but the empirical relation varies with water type. For off Kochi area, Sanilkumar et al. (2011) has formulated an empirical relation as

$$K_d = 0.140 * c - 0.047 \qquad \ldots\ldots\ldots\ldots\ldots\ldots \quad (1.3)$$

Similar, relations can be developed to get 'c' from K_d for each area / season and the visibility can be calculated without making *in situ* observations.

K_d is reciprocal of the depth, where surface radiance attenuates to 37% of the surface value (Muller et. al., 2003). Blue light (490 nm) can provide relatively better values due to least attenuation and hence K_d at 490nm gives the particle content in the water column. The present work utilises K_d at 490 nm to study its variability off the southwest coast of India.

(d) Aerosol Optical Depth (AOD) – AOD is the integrated extinction coefficient of the atmosphere due to aerosol particle. Hence, it is a measure of the atmospheric turbidity. There are various processes such as industrial pollution, biomass burning, desert dust, volcanic eruptions and sea salt from ocean surface that produce aerosol particles. These aerosol particles are carried from one region to other at various levels. Since aerosols play a major role on the global radiation budget, AOD serves an important parameter for climatic studies. Atmospheric deposition is a source of iron nutrient to ocean, which enhances primary production (Duce and Tinsdale, 1991; Fan et al., 2006; Jickells et al., 2005; Mahowald et al., 2005; Mahowald et al., 2009; Santos 2010; Sholkovitz et al., 2009; Wiggert and Murtugudde, 2007). The increased iron content is reflected on AOD and a good correlation between AOD and

Chl *a* exists in the western Arabian sea and eastern Atlantic Ocean (Patra et al., 2006; Santos, 2010).

(e) Angstrom coefficient (α) – **α** is a measure of the spectral dependence of AOD with the incident wavelength of light (λ). **α** is computed from AOD measurements at two different wavelengths viz. λi and λj between visible and NIR bands and is expressed as (http://disc.sci.gsfc.nasa.gov):

$$\alpha = \frac{-\log\left(AOD(\lambda i) / AOD(\lambda j)\right)}{\log\left(\lambda i / \lambda j\right)} \quad \ldots\ldots\ldots\ldots\ldots\ldots\ldots \quad (1.4)$$

The present work utilises Chl *a*, K_d and AOD to study the oceanographic and atmospheric characteristics.

1.2.4 Ocean colour satellites

Studies on the remote sensing of ocean colour from space began in October 1978 with launch of NASA‘s Coastal Zone Colour Scanner (CZCS) through NIMBUS – 7 satellite. CZCS was followed by a series of sophisticated instruments viz. MOS, OCTS, POLDER, SeaWiFS, OCI, OCM, OSMI, MERIS, CMODIS, COCTS CZI, OSMI, GLI, POLDER-2, MODIS_AQUA, MISR, POLDER-3, MERSI, HICO, OCM-2, GOCI and VIIRS. Compared to CZCS, many additional channels and improvements were incorporated in each of these sensors. Many of these sensors are equipped with tilting property. Some of the sensors could be rotated and variant calibration techniques were also employed.

The characteristics of past ocean colour sensors are furnished in Table. 1.2. Among the past ocean colour sensors, a short description on CZCS, SeaWiFS and

OCM is provided. SeaWiFS was the first and the only sensor to complete 13 years and hence, represents the best available ocean colour data for climatic studies.

1.2.4.1 CZCS

CZCS provided continues ocean colour observations since its launch till August 1981, and later faced interruption due to its degradation. However, the CZCS mission was success providing many lessons to the science community regarding calibration, validation and atmospheric corrections of an ocean colour remote sensing system. It also provided oceanographers with new insights into the biological and chemical properties of ocean water masses. However, much of the CZCS data remained unverified and inadequately calibrated. The Sea-viewing Wide Field-of-view Sensor (SeaWiFS) is the NASA successor instrument to the CZCS (Evans and Gordon, 1994).

1.2.4.2 SeaWiFS

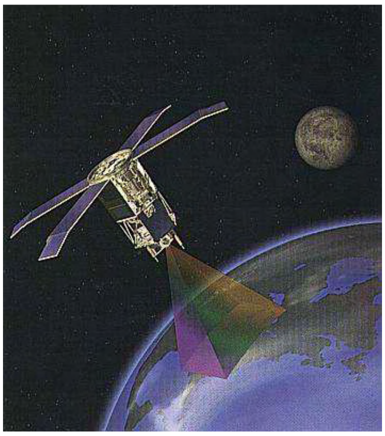

Figure 1.4. Orb View-2 spacecraft (Source: oceancolour.gsfc.nasa.gov)

The SeaWiFS instrument was launched on 1 August 1997 on board the OrbView-2 spacecraft (Figure 1.4). The spacecraft occupied a sun-synchronous orbit at an altitude of 705 km with an equatorial crossing time at 12 pm. SeaWiFS became operational on 18 September 1997 and routinely provided global coverage every two days.

Table 1.2. Characteristics of past ocean colour sensors. (Source: http://www.ioccg.org; https://earth.esa.int; Martin, 2004; Wikipedia)

Sensor	Platform	Agency	Operational period	Swath (Km)	Spatial resolution (Km)
CZCS	Nimbus-7	NASA	Oct 1978 - Jun 1986	1556	0.82
MOS	IRS-P3	DLR	Mar 1996 - May 2004	200	0.50
OCTS	ADEOS	NASDA	Aug 1996 - Jun 1997	1400	0.70
POLDER	ADEOS	CNES	Aug 1996 - Jun 1997	2400	6
SeaWiFS	Orbview -2	NASA	Aug 1997 - Dec 2010	2800	1.10
OCI	ROCSAT-1	NEC	Jan 1999 - Jun 2004	690	0.82
OCM	IRS-P4	ISRO	May 1999 - Aug 2010	1420	0.36
OSMI	KOMPSAT-1	KARI	Dec 1999 - Jan 2008	800	0.85
MERIS	ENVISAT	ESA	Mar 2002 - May 2012	1150	0.30
CMODIS	SZ-3	CNSA	Mar 2002 - Sep 2002	650-700	0.40
COCTS CZI	HY-1A	CNSA	May 2002 - Apr 2004	1400 /500	1.10 /0.25
GLI	ADEOS-II	NASDA	Dec 2002 - Oct 2003	1600	0.25/1.00
POLDER-2	ADEOS-II	CNES	Dec 2002 - Oct 2003	2400	6.00

SeaWiFS instrument was a cross-track scanner capable of covering 2800 km at 1.1 km spatial resolution. The lunar calibration was used to maintain its radiometric stability. However, during its operational period, the spacecraft telemetry became invalid due to failure of GPS, SeaWiFS interface and battery. As a result, there are gaps in data collection during 1 January 2008 – 12 April 2008. In order to make data available at same accuracy, the spacecraft orbit altitude changed from 705 to 690 km. The SeaWiFS data processing team incorporated the corresponding orbit inclination and its effects in the data processing (oceancolour.gsfc.nasa.gov; modis.gsfc.nasa.gov/). Unfortunately after long adventure the sensor failed on 14 December 2010 (https://earth.esa.int).

The present ocean colour sensors and their specifications are listed in Table 1.3. Among them, MODIS_AQUA is utilised in the present work.

1.2.4.3 MODIS

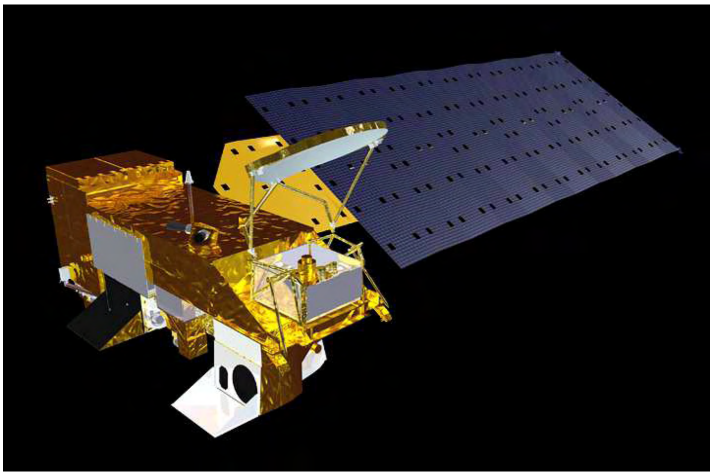

Figure 1.5. MODIS_AQUA satellite (Source: http://earthobservatory.nasa.gov)

MODerate- resolution Imaging Spectroradiometer (MODIS) are the series of EOS sensors launched by NASA on TERRA (December 1999) and AQUA (May

2002) satellites (Figure 1.5). Unlike SeaWiFS, MODIS records SST also with a spatial resolution of 1.1 km at nadir (http://modis.gsfc.nasa.gov).

Table 1.3. Characteristics of present ocean colour sensors. (Source: http://www.ioccg.org; Martin, 2004; Wikipedia)

Sensor	Platform	Agency	Launch date	Swath (Km)	Spatial resolution (Km)
MODIS_ TERRA	Terra	NASA	18/12/1999	2330	1.00
MODIS_ AQUA	AQUA	NASA	4/05/2002	2330	1.00
POLDER -3	Parasol	CNES	18/12/2004	2100	6.00
COCTS CZI	HY-1B	CNSA	11/04/2007	2400/500	1.10/0.25
MERSI	FY-3A	CNSA	27/05/2008	2400	0.25/1.00
MERSI	FY-3B	CNSA	5/11/2010	2400	0.25/1.00
HICO	JEM-EF	ONR/ DOD	18/09/2009	50 (selected coastal scenes)	0.10
OCM-2	Oceansat-2	ISRO	23/09/2009	1420	0.36
GOCI	COMS	KARI/ KORDI	26/06/2010	2500	0.50
VIIRS	NPP	NOAA/ NASA	28/10/2011	3000	0.37 / 0.74

1.2.4.4 Ocean Colour Monitor (OCM) and OCM-2

Ocean Colour Monitor (OCM) and OCM-2 deserves special mention as they were launched by the Indian Space Research Organisation and designed to map the ocean colour, especially in Indian waters. OCM is the first satellite sensor employed for oceanographic studies in the Indian waters. The sensor was launched on board Oceansat – 1 on 26 May 1999. It operated successfully till August 2010 and OCM-2, the successor of OCM launched on 23 September 2009, and is currently operational.

1.2.5 Ocean colour algorithms

1.2.5.1 AOD retrieval algorithm

The atmospheric parameter, AOD is the reciprocal of measured reflectance. In this procedure, the atmospheric-correction parameter (ε) is obtained for each pixels as follows,

$$\varepsilon(\lambda_i, \lambda_j) = \rho_{as}(\lambda i) / \rho_{as}(\lambda j) \qquad \ldots\ldots\ldots\ldots\ldots\ldots\ldots\ldots\ldots\ldots\ldots\ldots\ldots\ (1.5)$$

where, λ_i, λ_j represents the two selected NIR wave bands. ε – atmospheric correction parameter, $\rho_{as}(\lambda)$, the single scattering aerosol reflectance is the sum of reflectance due to aerosol scattering and Rayleigh-aerosol interactions. ie, $\rho_{as}(\lambda) = \rho_a(\lambda) + \rho_{ra}(\lambda)$.

The obtained $\varepsilon(\lambda_i, \lambda_j)$ is compared with values of ε provided in the lookup tables. If it is comparable, model ε, AOD (λ) of the model is adopted or if the value lie between two models, AOD is obtained by interpolating between two models (Gordon and Wang, 1994; Wang and Gordon, 1994) as given below,

$$AOD(\lambda) = (1-r_a)\, AOD^{(1)}(\lambda) + r_a\, AOD^{(2)}(\lambda) \ \ldots\ldots\ldots\ldots\ldots\ldots\ (1.6)$$

$$r_a = \frac{\varepsilon^{(avg)} - \varepsilon^{(1)}}{\varepsilon^{(2)} - \varepsilon^{(2)}} \qquad \ldots\ldots\ldots\ldots\ldots\ldots\ldots\ldots\ldots\ldots\ldots\ (1.7)$$

where, $AOD^{(1)}(\lambda)$ and $AOD^{(2)}(\lambda)$ are model retrieved AOD.

The aerosol lookup tables for SeaWiFS are based on approximately 25,000 radiative transfer simulations derived from twelve different MODTRAN aerosol models (Martin, 2004).

1.2.5.2 Bio-optical algorithm - Chl *a* and K_d

Two kinds of bio-optical algorithms between 400 – 500 nm are operational viz. empirical and semianalytic.

The Chl *a* and K_d data used in the present work is extracted using empirical algorithms updated from NASA bio-optical Marine Algorithm Data (NOMAD) version 2 (http://oceandata.sci.gsfc.nasa.gov/). NOMAD is the largest publicly available *in situ* bio-optical data for Chl *a* to validate satellite ocean colour algorithm. The data is applicable to coastal and open ocean regions collected by Ocean Biology & Biogeochemistry Program of NASA.

a. Chl *a* algorithm

Both SeaWiFS and MODIS_AQUA utilise an empirical algorithm to derive Chl *a*. The algorithm is called maximum band ratio, as the criteria to derive Chl *a* is not fixed. It considers the maximum reflectance between 443 nm (Rrs443), Rrs489 and Rrs510 for SeaWiFS, whereas in the case of MODIS_AQUA, Rrs443 and Rrs489 are considered. The algorithm relates a logarithmic transformed ratio of remote-sensing reflectance's to the logarithm of Chl *a* (http://oceandata.sci.gsfc.nasa.gov/) as given by Eqn (1.8).

$$\mathrm{Log}_{10}(\mathrm{Chl}\ a) = (a0 + a1*X + a2*X^2 + a3*X^3 + a4*X^4) \qquad \ldots\ldots\ldots\ldots(1.8)$$

In the case of SeaWiFS, the coefficients a0, a1, a2, a3, a4 and X are as follows

a0 = 0.3272, a1 = -2.9940, a2 = 2.7218, a3 = -1.2259, a4 = -0.5683,

$X = \log_{10}(Rrs_{max})/\log_{10}(Rrs555)$ and $Rrs_{max} = Rrs(443>489>510)$

and for MODIS_AQUA, the coefficients are

a0 = 0.2424, a1 = -2.7423, a2 = 1.8017, a3 = 0.0015, a4 = -1.2280,

$X = \log_{10}(Rrs_{max})/\log_{10}(Rrs547)$ and $Rrs_{max} = Rrs(443>489)$

b. K_d algorithms

The K_d algorithm for both SeaWiFS and MODIS_AQUA are given by Eqn (1.9) (http://oceandata.sci.gsfc.nasa.gov/).

$\text{Log}_{10}(K_d) = (a0 + a1*X + a2*X^2 + a3*X^3 + a4*X^4) + 0.0166$ ………….(1.9)

In the case of SeaWiFS, coefficients a0, a1, a2, a3, a4 and X are

a0 = -0.8515, a1 = -1.8263, a2 = 1.8714, a3 = -2.4414, a4 = -1.0690,

$X = \log_{10}(Rrs489)/\log_{10}(Rrs555)$

and for MODIS_AQUA, the coefficients are

a0 = -0.8813, a1 = -2.0584, a2 = 2.5878, a3 = -3.4885, a4 = -1.5061,

$X = \log_{10}(Rrs489)/\log_{10}(Rrs547)$

1. 3 Objective of the study

1.3.1 Study area

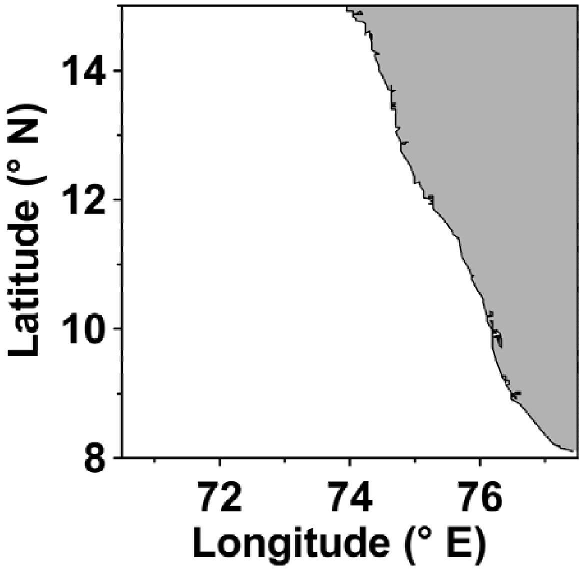

Figure 1.6. Study area

The area selected for the study is bound by 70.5-77.5° E and 8-15° N (Figure

1.6), which is one of the highly dynamic areas of the world ocean waters due to the influence of southwest and northeast monsoons. The coast line is observed to have an inclination of ~25^o with the geographic north.

1.3.2 Atmospheric conditions

During the southwest monsoon period, strong westerly to northwesterly wind ($\geq$ 10 m.s^{-1}) prevails over the study area, which changes to northeasterly with moderate speed (< 5 m.s^{-1}) during the northeast monsoon period (Shetye et al. 1990). Wind at 700 hPa level is of great significance during this period for aerosol studies, as this level is the carrier of African and Arabian iron particles (Li and Ramanathan, 2002). The area is enriched with desert dust and sea salt during the southwest monsoon and rest of the period continental aerosol from India southeast Asian continent prevailed over the area (Li and Ramanathan, 2002; Mandal et al., 2006; Nair et al., 2012; Rajeev et al., 2000; Rasch et al., 2001). These particles settle down after a fixed period depending on their size.

1.3.3 Oceanographic conditions

The surface current viz. West India Coastal Current (WICC) also undergoes seasonal reversal under the influence of surface winds. WICC is equatorward during the southwest monsoon period and poleward during northeast monsoon period (Shankar et al., 2002). In addition, Kelvin waves give rise to intra-annual variation (Rao et al., 2009).

During the southwest monsoon period, coastal upwelling emerging from the favourable currents and winds occurs off the coast (Shankar et al., 2002; Shetye et al., 1990). The process brings cooler, nutrient-rich subsurface water to the surface.

Consequently, primary production increases causing phytoplankton bloom (Banse et al., 1996; Sharma, 1978). Contrary to this, the Bay of Bengal (BoB) water intrudes and sinking occurs during the northeast monsoon period. Intrusion of the BoB water also induces a decreased primary production (Kumar et al., 2004).

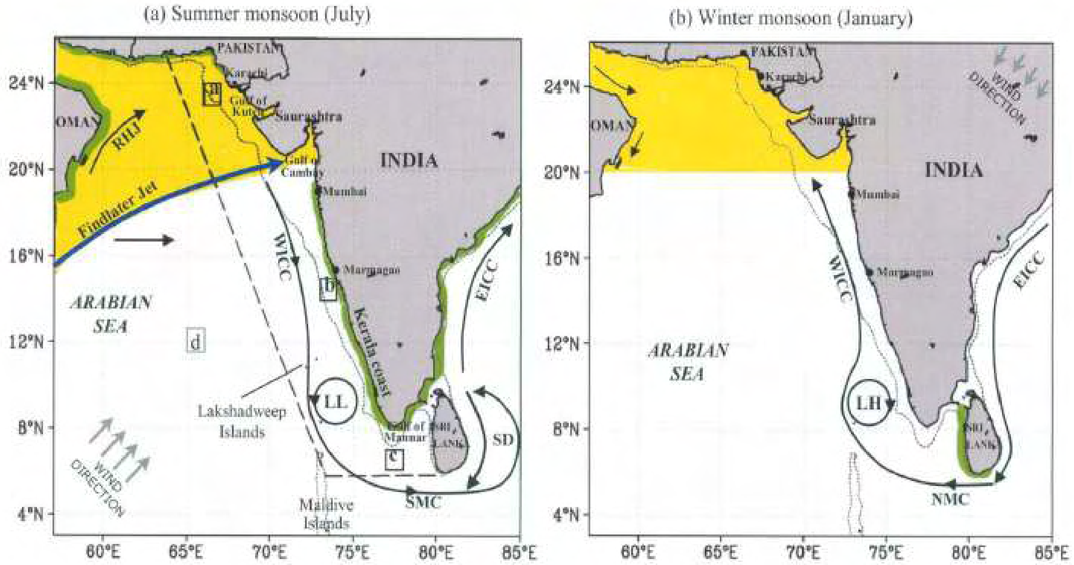

(a) Summer monsoon (July)

(b) Winter monsoon (January)

Figure 1.7. (a) Geography of the northern Arabian Sea. Schematics of summer-monsoon circulation are superimposed. Ekman pumping region in the northern Arabian Sea is highlighted in yellow tone. Coastal upwelling promoted by divergence of alongshore wind stress component is indicated in green tone. Current branches indicated are the Ras al Hadd Jet (RHJ), Lakshadweep Low (LL), West India Coastal Current (WICC), Southwest Monsoon Current (SMC), Sri Lanka Dome (SD) and East India Coastal Current (EICC). The Findlater Jet and wind direction are indicated by bold gray arrows. (b) As in (a), but for winter monsoon. Additional abbreviations shown are: Lakshadweep High (LH) and Northeast Monsoon Current (NMC). (Source: Luis and Kawamura, 2004)

Cyclonic / anticyclonic eddies are observed with low / high pressure over the Lakshadweep Sea called the Lakshadweep low / high (Bruce et al., 1998; Sanilkumar and Kumar, 2005; Shankar and Shetye, 1997). The forcing mechanism for these low / high is the Kelvin waves from BoB. Lakshadweep low induces upwelling in the area and are observed during July – October (McCreary et al., 1993). Contrary to this, Lakshadweep high forms during January and results in downwelling.

An important phenomenon occurs in this region during the south-west monsoon is the Mud bank formation, which is a unique characteristic feature of the region (Tatavarti and Narayana, 2006; Varma and Kurup, 1969). During the occurrence of this phenomenon, the waters become very turbid and slimy with the suspended sediment load. In addition, River discharge from Periyar, Bharathapuzha and Chaliyar alters the water characteristics especially during the southwest monsoon period (Priju and Narayana, 2007; http://en.wikipedia.org/).

The bottom topography includes continental shelf, continental slope and deep sea (> 2000 m). The inner shelf is covered by silts and clayey silts, outer shelf by oolitic sands, coral reefs, algal knolls, bioherms or lithified sediments, the lower part of the slope by silty clay / mud, the upper part of the slope by sand-silt-clay facies and the deep sea by clay (Karisiddaiah and Veerayya, 2002). Hence, seabed is characterised by varying sediment contents. In addition, the region experiences sediment transport across the shelf (Rao and Rao, 1995) and along the coast (Chandramohan and Nayak, 1992). The river discharge and sediment concentration, along with Chl *a* and decay matter increases K_d during the southwest monsoon.

It is evident that the study area is highly dynamic and ocean colour data can effectively depict oceanographic and atmospheric characteristics of such a region. Several studies utilising *in situ* measurements (Banse, 1959; Banse et al., 1996; Johannessen et al., 1987; Shetye et al., 1984; Shetye et al., 1985; Shetye et al., 1988 Shetye et al., 1990), satellite observations (Jayaram et al. 2010; Jayaram, 2011; Matondkar et al. 2006; Sankar et al. 2010) and model studies (Haugen et al., 2002; Shaji and Gangopadhyay, 2007; Shankar et al., 2002) are carried out in the study area.

Satellite ocean colour data are sparsely utilised in the study area. Among them, many studies were to validate oceanographic features like algal bloom, river discharge, etc. (Chauhan, 2003; Matondkar, et al. 2006; Prasad et al. 2002; Sarangi et al. 2005; Watts et al. 2005). Majority of these ocean colour observation are carried out off the west coast of India, focused the northwestern side. However, as far as Indian economy is considered, fisheries play a significant role in the south west coast of India (Madhupratap et al. 2001). View above, objective of the present study is to explore the utility of data from ocean colour sensor to study the oceanographic and overlying atmospheric features off the southwest coast of India. Accordingly, the present work concentrates on spatio-temporal variability of Chl a, K_d and AOD and the feasibility of deriving upwelling features using satellite ocean colour observations.

Chapter 2

Data and Methodology

2.1 Data

2.1.1 Satellite

(a) Ocean colour data

Global Area Coverage on Chl *a*, K_d and AOD at 9x9 km^2 from SeaWiFS sensor for various time windows viz. daily, weekly, monthly, monthly climatology during the period September 1997- December 2010 are extracted from the ocean colour site (http://oceandata.sci.gsfc.nasa.gov/). Similar data at 4x4 km^2 resolution from MODIS_AQUA during the period July 2002 – March 2012 are also used along with SeaWiFS data. In addition, the seasonal global climatology generated by the site utilising SeaWiFS sensor for four seasons i.e. autumn (mid-September to mid-December), winter (20th November – 19th March), spring (20th March – 19th June) and summer (20th June – 19th August) are examined to obtain a comprehensive picture of the global variability. The GAC data provided in Hierarchical Data Format (HDF) was extracted with the aid of SeaDAS software.

(b) Wind

Daily averaged wind data on zonal and meridional scale were extracted from QuikSCAT for the period 19 July 1999 – 19 November 2009 (ftp://www.ssmi.com). Monthly wind was generated from the above dataset using ferret software. The alongshore component was calculated for each area using the monthly averaged dataset.

(c) SST

SST from MODIS / AQUA sensor at 4 and 9 km spatial resolutions were downloaded from website http://oceandata.sci.gsfc.nasa.gov for different time scale of daily, 3 day, 8 day, monthly and monthly climatology.

Similarly, daily AVHRR SST data was downloaded for the study period and utilised to generate SST at chosen temporal scales utilising Ferret software.

(d) Sea Surface Height Anomaly (SSHA)

Monthly and monthly climatology on SSHA data during January 1992 - February 2010 were downloaded from AVISO site (www.aviso.soest.hawaii.edu). The SSHA data obtained from AVISO is the merged product of TOPEX, ERS and Jason-1 altimetry. The data has a spatial resolution of 0.33^o.

(e) Rain data

Weekly rainfall data from TMI sensor (December 1997 – February 2011) at 0.25^o x 0.25^o spatial resolution was downloaded and was used to generate monthly rainfall rate.

2.1.2 *In situ* temperature

SST collected from *INS Sagardhwani* off Kochi using Mini CTD (M/s SAIV, Norway) during eight years representing upwelling phases between 1998 and 2009 were utilised (Figure 2.1. and Table 2.1). Accuracy of the temperature data is $\pm 0.01^oC$ and depth is 0.01 % of the measured depth. Since the sea surface temperature values at 0 m depth cannot be measured accurately using Mini CTD, the values at 5 m depth were considered as the SST. The spatial and temporal information on data collection is given below.

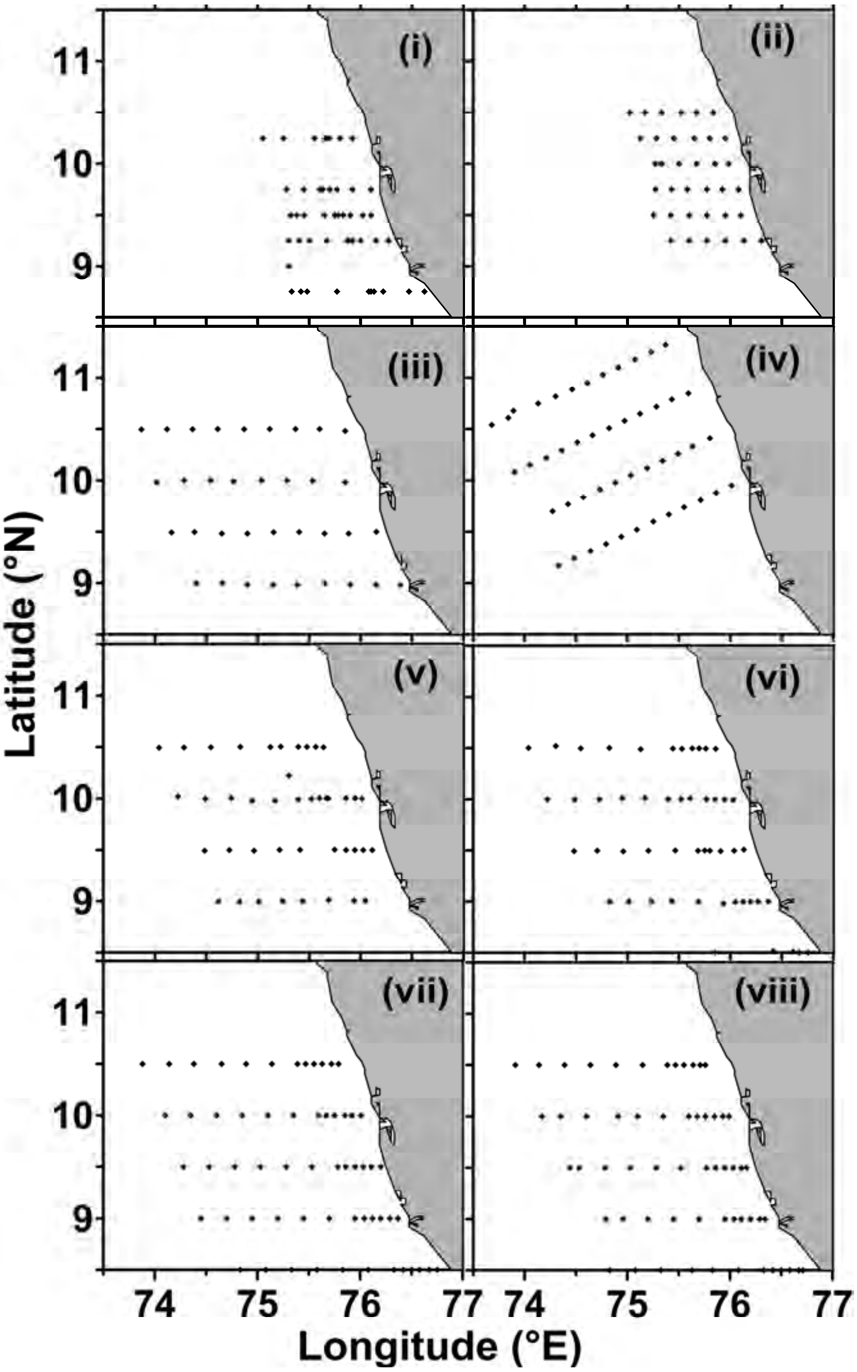

Figure 2.1. *In situ* data location during (i) August 1998, (ii) July 2000, (iii) July 2003, (iv) June 2004, (v)August 2007, (vi) September 2007, (vii) June 2009 and (viii) July 2009.

Table 2.1. Period and locations of *in situ* observations.

SI. No.	Period	No. of stations
a	13 – 17 August 1998	70
b	10 – 12 July 2000	37
c	14 – 18 July 2003	35
d	7 – 11 June 2004	47
e	3 – 9 August 2007	42
f	3 – 7 September 2007	53
g	1 – 5 June 2009	60
h	8 – 12 July 2009	59

(a) **August 1998 -** During 13 – 17 August 1998, *in situ* temperature was collected along five transects. Each transect was selected such that the first and last transects were 0.5° apart from their adjacent ones and the rest were at 0.25° apart. In each transect, CTD observations were made at 3 -5 nautical mile intervals.

(b) July 2000- Thirty seven CTD casts were carried out from six transects, separated by 0.25° zonally and each station was separated by 0.20° meridionally. These observations were completed during 10 – 12 July 2000.

(c) July 2003- The *in situ* stations spanned over at 15 nautical miles intervals along four transects using CTD. The transects were selected such a way that they were separated by 0.3° intervals from south to north and begins from the 30 m depth contour and extending offshore up to ~ 220 km.

(d) June 2004- Forty seven temperature profiles were collected from four transects perpendicular to the coast during 7 – 11 June 2004. These transects were 0.50^o apart and each stations was separated by 0.15^o along the transect.

(e) August 2007, September 2007, June 2009, July 2009- During all these field programmes, temperature profiles were collected from four transects which were 0.5^o apart. In each transect, station locations were selected such a way that each location was separated from the other by 0.1^o within 200 m depth contour and by 0.2^o beyond 200 m contour.

In all the above field programmes, temperature data were available at < 1m vertical resolution. These data were vertically interpolated to 1 m and temperature at 5 m depth is taken as SST.

2.1.3 Data processing

The surface currents provided by European Centre for Medium range Weather Forecast (ECMWF) during the period January 1959 – December 2009 was used for the study (www.aviso.soest.hawaii.edu). Monthly zonal and meridional currents with spatial resolution of 1^o were downloaded to examine the alongshore surface currents.

NCEP / NCAR wind at a spatial resolution of 2.5^o x 2.5^o and daily temporal resolution was extracted from NCEP / NCAR site. NCEP winds at the 1000 hPa and 700 hPa pressure levels are utilised in the work.

2.1.4 Surface currents from ship observations

Ship drift data during 1900-1993 across the Indian Ocean (20^o-120^{o}E and 30^{o}S-30^{o}N) logged by the commercial and research ships and archived at UK Meteorological office are utilized to obtain ocean current climatology.

2.1.5 GOCART model

The Goddard Global Ozone Chemistry Aerosol Radiation and Transport (GOCART) model is a global scale model with horizontal resolution of 2.5^{o} longitude X 2.0^{o} latitude and uses the assimilated meteorological fields of the Data Assimilation System (DAS), generated by the Goddard Modeling and Assimilation Office. The GOCART model simulates the AOD for tropospheric aerosol components, such as sulfate, dust, black carbon, organic carbon and sea-salt (Chin et al., 2000; Chin et al., 2002; Ginoux et al., 2001). The present work utilises fine dust and sea salt simulated by the model over the atmosphere off the southwest coast of India during January 2000 – December 2007. These data were downloaded from Giovanni maintained by NASA (http://gdata1.sci.gsfc.nasa.gov/).

2.1.6 Nino index and Dipole Mode Index (DMI)

Nino index is adopted from Climatic Prediction Centre maintained by NOAA (www.nws.noaa.gov). Nino index were calculated from the three month running mean of ERSST.v3b SST anomalies in the Nino 3.4 region (5^{o}N-5^{o}S, 120^{o}-170^{o}W).

DMI is the difference in SST anomaly between Western Tropical Indian Ocean (50^{o}E – 70^{o}E and 10^{o}S – 10^{o}N) and South Eastern Tropical Indian Ocean (90^{o}E – 110^{o}E and 10^{o}S – 0^{o}N) based on Reynolds OIV2.SST. DMI during September 1997 – December 2010 is obtained from JAMSTEC site (http://www.jamstec.go.jp).

2.2 Methodology

2.2.1 Selected areas

- Area 1 (7^{o} x 7^{o})

The southwest coast of India (70.5-77.5 ^{o} E, 8.0-15.0 ^{o} N) was selected to study the oceanographic and atmospheric features using the ocean colour sensors. Within Area 1, two 3^o x 3^o areas and six 0.5^o x 0.5^o were selected to understand the regional scale variability on inter- and intra-annual variability in Chl *a*, K_d and AOD distribution (Figure 2.2).

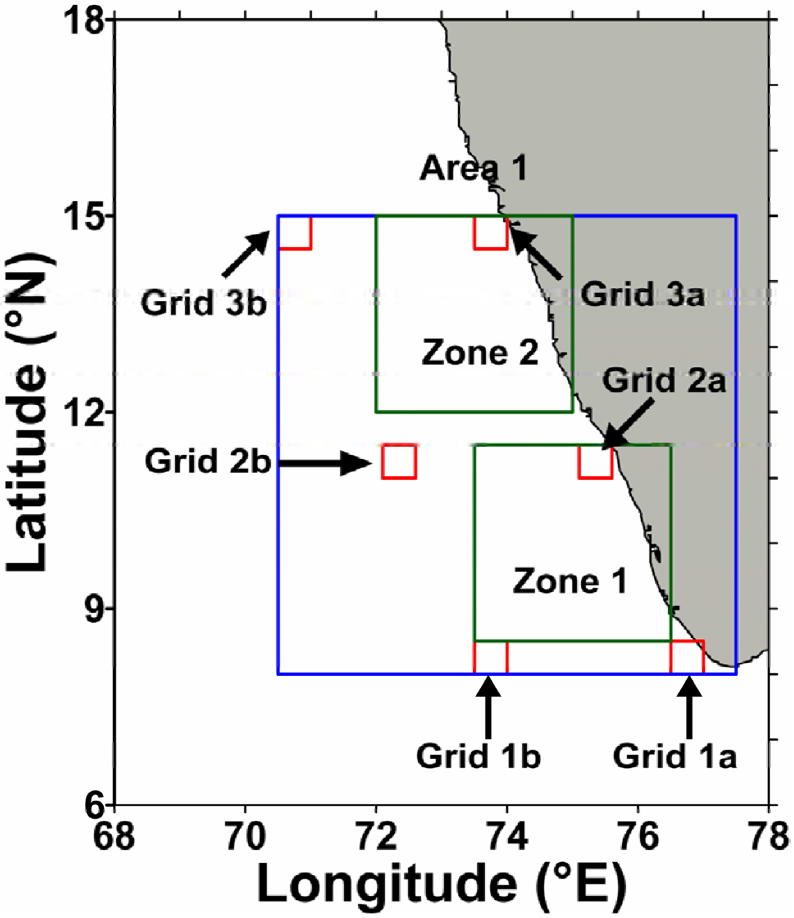

Figure 2.2. Study area. Area 1 (Blue square). Zone 1 and 2 (Green square). Grid 1 to 3 (Red square) (suffix 'a' represents coastal and 'b' offshore areas)

- Zone 1 and 2 (3^o x 3^o)

Areas with spatial extent 3^o x 3^o was selected from the southern (73.5-76.5^{o}E, 8.5-11.5^{o}N) and northern sides (72.0-75.0^{o}E, 12.0-15.0^{o}N) within Area 1 and denoted as Zone 1 and Zone 2 for brevity.

- Grid 1, 2 and 3 (0.5° x 0.5°)

The coastal and offshore areas comprising of 0.5°x0.5° grid of Thiruvananthapuram (76.5-77.0°E, 8.0-8.5°N; 73.5-74.0°E, 8.0-8.5°N), Kozhikode (75.1-75.6°E, 11.0-11.5°N; 72.1-72.6°E, 11.0-11.5°N) and Karwar (73.5-74.0°E, 14.5-15.0°N; 70.5-71.0°E, 14.5-15.0°N) representing south, central and north regions were selected. These regions are named as Grid 1 to Grid 3 respectively and suffixed with ‘a’ to coastal and ‘b’ to offshore areas to demarcate them.

2.2.2 Statistical analysis

Major statistical methods used in the thesis are given below.

2.2.2.1 Empirical Mode Decomposition

Empirical Mode Decomposition (EMD) is a processing tool designed to analyse non-linear and non-stationary properties (Huang et al., 1998). The advantage is that the basis function is derived directly from the signal. It also splits time-series data into intrinsic oscillations, and separate nonlinear oscillations from low frequency oscillations. These oscillatory modes are called the Intrinsic Mode Functions (IMF). Huang et al (1998) defined an IMF as any function satisfying the following conditions:

(1) The number of extremes and zero crossings must be equal or differ by one.

(2) At any point, the mean value defined by the local maxima and the envelope defined by the local minima must be zero.

The procedure to decompose a time series signal s(t) into IMFs are summarized as follows:

(i) Identify the extremes (maxima and minima) in the signal s(t)

(ii) generate the upper h(t) and lower l(t) envelopes, by connecting the maxima and minima points using cubic spline interpolation

(iii) determine the mean envelope, m(t) representing the highest frequency following the relationship, $m(t)=[h(t)+l(t)]/2$

(iv) IMF should have zero local mean and hence, $r(t) = [s(t) – m(t)]$

(v) Examine whether the obtained r(t) satisfies IMF criteria or not.

(vi) Continue iterations of step (i) – (v) till r(t) becomes an IMF.

(vii) IMF is subtracted from s(t) to obtain new signal

(viii) Step (i) – (vii) is continued till all IMF are extracted, leaving behind a residual.

Once the mean value of m(t) is close to zero, the residual can be considered as an IMF (Huang et al, 1998). The stopping criteria is introduced here based on two thresholds θ_1 and θ_2 considering small fluctuations in the mean (Huang et al, 2003). The threshold values are estimated from the amplitude $a (t) = [h(t) - l(t)] / 2$ and the evaluation frequency $\sigma (t) = | m(t) / a(t)|$. The sifting is iterated until $\sigma (t) < \theta_1$ for a prescribed fraction (1-α) of the total duration atains $\sigma (t) < \theta_2$ for the remaining fraction. In this case the parameters are set as $\alpha \approx 0.05$, $\theta_1 = 0.05$ and $\theta_2 = 10\ \theta_1$ (Rilling, 2003).

2.2.2.2 Regression analysis

Regression analysis was carried out to bring out the relationships among different parameters viz. Chl *a* and K_d with SST. Their acceptance was verified in terms of coefficient of determination (r^2), error percentage (err %) and Root Mean Square Deviations (RMSD).

2.2.3 HYSPLIT model

The trajectory is important in determining the source of aerosol and to trace it back. In this work, the back trajectory was computed using HYSPLIT (Hybrid Single-Particle Lagrangian Integrated Trajectory) (version 4) model (Draxler and Hess, 1998) of Air Resources Laboratory, NOAA. The model traces the trajectory utilising the wind and temperature fields, retrieved from NCEP/NCAR data archives (ftp://www.arl.noaa.gov/pub/archives/fnl). The model is useful to trace forth and back the path. In this work, the trajectories were traced back at two heights viz. 1000 and 700 hPa.

2.2.4 Data analysis and plotting tools

Software packages viz. SeaDAS, MATLAB, FORTRAN and Ferret are utilised to carry out mathematical computations. For scientific visualisation, plots were generated using MATLAB, Surfer and Grapher.

SeaDAS (SeaWiFS Data Analysis System) is widely utilised software, designed to perform ocean colour data analysis. The software is capable of analyzing different level and area coverage. In the present work, level 3 GAC ocean colour and SST data were extracted for the southwest coast of India using SeaDAS.

MATLAB is a software package for scientific applications providing interactive environment for numerical computation, visualization, and programming developed by MathWorks (http://www.mathworks.in/products). Most of the plots were produced with the aid of this software.

Surfer generates various plots including 3D contour maps. Grapher aids to create 2D and 3D graphs (http://www.alentum.com/agrapher/). Many plots including the regression analysis were carried out using above software packages.

FORTRAN is a scientific programming language to carry out numeric computation (http://groups.engin.umd.umich.edu). In the present work, the language was extensively used for many computations.

Ferret is an interactive computer visualization and analysis environment designed to analyzing large and complex gridded data sets (http://ferret.wrc.noaa.gov/Ferret/). Ferret was used for averaging daily dataset over monthly intervals.

Chapter 3

Climatology

Climatology of ocean colour parameters generated from both satellites SeaWiFS and MODIS_AQUA is provided by NASA (http://oceandata.sci.gsfc.nasa.gov/). The data on Chl *a*, K_d and AOD has been extracted from the site and utilised in this study. A prior knowledge on the global climatology of the parameters is a prerequisite to comprehend the regional scale oceanography and meteorology as they have teleconnections to the global features in most of the cases. Accordingly, the global climatology of the parameters is examined very briefly on a seasonal scale and thereafter, the regional scale climatology has been analysed on monthly scale. Subsequent analysis is based on the observations from the climatological features.

3.1 Global climatology

Satellite ocean colour observations provide continuous global observations on Chl *a*, K_d and AOD. These datasets are useful in identifying algal bloom, eddies, fronts, river discharge, monitoring water quality, aerosol studies, etc.

3.1.1 Chl *a*

The blue and violet patches in the Pacific, Atlantic and south Indian Oceans (Figure 3.1) represent the low chlorophyll regions of the world oceans, which appears in mid-ocean circulation gyres. The productivity in these regions is very low due to oligotrophic conditions (Conkright et al., 2002; Polovina et al., 2008; Signorini and McClain, 2012). Moderate values are observed in the equatorial regions of Pacific and Atlantic Oceans, where the upwelling takes place due to the divergence in the upper layers of the oceans induced by the easterly winds (Johnson et al., 2001). However, it is to be noted that similar moderately high Chl *a* region is absent in the equatorial Indian Ocean resulting from the absence of such upwelling inducing winds in the Indian Ocean throughout the year. High values of Chl *a* are observed in high latitudes and coastal regions. In high latitudes, high chlorophyll appears due to high nutrients (Conkright et al., 2002; Taylor and Ferrari, 2011 and therein). Among the coastal regions, the major upwelling zones viz. off California, off Canary, off Benguela, Off Somalia and off Peru are well known for the high values due to the significant primary productivity resulting from the vertical movement of nutrient rich waters from subsurface to surface layers (Kahru et al., 2012; Patti et al., 2008). It is to be noted that the seasonal variability in the north India Ocean, especially in the western part of the Arabian Sea is very prominent emerging from the seasonal monsoon winds and the consequent seasonal upwelling phenomenon (Wiggert et al., 2005).

3.1.2 K_d

K_d also shows minimum in the mid-ocean gyres and moderate in the equatorial upwelling zones in the Pacific and Atlantic and high in the high latitudes and coastal regions, similar to Chl *a* (Figure 3.2). However, seasonal variability in K_d is very prominent in the polar regions. K_d becomes very high in the northern (southern) polar regions during spring / summer (autumn / winter), whereas the low occurs during the other seasons in both the polar regions. This seasonal variability coincides with seasonal solar march from one hemisphere to the other. In addition, prominent seasonal variability is noticed in the north Indian Ocean especially in the Arabian Sea, which matches with the upwelling zones.

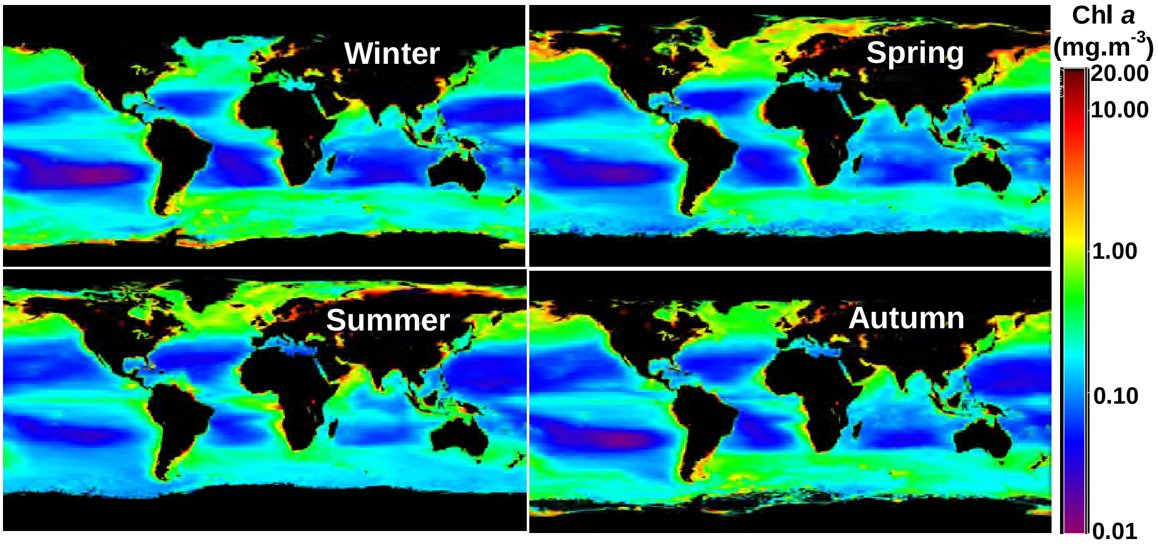

Figure 3.1. Seasonal composites on global Chl *a* distribution as obtained from SeaWiFS.

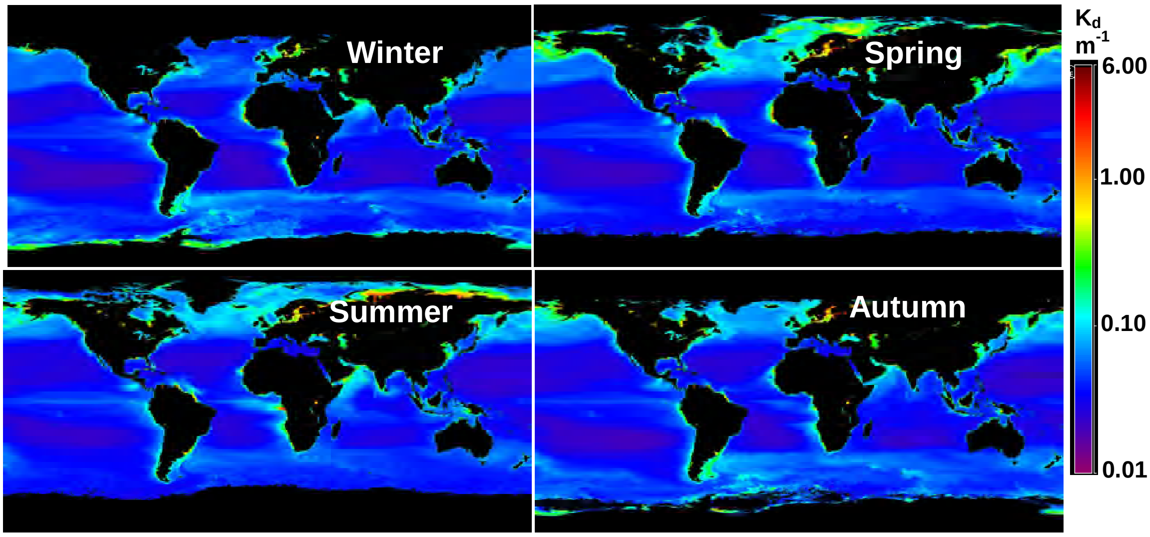

Figure 3.2. Seasonal composites on global K_d distribution as obtained from SeaWiFS

3.1.3 AOD

In general, AOD concentration in atmosphere over the world oceans is low during autumn (Figure 3.3). However, a zone of comparatively dense AOD is observed over the tropical regions of the Atlantic and Indian Oceans during this season. This zone gets intensified by winter over the eastern side of the Atlantic Ocean. By spring, the zone further becomes denser and extends towards Pacific Ocean after passing over the north Indian Ocean. The AOD concentration becomes the highest during summer with its epicenter off the Arabian Peninsula. Thus the atmosphere over the western Arabian Sea possesses the highest AOD concentration among all the world oceanic regions during summer. This observation also implies that the seasonal variability is highest over the western Arabian Sea. The present observations are in concurrence with the earlier studies (Hsu et al., 2012 and therein; Zhu et al., 2007).

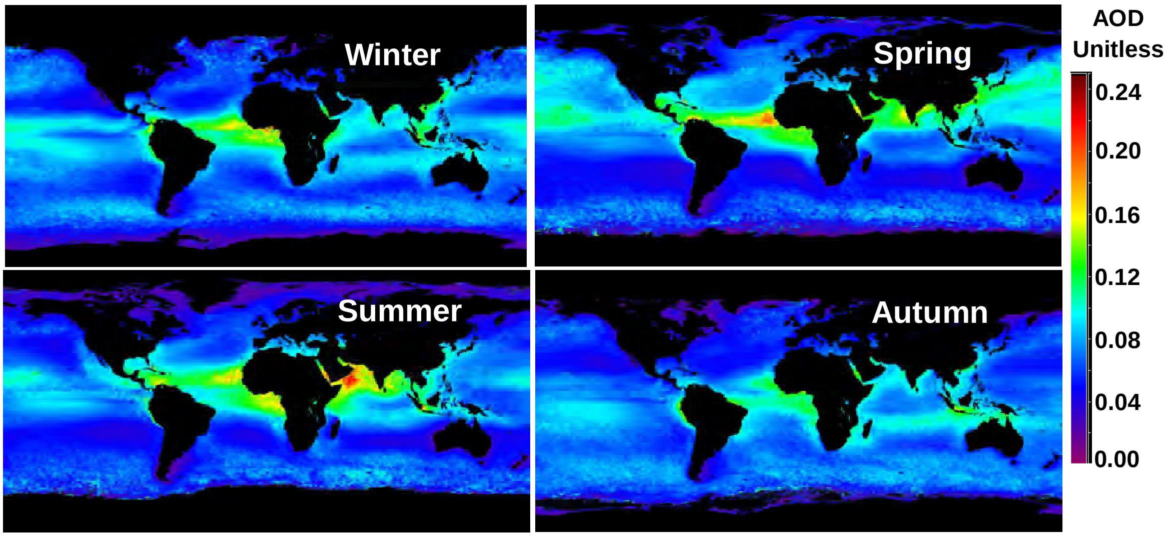

Figure 3.3. Seasonal composites on global AOD distribution as obtained from SeaWiFS

3.2 Climatology of Chl *a*, K_d and AOD in the study area

Distribution of Chl *a*, K_d and AOD are examined to understand the climatology of these parameters in the study area. In this regard, the monthly averages generated from the data provided by the sensors SeaWiFS (Fig 3.4) and MODIS_AQUA are used (Figure 3.5).

In general, the values of Chl *a* are high near the coast during all the months, which decreased towards offshore (Figure 3.4.a). During May, a marginal increase in Chl *a* sets in and this trend continues up to August. In addition, a significant cross-shore gradient is established in the southern area by June, which moves northward to encompass the entire study area by August and undergoes gradual decay during subsequent months. Similar to its intensification, the decay also starts from the south and moves northward. The gradient starts weakening from September and disappears from the southern area by October. By November, it fades off the northern area too. Thereafter, low Chl *a* values continue up to April all through the area.

Present observation of the northward propagation of Chl *a* gradient with the advance of the southwest monsoon and occurrence of higher values of Chl *a* during peak of south-west monsoon is in good agreement with the *in situ* Chl *a* observation by Habeebrehman et al. (2008). The high values Chl *a* during the southwest monsoon is consistent with Banse et al. (1996), Goes et al. (1992) and is observed to be the resultant of enhanced nutrient supply from the subsurface.

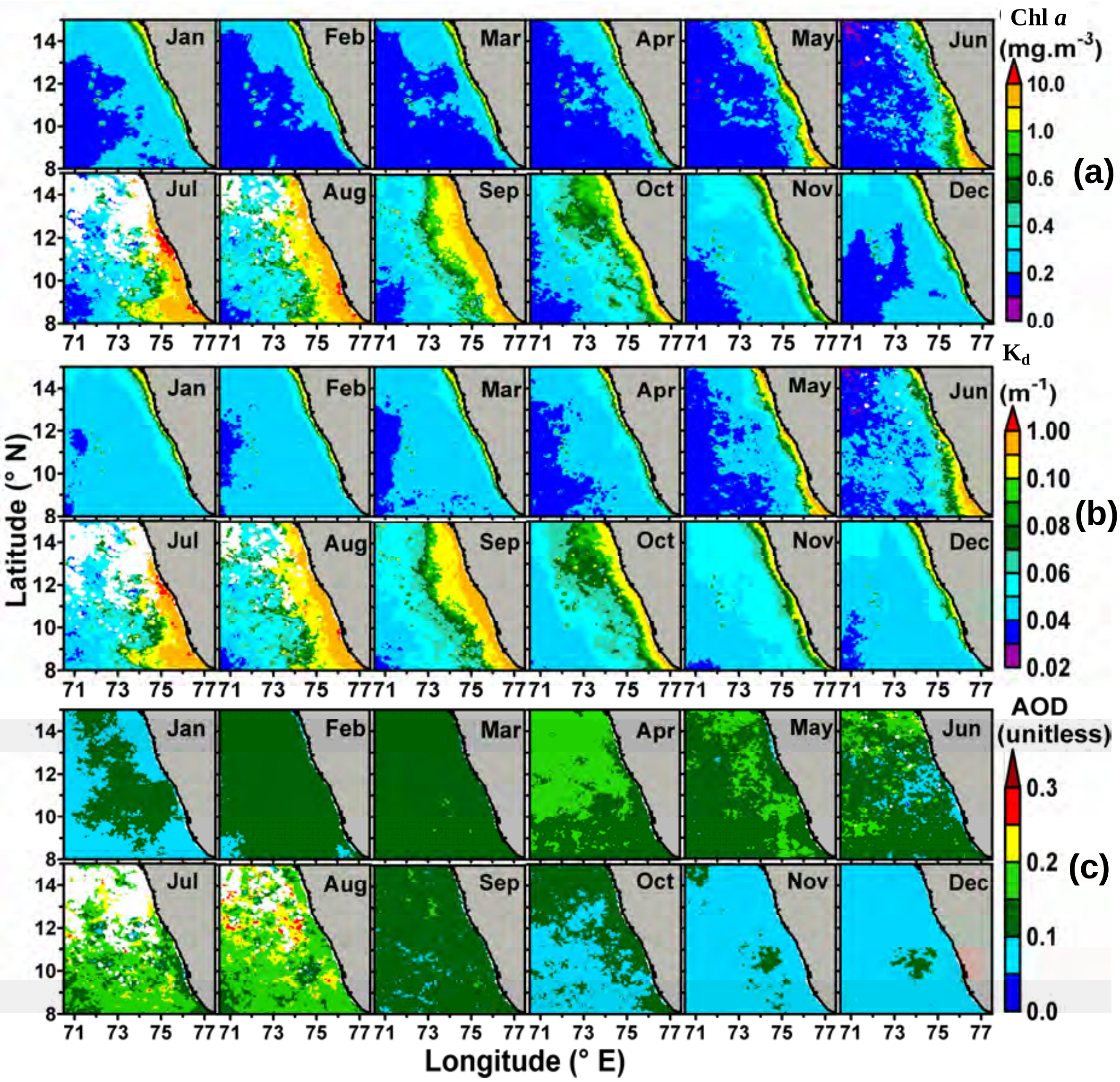

Figure 3.4. Monthly climatology of (a) Chl *a*, (b) K_d and (c) AOD from SeaWiFS off the southwest coast of India. The upper panels represent the distribution pattern during January to June and the lower panel during July to December.

Similar to Chl *a*, K_d is also high near the coast during all the months and decreased towards offshore (Figure 3.4.b). Here also, cross shore gradients are present throughout the year, but it is prominent during the southwest monsoon. The monthly spatiotemporal variability for Chl *a* and K_d has a close resemblance. Thus, it is concluded that the Chl *a* and K_d in the study area are strongly coupled. This similarity in the variability of Chl *a* and K_d deserves special attention (Figure 3.4 and 5). Though, K_d depends on Chl *a* and organic and inorganic particles (Kirk, 1994), it appears, that, K_d is more associated with Chl *a* distribution in the study area. Therefore, a regression analysis is carried out with monthly data to establish this correlation (Figure 3.6). This analysis clearly indicates a significant linear relation between Chl *a* and K_d ($r^2 > 0.90$) throughout the year.

The AOD distribution showed an annual cycle with gradual increase from January (~0.1) to August (~0.2) and a decrease thereafter up to January (Figure 3.4.c). Maximum value is observed during July / August and minimum during November / December. The high AOD values during the southwest monsoon are already reported by Li and Ramanthan (2002), Nair et al., (2012). The coincidence of higher values of AOD, Chl *a* and K_d during the southwest monsoon are noteworthy.

A comparison study is carried out using MODIS_AQUA data with that of SeaWiFS (Figure 3.5). The result shows that Chl *a*, K_d and AOD data from MODIS_AQUA sensor have good similarity with that of SeaWiFS.

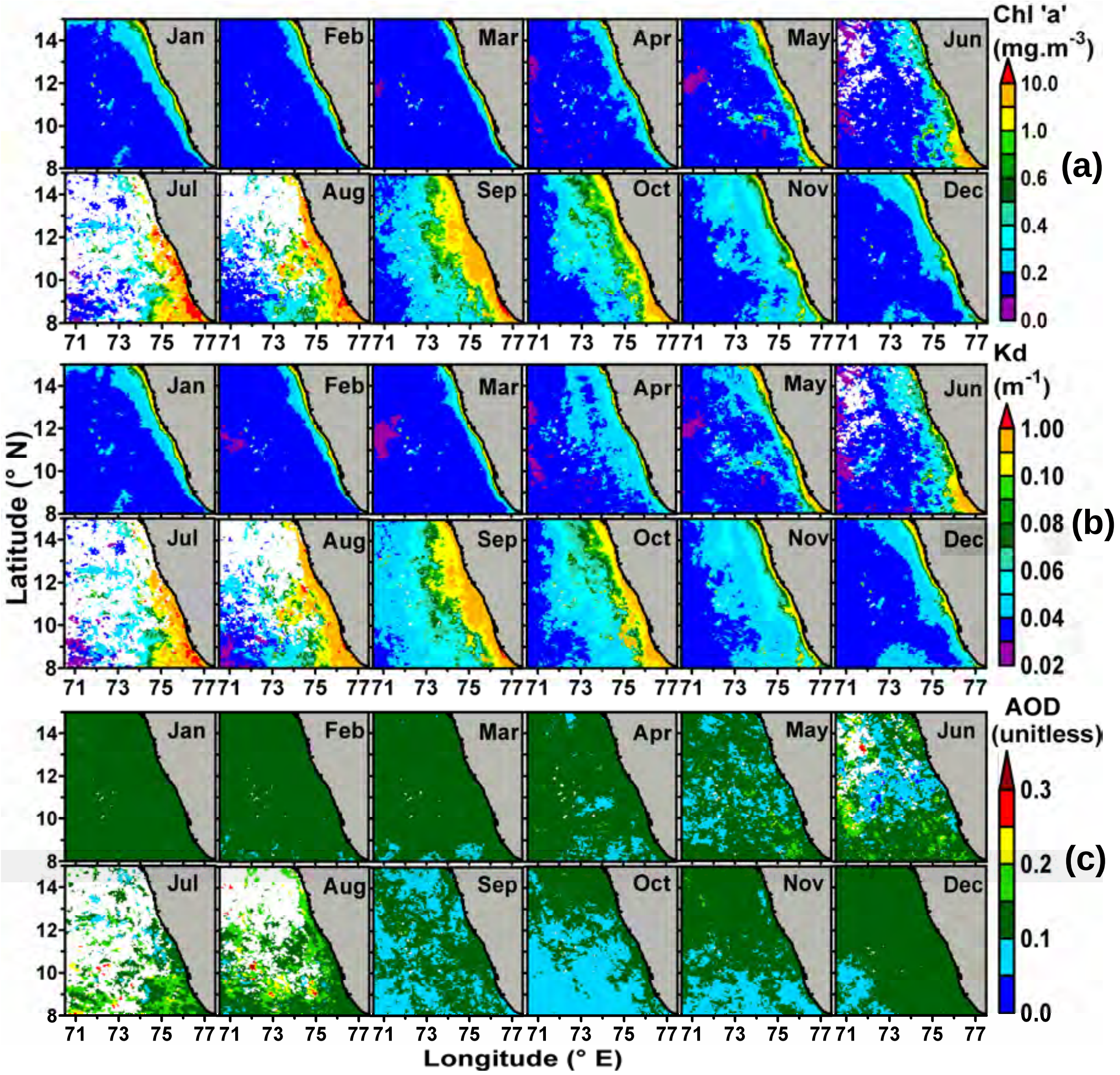

Figure 3.5. Monthly climatology of (a) Chl *a*, (b) K_d and (c) AOD of MODIS_AQUA.

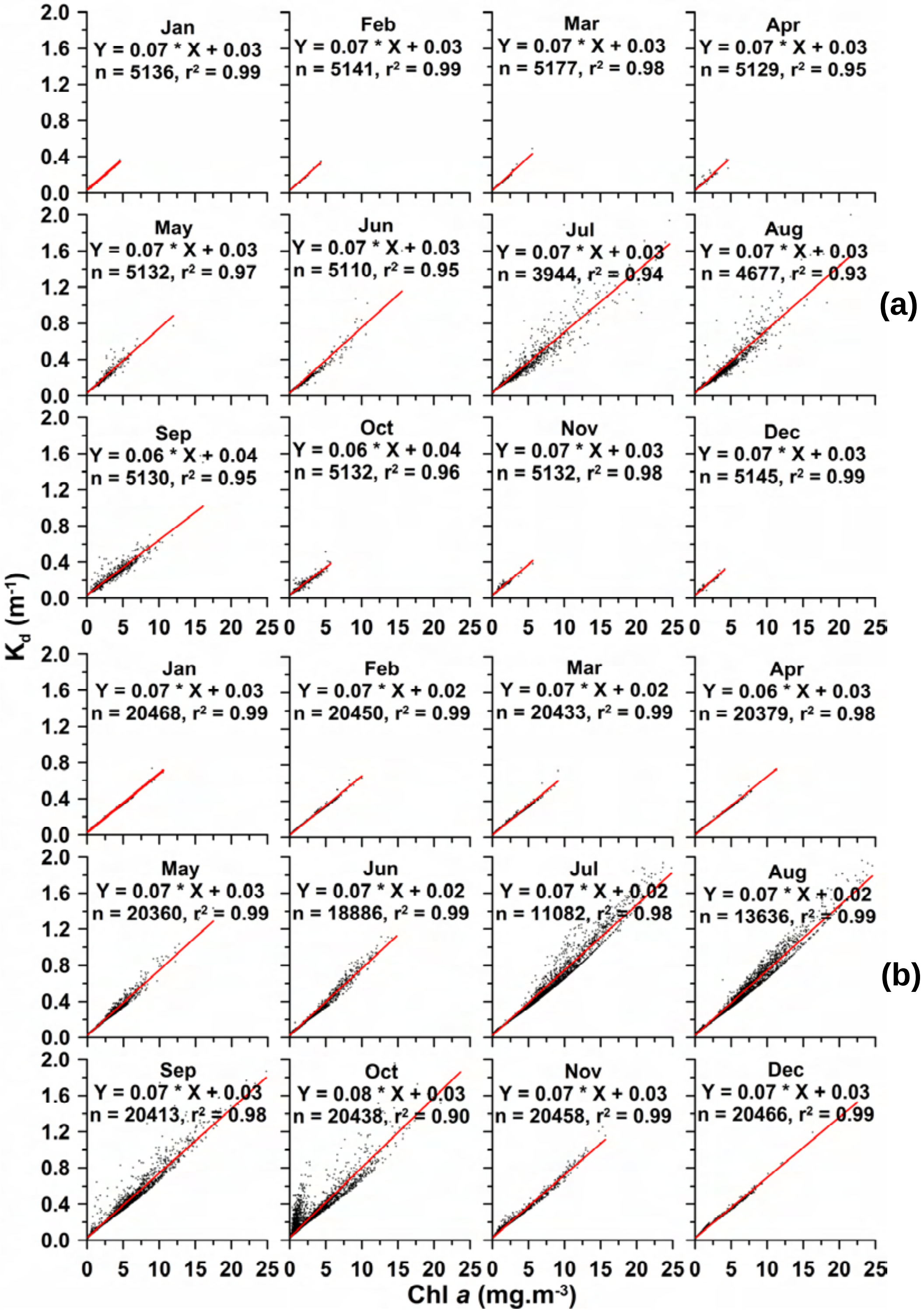

Figure 3.6. Regression analysis between Chl *a* and K_d of (a) SeaWiFS and (b) MODIS_AQUA

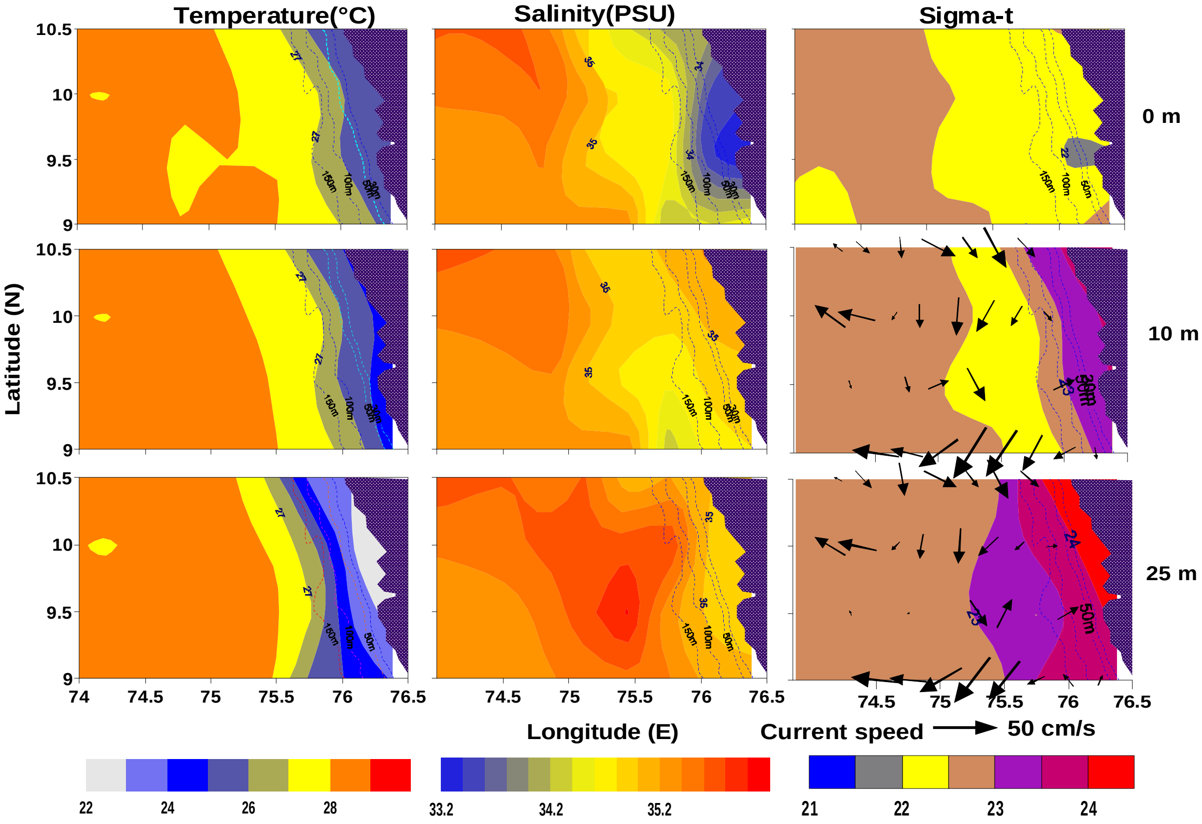

Figure 3.7. Topography maps of temperature (^{o}C), salinity (PSU) and sigma-t at 0, 10 and 25 m. (Source: Sanilkumar et al., 2004)

A significant cross-shore gradient was found in the distribution of Chl *a* and K_d along the southwest coast of India during the southwest monsoon. Similar gradients on other oceanographic parameters viz. temperature, salinity and sigma-t have been reported in the study area based on *in situ* observations (Sanilkumar et al., 2004). They also observed that the isolines of the above parameters were at three depth levels (0, 10 and 25 m) were running parallel to the coast and were closely spaced towards the coast, indicating a significant gradient across the shelf occurred due to prevailing upwelling (Figure 3.7; reproduced from Sanilkumar et al., 2004). Such gradient can be named as upwelling front (Beletsky et al., 1997). The front develops because the vertical movement of subsurface waters is more towards coast compared to the offshore region during the upwelling.

Other oceanic regions too exhibit similarity in SST and Chl *a* distribution pattern during specific seasons, including off northern California (Denman and Abbott, 1994; Doney et al., 2003; Hood et al., 1990), northwest Atlantic (Stegmann and Ullman et al., 2004), southwestern Atlantic ocean (Saraceno et al., 2005), Mid-Atlantic Bight (He et al., 2010); off Iberian Atlantic (Smyth et al., 2001); south Africa and Namibia (Denmarcq et al., 2003).

The similarity between Chl *a*, K_d and temperature distribution in the study area indicates that, these parameters may also to be tried out to study the upwelling features during the upwelling period instead of SST, which is the most conventionally accepted parameter. In order to verify this, SST data from AVHRR and MODIS_AQUA are utilised.

3.3 SST

Monthly climatology of SST from AVHRR and MODIS_AQUA along the southwest coast of India is presented (Fig 3.8.a-b). It is evident that there is a high SST (> 29.5^oC) during April and May that decreases from June to August. In addition, there is a strong cross-shore gradient near the coast during July and August which intensified during September. Cross-shore gradient in SST during the months of July / August could be captured from both the sensors MODIS_AQUA and AVHRR.

3.4 Upwelling

Upwelling brings dense, cold and nutrient-rich subsurface waters to the surface (Figure 3.9). As seen in the Figure 3.5, the temperature drops and cross-shore gradient develops in the study area. In addition, nutrient-rich waters upwelled will enhance primary productivity in the upper layers and will be evident in Chl *a* concentration (Banse, 1987; Ryther, et al; 1966; Wiggert et al, 2005). Thus, a positive relation between upwelling index and Chl *a* exists during upwelling (Lluch-cota, 2000). The phytoplankton blooms normally occurs 3 - 7 days after the upwelling event (Wilkerson et al., 2006). Recent studies have shown that the supply of nutrients from atmospheric deposition can also increase the productivity (Duce and Tinsdale, 1991; Fan et al., 2006; Jickells et al., 2005; Mahowald et al., 2005; Mahowald et al., 2009; Santos 2010; Sholkovitz et al., 2009).

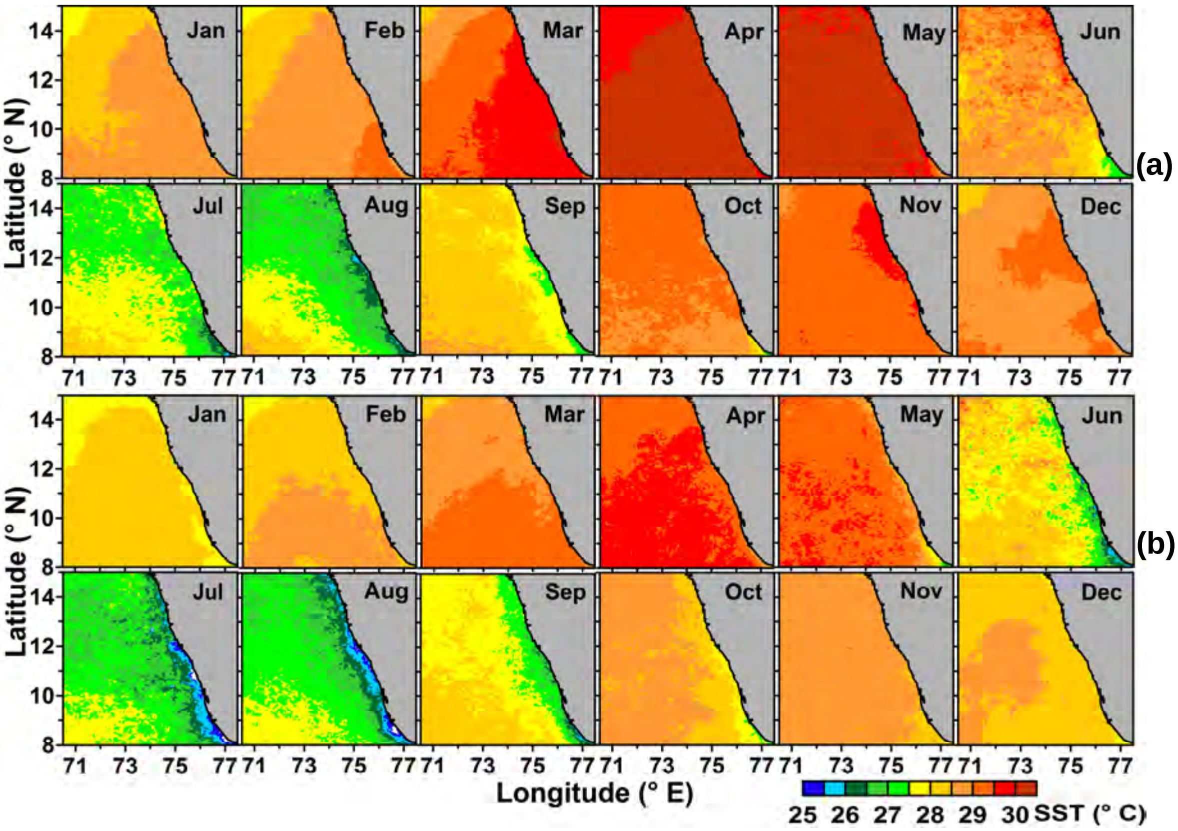

Figure 3.8. SST climatology from (a) AVHRR and (b) MODIS_AQUA

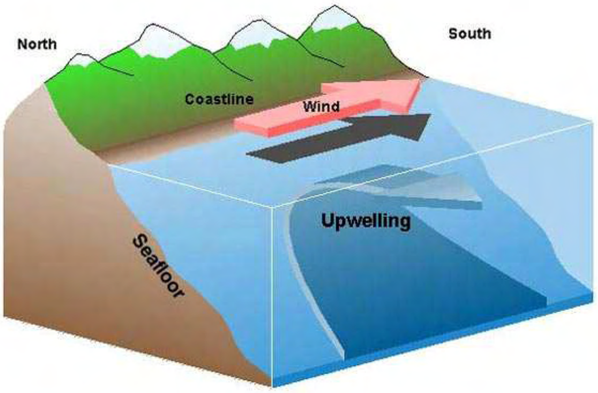

Figure 3.9. Schematic diagram of upwelling in the northern hemisphere. (Source: Wikipedia)

3.4.1 Upwelling off the southwest coast of India

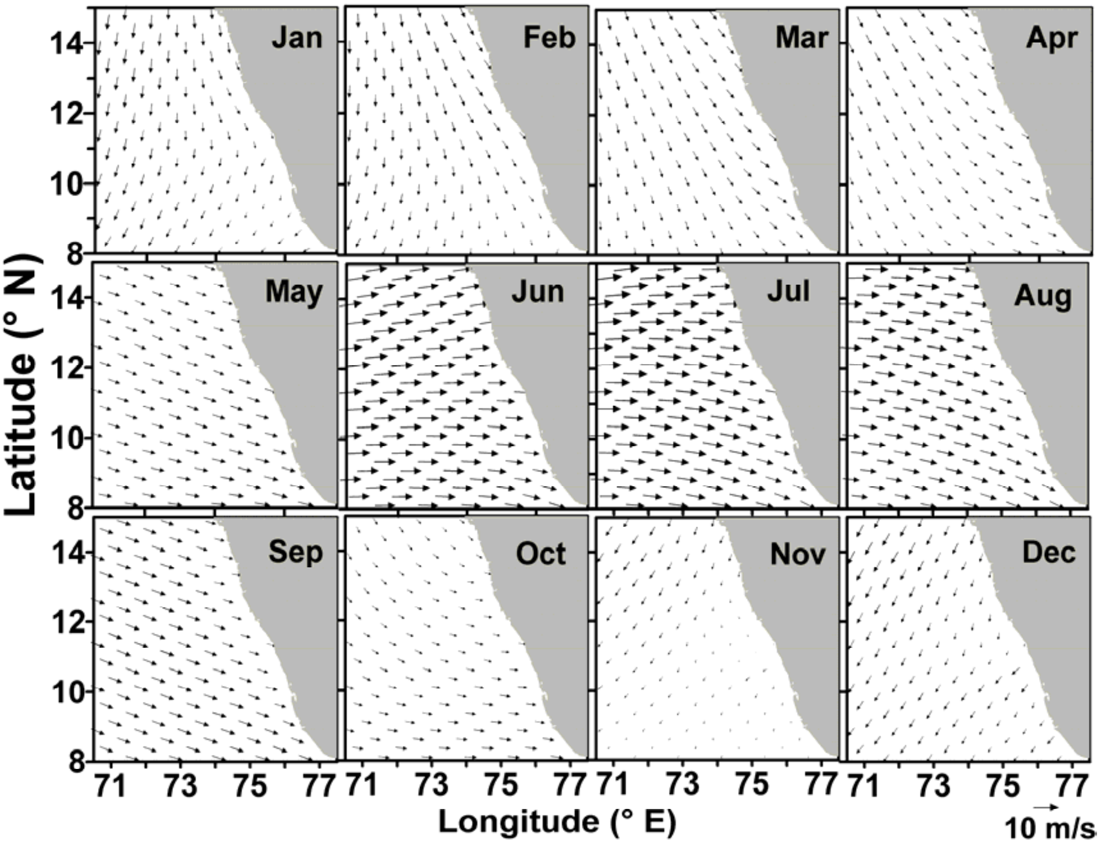

Figure 3.10. Surface wind climatology utilising QuikSCAT data during July 1999 – November 2009.

It is well known that upwelling occurs annually off the southwest coast of India (Banse, 1959; Banse 1987; Johannessen et al., 1987; Sharma, 1978). In the northern hemisphere, upwelling commences when the alongshore winds and surface currents flow with the coast on left side. Therefore, to show the influence of these local forcings on seasonal upwelling, data on the surface winds and currents are examined.

In general, the winds prevailing over the area during November – January are northerly to northeasterly (Figure 3.10). By February, the coastal winds change to northwesterly, while northeasterly winds persist over the offshore. From March to May, the northwesterly winds dominate the entire area, but change to nearly westerly during June / July and become again northeasterly in the subsequent months. Wind speed is higher during June - August. Thus, it is to be noted that even though wind speed / direction change seasonally, winds are favourable for upwelling near the coast especially towards south (northwesterly) along with higher speed during May – September. Mathew (1983) and Shetye et al. (1990) have already reported that very near to the coast, the winds are favourable for upwelling during the southwest monsoon period. The reason for "why upwelling occurs only during the southwest monsoon season?" is examined based on the surface currents also. The ship drift data compiled by UK meteorological office during the year 1900-1993 have been utilised for this study (Figure 3.11). It was observed that the West India Coastal Current (WICC) turns southward by February and is faster during May – September. While, WICC is northward during November – December, it is also a continuation of the EICC in the Bay of Bengal (Kumar et al., 2004; Shankar et al., 2002). Therefore, based on the surface currents, they are highly favourable during the southwest monsoon period, when the WICC is southward and faster. Thus, it can be inferred that both the winds and currents are favorable for upwelling during the southwest monsoon period. Further, it is to be noted that propagation of long period waves (Kelvin and Rossby wave) also contribute to upwelling in the area (Brandt et al., 2002; Kumar and Sanilkumar, 2005; McCreary et al., 1993; Shankar and Shetye, 1997; Shankar et al., 2002; Wu and Kirtman, 2007; Yang et al., 1998).

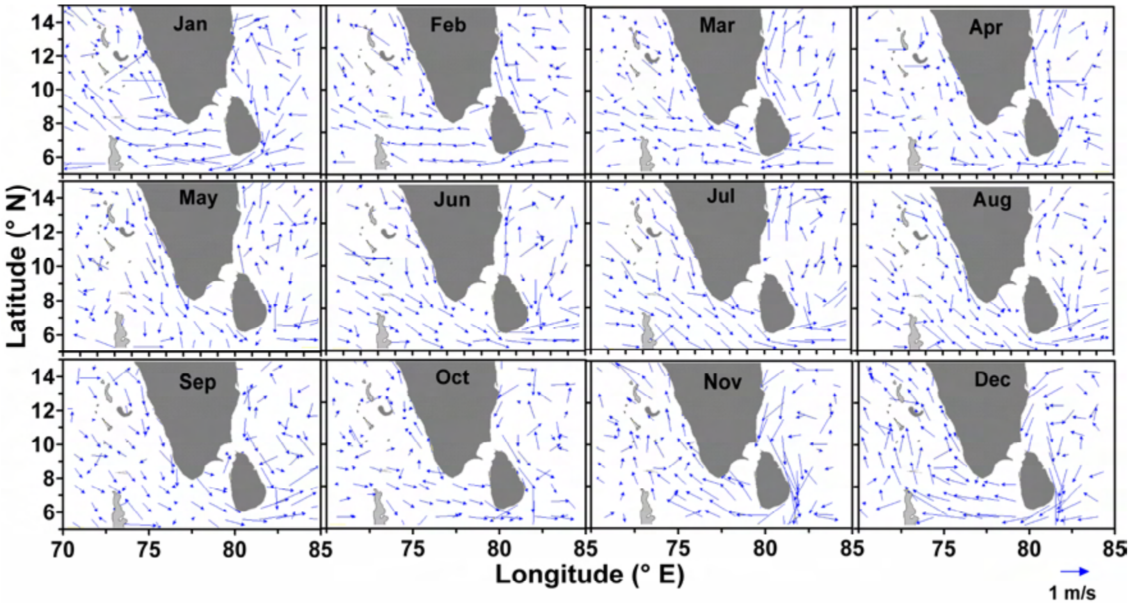

Figure 3.11. The surface current climatology utilizing ship drift data during 1900 – 1993

In addition, to southward current / wind and low SST, low SSHA are reported in the oceanic regions during upwelling period (Shankar et al., 2002). Hence, the climatology of SSHA obtained from merged ERS and TOPEX are utilized here to view the SSHA distribution.

In addition, to southward current / wind and low SST, low Sea Surface Height Anomaly (SSHA) is another feature in the study area during upwelling period

(Shankar et al., 2002). Hence, the climatology of SSHA obtained from merged ERS and TOPEX are utilized here to view the SSHA distribution.

3.4.2 SSHA

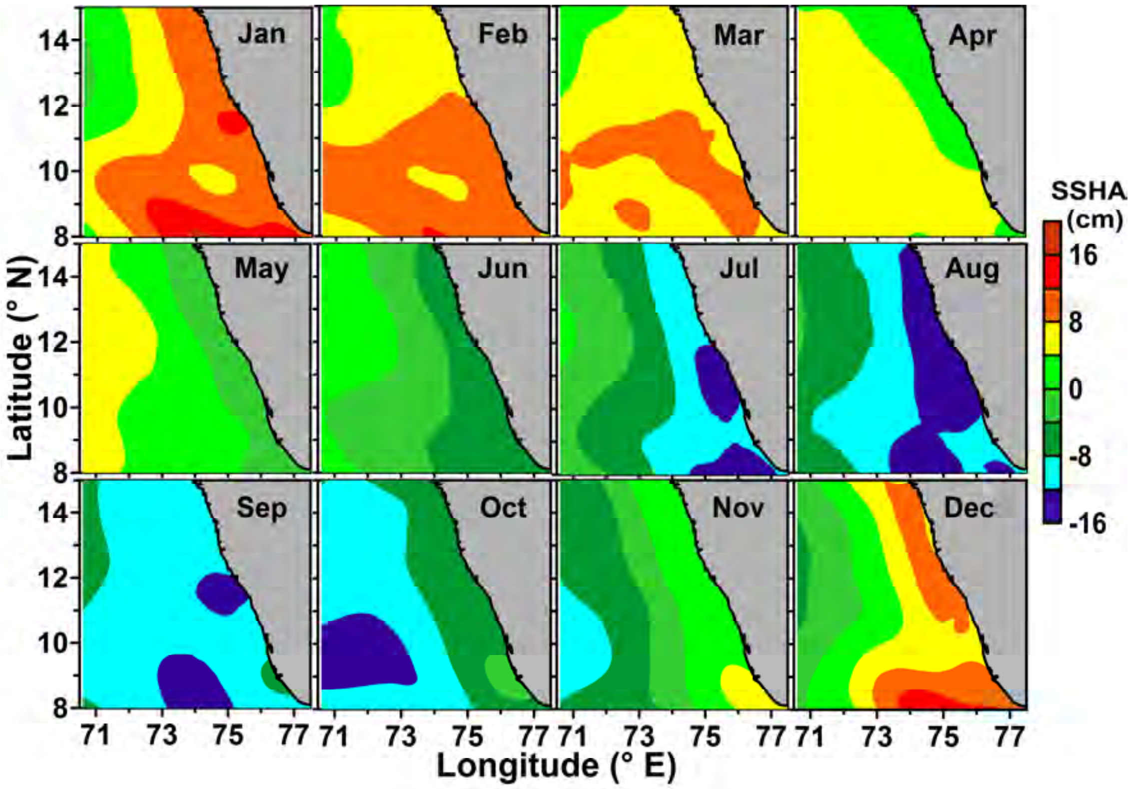

Figure 3.12. Climatology of Sea Surface Height Anomaly (SSHA) utilising merged data from TOPEX / ERS / Jason - 1 obtained during 1992 – 2010

In general, low values of SSHA are observed in the area during the southwest monsoon period (Figure 3.12). By May, a narrow band of low SSHA (< 0 cm) appears very near to the coast. By June, this band begins to widen along with further lowering in SSHA from south to north and continues up to August. It is also observed that the rate of change is faster towards south. Accordingly, the broadest SSHA band with lowest values occurs towards south. The reverse process i.e. evolution towards positive SSHA anomaly commences by September and by November SSHA becomes positive all along the coast. SSHA further increases in the followings months and attains the highest values by January. Towards south, the Laccadive High / Low are the part of this SSHA evolution (Bruce et al., 1998, Shankar and Shetye, 1997).

Observations from the above analysis brought out that the high Chl *a* and K_d (Chl *a* and K_d is represented mostly by Chl *a* / K_d in the subsequent portion for brevity) during July – September coincides with the features of the upwelling viz. low SSHA, faster southward current and low SST. Thus the study confirms the correlation of upwelling on the increase of Chl *a* / K_d in the study area.

3.5 Empirical equation between SST and Chl *a* / K_d

Similarity on the distribution of Chl *a* / K_d to that of SST during the upwelling period indicates that there may be an underlying relation between the parameters and the same may be possible to be represented in terms of parametric equations. In order to verify the above concept, regression analysis was carried out utilising collocated data points available from the monthly climatology of SST generated from MODIS_AQUA and of Chl *a* / K_d from SeaWiFS as well as MODIS_AQUA (Figure 3.13-14). The corresponding empirical equations along with number of data and correlation coefficient (r^2) are provided in the respective figures.

3.5.1 Results and discussion

In general, there exists an inverse relation between SST and Chl *a* during the southwest monsoon period (Figure 3.13.a). This relation is found exponential in nature. Hence, plots are taken on semi-logarithmic scale. A linear curve in a semi-logarithmic plot confirms the existence of an exponential relation between the parameters. The relation is very evident during July – September from the maxima of r^2 (~ 0.5) and slope of the curve. In June, the trend is weak (r^2 =0.12) and is dominated by low Chl *a* (< 0.1mg.m^{-3}), which are denoted by red dots. Hence, the experiment was repeated after removing these low Chl *a* points, which yielded good r^2 (0.63) value and more slope on the linear curve. Similar analysis was carried out for October also and found the relation for this month is also comparable to that of June. Therefore, from the above analysis, it is clear that June and October months are to be considered as transition periods.

A logarithmic relation between SST and Chl *a* is reported in the Pacific Ocean and Sargasso Sea (http://disc.sci.gsfc.nasa.gov). However, in the upwelling zone of Equatorial Atlantic Ocean (Perez et al., 2005), western Arabian Sea (Goes et al., 2005) and Vietnam (Yuan-Jian et al., 2012) the relation is linear during summer.

It is evident that, K_d in the study area is strongly associated with Chl *a* (Figure 3.3). Hence a regression analysis is carried out to examine whether the relation is true between SST and K_d also (Figure 3.13.b). The test proves that the equations between SST and K_d follow similar trend, which has been observed in SST - Chl *a* equation.

For inter-comparison between data sets of SeaWiFS and MODIS_AQUA, the regression analysis is carried out with the later one also (Figure 3.14). The results are quite comparable in both the cases of Chl *a* and K_d, indicating that both the data sets from different satellites can be utilised to study ocean variability in the study area.

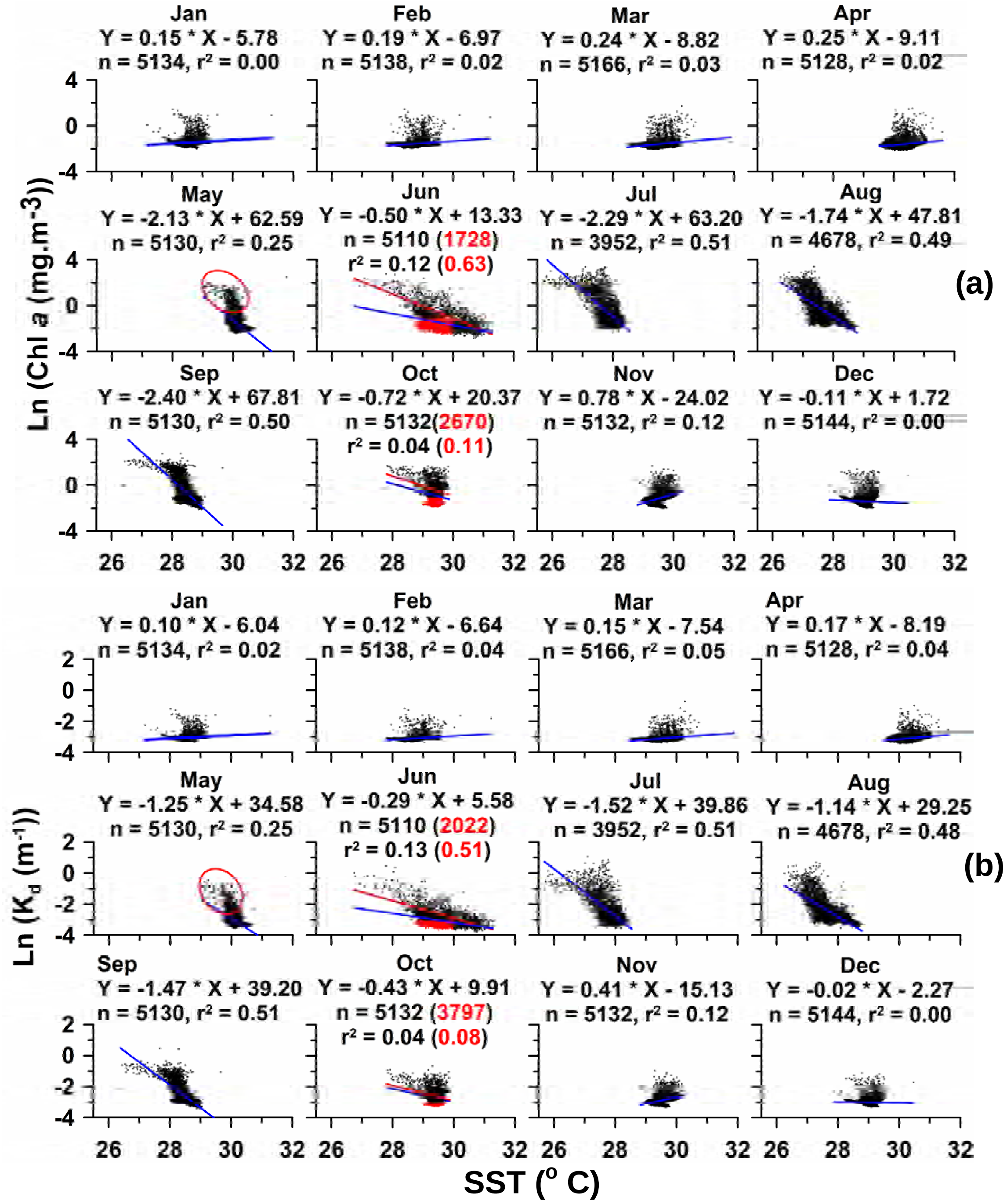

Figure 3.13. Regression analysis between SST from MODIS_AQUA and (a) Chl *a* and (b) K_d from SeaWiFS

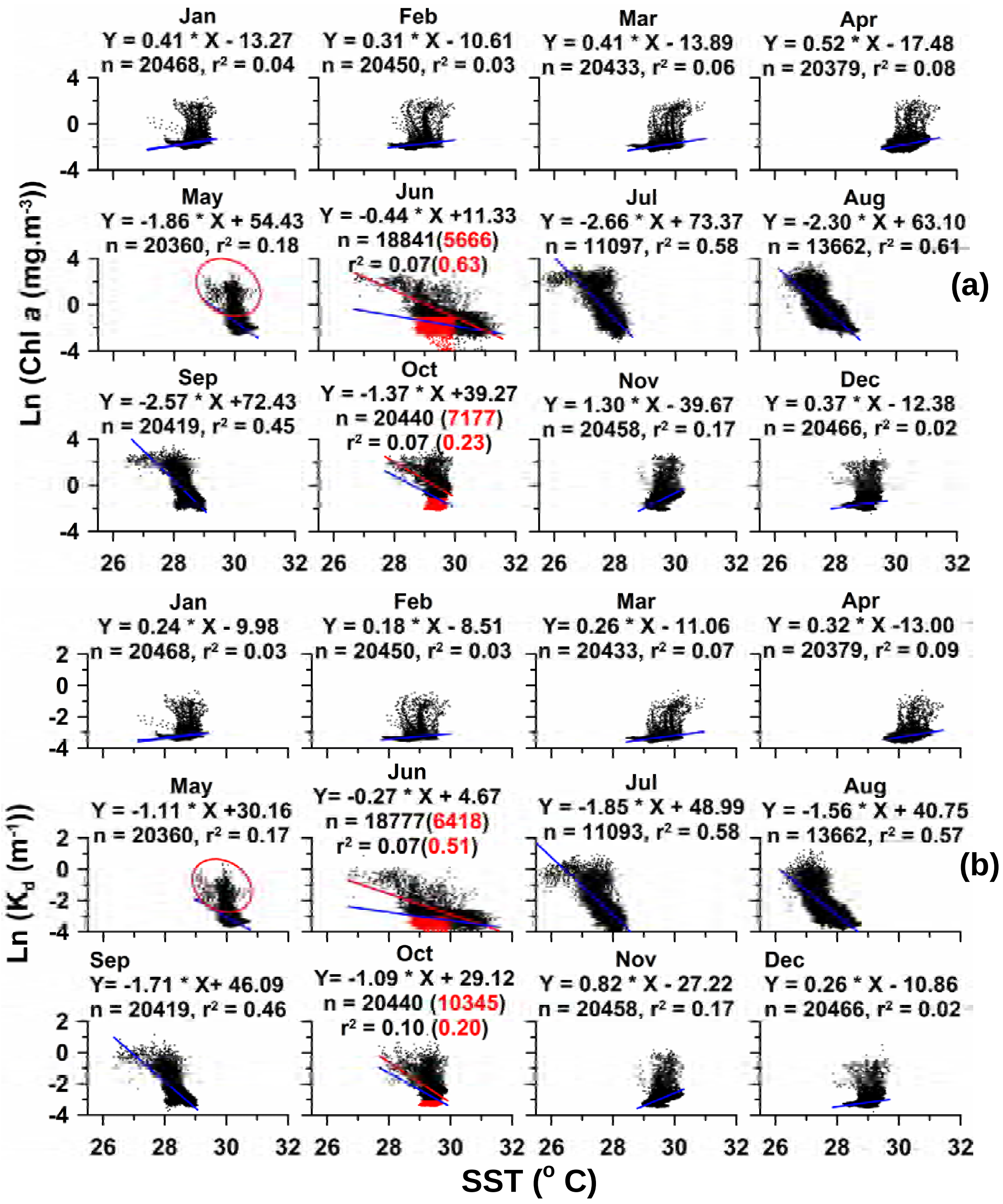

Figure 3.14. Regression analysis between SST from MODIS_AQUA and (a) Chl *a* and (b) K_d from MODIS_AQUA

Chapter 4

Temporal variability of Chl a, K_d and AOD

Most of the oceanographic and atmospheric parameters exhibit temporal variability. Therefore, this Chapter deals with the time series observations on Chl *a*, K_d and AOD as obtained from SeaWiFS images during September 1997 – December 2010. Previous Chapter has established the existence of large spatio-temporal variability in the study area especially during the southwest monsoon. In order to explain this, two subareas (3^o longitude X 3^o latitude grids) lying to the south and north of the study region were selected and named as Zone 1 and Zone 2 (Figure 2.2). In addition, three smaller areas (0.5^o longitude X 0.5^o latitude grids) representing coastal and offshore regions of the south (off Thiruvananthapuram), central (off Kozhikode) and north (off Karwar) locations were selected to understand the regional variability. They are named as Grid 1, Grid 2 and Grid 3 and also suffixed by ‘a’ and ‘b’ to demarcate coastal and offshore respectively. It is to be mentioned here that ocean colour data are capable of depicting variability at closer spatial resolution (Table 1.1).

Monthly Chl *a*, K_d and AOD were averaged for all the selected areas to explain their temporal variability. The influence of local environmental conditions (wind, ocean current, SSH and SST) on these parameters were also examined. Further, monthly anomalies of each of these ocean colour parameters were extracted from the time series data to examine their response to global climatic oscillations (ENSO /

IOD). Moreover, Hysplit model was utilised to understand the influence of aerosols from remote areas on to AOD anomaly. The oscillatory modes embedded in these parameters were delineated using EMD.

4.1 Intra- and inter-annual variability of Chl *a*, K_d and AOD

4.1.1 Area 1

In general, Chl *a* in Area 1 showed high values (> 1.20 $mg.m^{-3}$) during June – September and very low values (~0.25 $mg.m^{-3}$) during December – April. May and October / November can be considered as transition periods (Figure 4.1). The above three phases complete an annual cycle that recurs, while peak values occur during one of the months and found to vary each years between July and September (Table 4.1). The intra- and inter-annual variations of K_d were similar to that of Chl *a* with high value (> 0.12 m^{-1}) during June-September and low (~0.05 m^{-1}) during December – April. Although, the AOD followed an annual rhythm; its peak (0.08-0.23) was recorded (April) much early compared to that of Chl *a* and K_d. The fluctuations in AOD were high unlike that for Chl *a* and K_d and became low (0.06-0.13) during the northeast monsoon, indicating a significant intra- and inter-annual variability.

The annual cycle exhibited by Chl *a* was consistent with the earlier observations (Banse, 1987; Banse and English, 2000; Goes et al., 1992). All these observations showed an increase in Chl *a* which was attributed to the nutrient supply from the subsurface levels due to upwelling during the southwest monsoon period. In the following section, the corresponding supporting parameters representing oceanographic and atmospheric conditions were examined, to understand their influence on Chl *a* distribution.

The supporting parameters showed that in general, low SST / SSHA and high equatorward components of currents and winds existed during the southwest monsoon. SST was found to follow a bi-annual oscillation, with lowest value in one of the months during the southwest monsoon, whereas, SSHA showed an annual cycle again with minima in one of the months during the southwest monsoon. The surface alongshore currents change its direction poleward during the northeast monsoon, but the alongshore winds has equatorward components irrespective of the season (0 to -5 ms^{-1}). The equatorward winds intensified during the southwest monsoon, except during 2006 and 2007. Thus, in general, the supporting parameters showed maximum equatorward current / wind and low SST / SSHA during the southwest monsoon, with their peak in one of the months similar to Chl *a* and K_d. In this context, it is to be noted that this low SST / SSHA and strong equatorward current / wind are associated features of upwelling (Bruce et al., 1998; Shankar and Shetye, 1997; Shankar et al., 2002). Therefore, the co-occurrence of high Chl *a* / K_d along with the above maxima / minima of the supporting parameters during the southwest monsoon period suggests close linkage to them with upwelling. Further, the low SST and highest Chl *a* / K_d values co-occurred with the highest southward current / wind in the same month or within the differences of one month during most of the years. This observation showed the increase in Chl *a* / K_d would have induced by upwelling as these factors are favorable for upwelling.

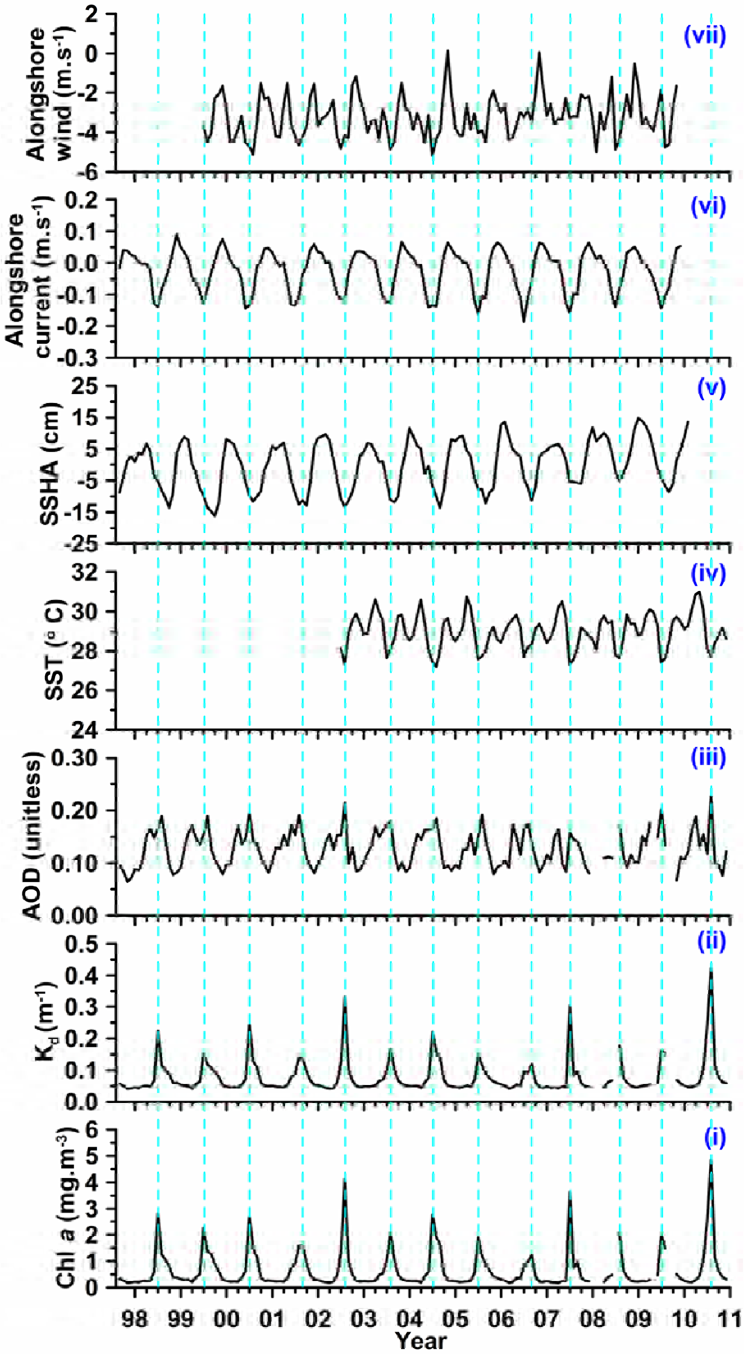

Figure 4.1. Temporal variability in (i) Chl *a*, (ii) K_d, (iii) AOD, (iv) SST, (v) SSH, (vi) alongshore surface current and (vii) alongshore surface wind averaged for Area 1. The dotted vertical lines denote peak values of Chl *a*. The gap indicates non-availability of data

High values of AOD during the southwest monsoon, co-existed with high *Chl a* / K_d. The influence of AOD to increase Chl *a* / primary production was reported in the Atlantic Ocean, Pacific Ocean, southern ocean, north western Arabian Sea (Behrenfeld et al., 1996; Boyd et al. 2000; Fitzwater et al., 1996; Hutchins et al., 2002; Santos, 2010; Witter et al, 2000). A similar influence of AOD on the Chl *a* is possible in this area also.

Table 4.1. Months during which maxima / minima occurred in Chl *a* , K_d, AOD, SST, SSHA, current and winds in Area 1

Year	Maximum			Minimum SST	Lowest SSHA	Maximum	
	Chl *a*	K_d	AOD			southerly current	southward wind
1998	Jul	Jul	Aug	-	Oct	Jul	-
1999	Jul	Jul	Aug	-	Oct	Jul	Aug
2000	Jul	Jul	Jul	-	Aug	Jun	Aug
2001	Sep	Aug	Aug	-	Oct	Jul	Aug
2002	Aug	Aug	Aug	Aug	Aug	Aug	Jul
2003	Aug	Aug	Aug	Jul	Sep	Aug	Aug
2004	Jul	Jul	Aug	Aug	Sep	Jun	Jul
2005	Jul	Jul	Aug	Jul	Sep	Jul	Sep
2006	Sep	Sep	Aug	Jul	Sep	Jul	Mar
2007	Jul	Jul	Apr, Jul	Jul	Oct	Jul	Mar
2008	Aug	Aug	Aug	Aug	Aug	Jul	Feb
2009	Jul	Jul	Jul	Jul	Sep	Jul	Aug
2010	Aug	Aug	Aug	Aug	-	-	-

4.1.2 Zone 1 and 2

In general, Chl *a* in Zone 1 and 2 followed an annual cycle, with high values during the southwest monsoon (Figure 4.2). Similar to that of Area 1, the maximum Chl *a* (> 1.4 $mg.m^{-3}$) was observed only for a short period between July and September (Table 4.2-3), which showed significant inter-annual variability, especially in Zone 2 (0.6-7.0 $mg.m^{-3}$) compared to that of Zone 1 (2.5 – 7.0 $mg.m^{-3}$). Mostly, the month of peak of Chl *a* was same in both the zones. However, in certain years the highest values developed in Zone 2 with one or two months lag. K_d (0.04-0.60 m^{-1}) and AOD (0.06-0.28) in both zones exhibited intra- and inter-annual variability. The supporting parameters revealed upwelling condition during the southwest monsoon in Zone1 and 2, which were similar to that of Area 1. Lowest SST / SSHA and strong southerly current existed in one of the months during the southwest monsoon, which co-occurred with high Chl *a* / K_d.

4.1.3 Grids 1-3

In general, Chl *a* in Grid 1a followed an annual cycle similar to that of Area 1 (Figure 4.3). However, in this case, high values (0.50-21.0 $mg.m^{-3}$) were found fluctuating and exist for a longer duration (May – October). The highest value in a year was observed again in one of the months during June – September (Table 4.4). The peaks of Chl *a* during August 2002 (21.0 $mg.m^{-3}$) and 2010 (15.5 $mg.m^{-3}$) as well as the low Chl *a* during August 2007 (2.0 $mg.m^{-3}$) indicated significant inter-annual variabition. However, Chl *a* variation in Grid 1b was not visible due to very low values. K_d variability in Grid 1a and Grid 1b also followed the same pattern of Chl *a*. AOD over both grids followed an annual cycle similar to that of Area 1.

The results generally showed the occurrence of low SST / SSHA and strong equatorward current / wind in Grid 1a and Grid 1b during the southwest monsoon, as obserevd in the previous cases. The winds over Grid 1a and Grid 1b followed an annual cycle with strong equatorward flow (<-3$m.s^{-1}$) during the southwest monsoon that weakened (>-1$m.s^{-1}$) during the northeast monsoon. The differences in SST (~-

2^{o}c) and alongshore winds (~-2ms^{-1}) during the southwest monsoon were quite significant between two grids, with lower SST and stronger equatorward wind in Grid 1a.

The inter-annual variability on annual peaks of the different ocean colour parameters and supporting variables in Grid 1a revealed good correlation between the highest Chl *a* / K_d and lowest SST for most of the years. However, unlike for the larger areas, the co-existence of Chl *a* with the lowest SSHA and southerly current / wind was not evident here.

Chl *a* (0.4-15.0 mg.m^{-3}) / K_d (0.06-1.20m^{-1}) in Grid 2a showed an annual cycle similar to that of Grid 1a, with highest values for a short period during June – September (Figure 4.4). Grid 2b had low Chl *a* (~0.30 mg.m^{-3}) / K_d (~0.05 m^{-1}) values were comparable to that of Grid 2a. AOD also followed a similar annual cycle over both Grids 2a and 2b. Upwelling signatures on SST and SSHA were quite evident in Grid 2a during the southwest monsoon, with their lowest values for a short period similar to the other areas (Table 4.5).

A major difference in the observations in Grid 3a was that the magnitude of variability in Chl *a* and K_d was less compared to that of Grids 1a and 2a (Fig. 4.5). The seasonal variability reflected in the time series data on SST, SSHA and alongshore currents. High Chl *a* / K_d coincided with upwelling signatures viz. low SSHA / low SST, strong equatorward current / winds, indicating the increase in these parameters were related to upwelling as in the other areas (Table 4.6).

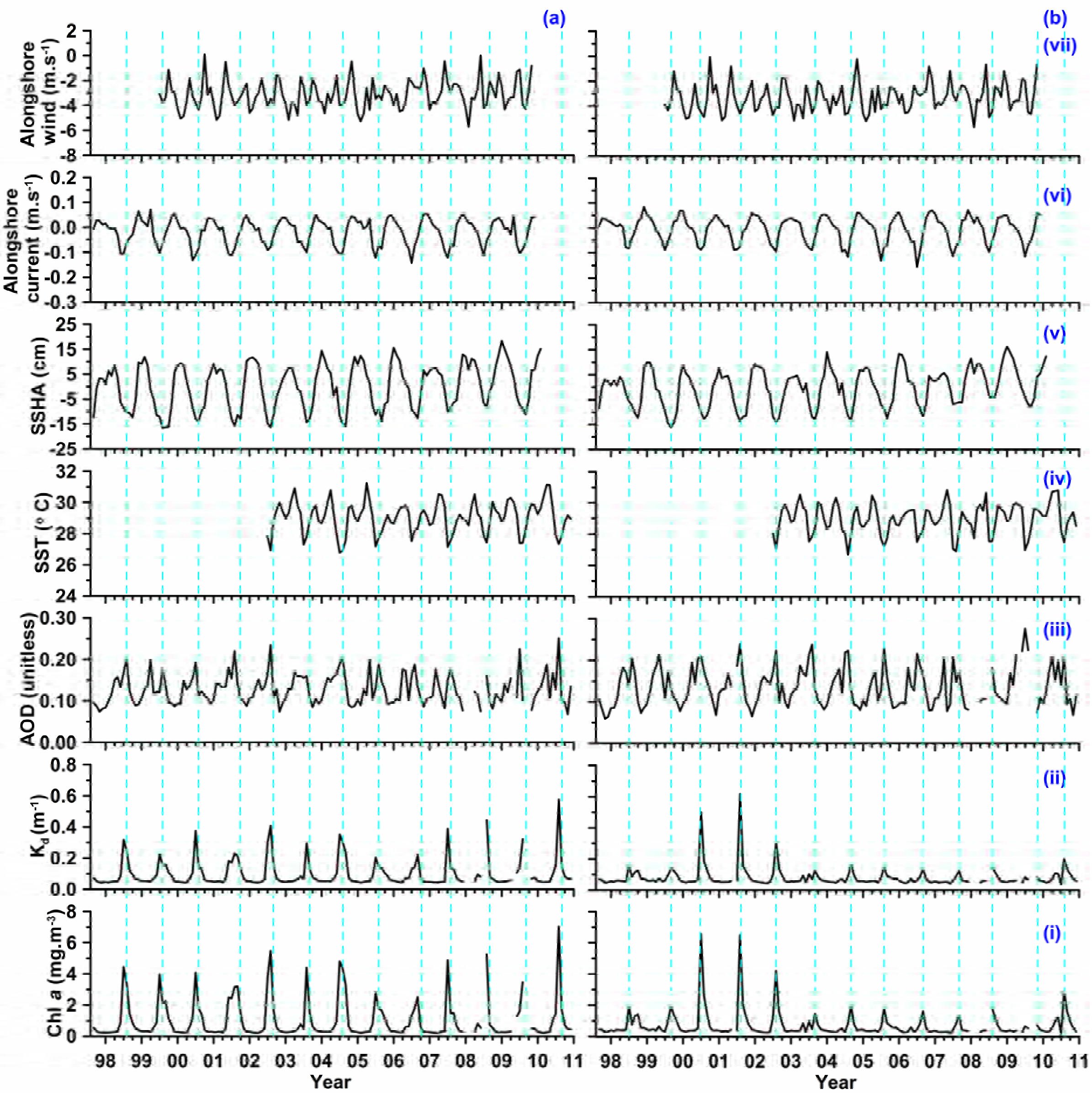

Figure 4.2. Temporal variability in (i) Chl *a*, (ii) K_d, (iii) AOD, (iv) SST, (v) SSH, (vi) surface current and (vii) surface wind of (a) Zone 1 and (b) Zone 2. The dotted vertical lines denote peak values of Chl *a*. The gap indicates non-availability of data.

Table 4.2. Months during which maxima / minima occurred in Chl *a* , K_d, AOD, SST, SSHA, current and winds in Zone 1

Year	Maximum			Minimum SST	Lowest SSHA	Maximum	
	Chl *a*	K_d	AOD			southerly current	southward wind
1998	Jul	Jul	Aug	-	Oct	Jul	-
1999	Jul	Jul	Apr	-	Oct	Jul	Aug
2000	Jul	Jul	Jul	-	Aug	Jun	Feb
2001	Aug, Sep	Aug	Aug	-	Aug	Jul	Feb
2002	Aug	Aug	Aug	Aug	Aug	Jul	Jan
2003	Aug	Aug	Apr	Jul	Aug	Aug	Feb
2004	Jul	Jul	Aug	Jul	Sep	Jul	Feb
2005	Jul	Jul	May	Jul	Sep	Jul	Feb
2006	Sep	Sep	Aug	Jul	Sep	Jul	Mar
2007	Jul	Jul	Mar, Aug	Jul	Jul	Jul	Jan
2008	Aug	Aug	Aug	Aug	Aug	Jul	Feb
2009	Aug	Aug	Jul	Aug	Sep	Jul	Feb, Sep
2010	Aug	Aug	Aug	Aug	-	-	-

Table 4.3. Months during which maxima / minima occurred in Chl *a* , K_d, AOD, SST, SSHA, current and winds in Zone 2

Year	Maximum			Minimum SST	Lowest SSHA	Maximum	
	Chl *a*	K_d	AOD			southerly current	southward wind
1998	Jul	Jul	Aug	-	Oct	Jul	-
1999	Sep	Sep	May	-	Sep	Jul	Aug
2000	Jul	Jul	Jul	-	Aug	Jul	Feb
2001	Aug	Aug	Aug	-	Aug	Jun	Feb
2002	Aug	Aug	Aug	Aug	Aug	Aug	Jul
2003	Sep	Sep	Aug	Jul	Sep	Aug	Feb
2004	Sep	Sep	Aug	Aug	Sep	Aug	Feb, Jul
2005	Aug	Aug	Aug	Aug	Sep	Jul	Feb
2006	Sep	Sep	Jul	Jul	Sep	Jul	Mar
2007	Sep	Sep	Jul	Aug	Jul	Jul	Jan
2008	Aug	Aug	Aug	Jul, Aug	Aug	Jul	Feb
2009	Jul	Jul	Jul	Jul	Sep	Jul	Sep
2010	Aug	Aug	Apr, Aug	Aug	-	-	-

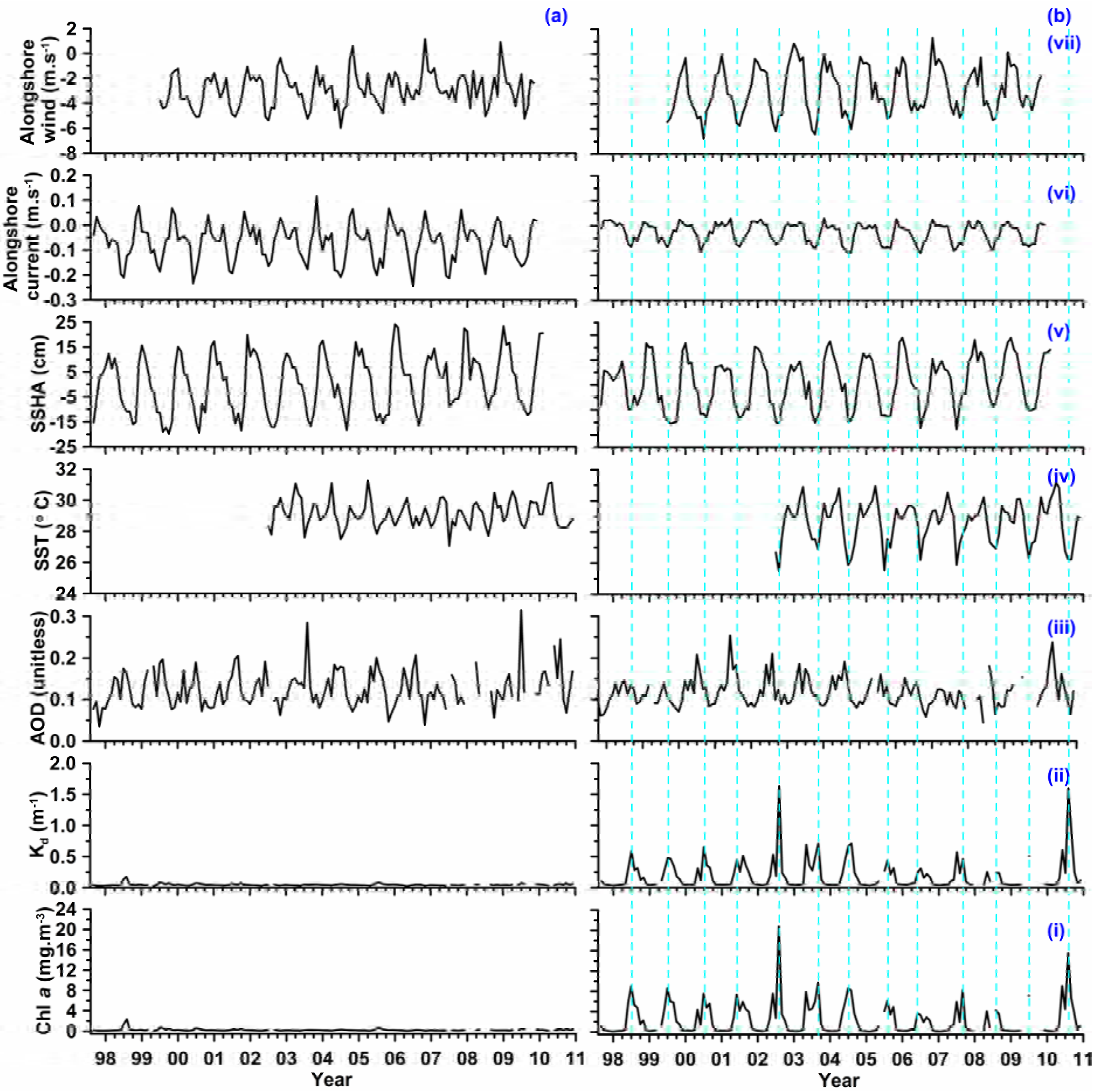

Figure 4.3. Temporal variability in (i) Chl *a*,(ii) K_d, (iii) AOD, (iv) SST, (v) SSH, (vi) surface current and (vii) surface wind of (a) Grid 1b and (b) Grid 1a. The dotted vertical lines denote peak values of Chl *a*. The gap indicates non-availability of data.

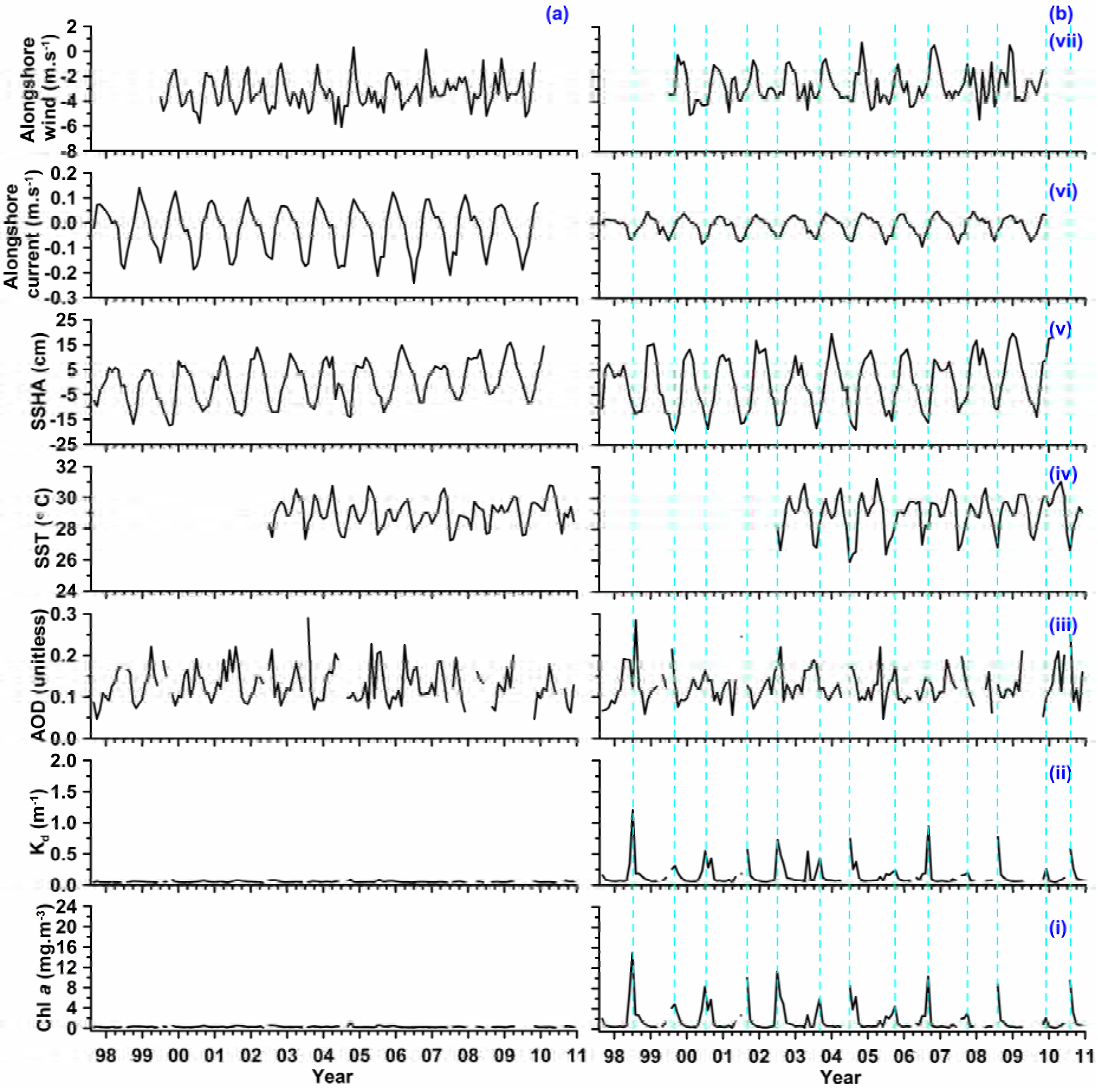

Figure 4.4. Temporal variability in (i) Chl *a*, (ii) K$_d$, (iii) AOD, (iv) SST, (v) SSH, (vi) surface current and (vii) surface wind of (a) Grid 2b and (b) Grid 2a. The dotted vertical lines denote peak values of Chl *a*. The gap indicates non-availability of data.

Table 4.4. Months during which maxima / minima occurred in Chl *a* , K_d, AOD, SST, SSHA, current and winds in Grid 1a

Year	Maximum			Minimum SST	Lowest SSHA	Maximum	
	Chl *a*	K_d	AOD			southerly current	southward wind
1998	Jul	Jul	Jul	-	Jul	Jul	-
1999	Jul	Jul, Aug	Aug	-	Aug	Jul	Jul
2000	Jul	Jul	Jul	-	Aug	Jun	Jul
2001	Jun	Aug	Jun	-	Jul	Jul	Jun
2002	Aug	Aug	Aug	Aug	Aug	Jul	Jul
2003	Sep	May, Sep	May	Sep	Aug	Aug	Aug
2004	Jul	Aug	Aug	Jul	Jul	Jul	Aug
2005	Aug	Aug	Aug	Jul	Sep	Jul	Sep
2006	Jun	Jul	Apr	Jul	Jul	Jul	Jun
2007	Sep	Jul	Mar, Apr	Jul	Jul	Jun	Aug
2008	Aug	May	Aug	Aug	Jul	Jul	Jul
2009	Jul	Jul	Jul	Jul	Jul	Jul	May
2010	Aug	Aug	May	Aug, Sep	-	-	-

Table 4.5. Months during which maxima / minima occurred in Chl *a*, K_d, AOD, SST, SSHA, current and winds in Grid 2a

Year	Maximum			Minimum SST	Lowest SSHA	Maximum	
	Chl *a*	K_d	AOD			southerly current	southward wind
1998	Jul	Jul	Aug	-	Aug	Jul	-
1999	Sep	Sep	Aug	-	Sep	Jul	Aug
2000	Jul	Jul	Jul	-	Aug	Jun	Aug
2001	Sep	Sep	Jul	-	Jul, Aug	Jun, Jul	Mar
2002	Jul	Jul	Aug	Aug	Jul	Jul	Mar
2003	Sep	May	Jul	Aug	Aug	Aug	May
2004	Jul	Jul	Jul	Jul	Sep	Jul, Aug	Aug
2005	Oct	Oct	May	Jul	Sep	Jul	Feb
2006	Sep	Sep	Aug	Jul	Sep	Jul	Mar
2007	Oct	Oct	Aug	Jul	Jul	Jul	May
2008	Aug	Aug	May	Aug	Aug	Jul	Feb
2009	-	-	Apr	Aug	Sep	Jul	Feb
2010	Aug	Aug	Aug	Aug	-	-	-

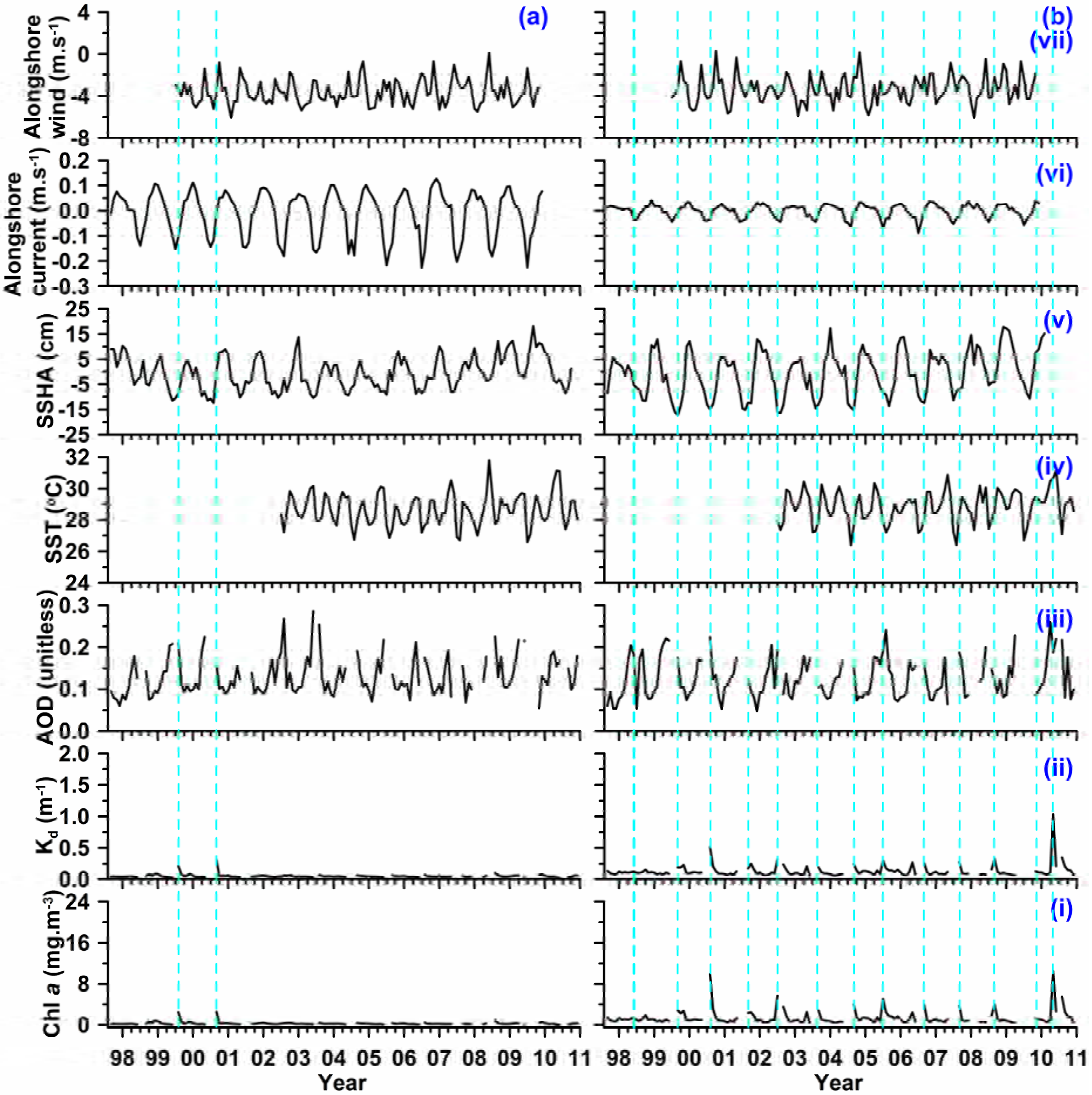

Figure 4.5. Temporal variability in (i) Chl *a*,(ii) K_d, (iii) AOD, (iv) SST, (v) SSH, (vi) surface current and (vii) surface wind of (a) Grid 3b and (b) Grid 3a. The dotted vertical lines denote peak values of Chl *a*. The gap indicates non-availability of data.

Table 4.6. Months during which maxima / minima occurred in Chl *a*, K_d, AOD, SST, SSHA, current and winds in Grid 3a

Year	Maximum			Minimum SST	Lowest SSHA	Maximum	
	Chl *a*	K_d	AOD			southerly current	southward wind
1998	Oct	Oct	May	-	Sep, Oct	Jun, Jul	-
1999	Sep	Nov	May	-	Sep	Jul	Jul
2000	Aug	Aug	Aug	-	Aug	Jun, Jul	Feb
2001	Oct	Oct	May	-	Jul, Aug	Jun	Feb
2002	Jul	Jul	May	Aug	Jul, Aug	Jul, Aug	Feb
2003	Sep	May	Apr	Jul	Aug	Jul, Aug	Feb
2004	Sep	Sep	May	Aug	Sep	Aug	Feb
2005	Jul	Jul	Aug	Aug	Sep	Jul	Feb
2006	Sep	May	Apr	Jul	Sep	Jul	Apr
2007	Sep	Sep	Sep	Aug	Jul	Jul	Jan
2008	Sep	Sep	Jun	Feb, Jul	Jul	Jul	Feb
2009	-	-	Apr	Jul	Sep	Jul	Feb
2010	May	May	Apr	Aug	-	-	-

4.2 Anomalies on ocean colour parameters and their response to climatic oscillations

To understand the inter-annual variability, monthly anomalies of Chl *a*, K_d and AOD during September 1997 – December 2010 were generated for all the selected areas. After an initial analysis, a threshold values of $\pm$ 1.0 mg.m^{-3} and $\pm$ 0.08 m^{-1} was fixed to demarcate positive and negative anomalies of Chl *a* and K_d in this study. The threshold value on AOD was fixed as 0.03 following Shalin and Sanilkumar (2013). Anomalies in Grid 1 – 3 were not included.

4.2.1 Anomalies on ocean colour parameters

Significant positive anomalies of Chl *a* / K_d (> 1.0 mg.m^{-3} / 0.08 m^{-1}) were observed during August 2002, July 2007 and August 2010, whereas negative anomalies (< -1.0 mg.m^{-3} / -0.08 m^{-1}) were observed during July 2001, 2003 and 2006, August 2006 and 2007 (Figure 4.7 and Table 4.7) in the Area 1.

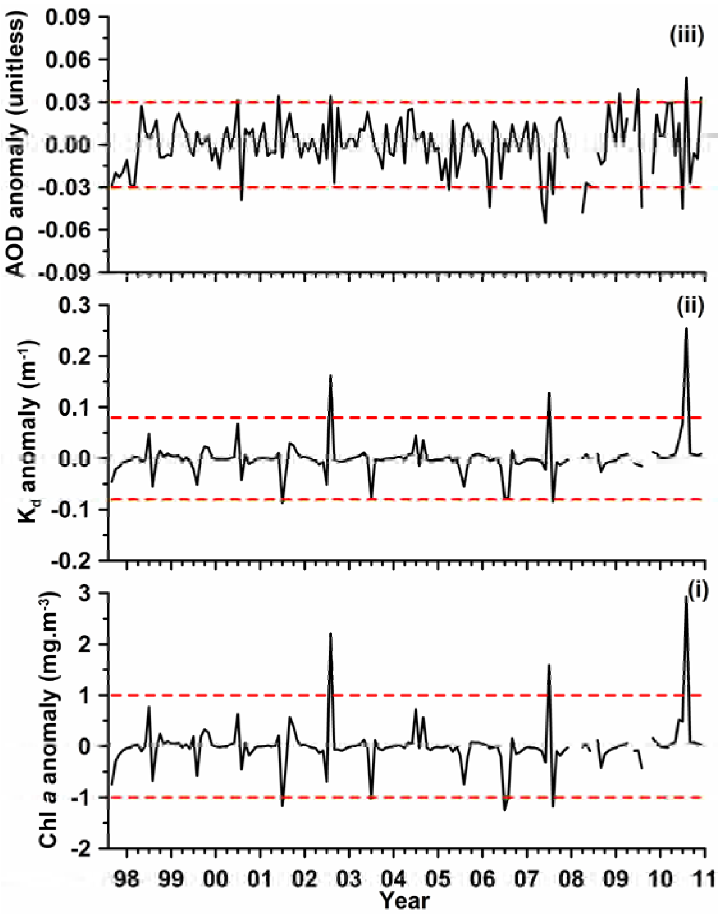

Figure 4.6. Anomalies on (i) Chl *a*, (ii) K$_d$ and (iii) AOD for Area 1 during September 1997 – December 2010. Red dotted lines represent threshold line to demarcate positive and negative anomaly.

AOD showed positive anomalies during June 2001, August 2002, February 2009, July 2009, August 2010 and December 2010 and negative during August 2000, March 2006, June 2007, April 2008, August 2009 and July 2010. The anomalies observed during 2008 – 2010 had both extreme positive and negative values.

Table 4.7. Significant Chl *a* anomalies along with the corresponding K_d and AOD for Area 1. The corresponding rain rate is also listed.

No	month	year	Chl *a* anomaly (mg.m^{-3})	K_d anomaly (m^{-1})	AOD anomaly (unitless)	Rain rate (mm.hr^{-1})
1	7	2001	-1.2	-0.09	-0.01	0.41
2	7	2003	-1.0	-0.08	0.01	0.53
3	7	2006	-1.2	-0.08	0.00	0.14
4	7	2007	1.6	0.13	0.00	0.55
5	8	2002	2.2	0.16	0.03	0.30
6	8	2006	-1.0	-0.08	0.00	0.21
7	8	2007	-1.2	-0.09	-0.04	0.38
8	8	2010	2.9	0.25	0.05	0.65

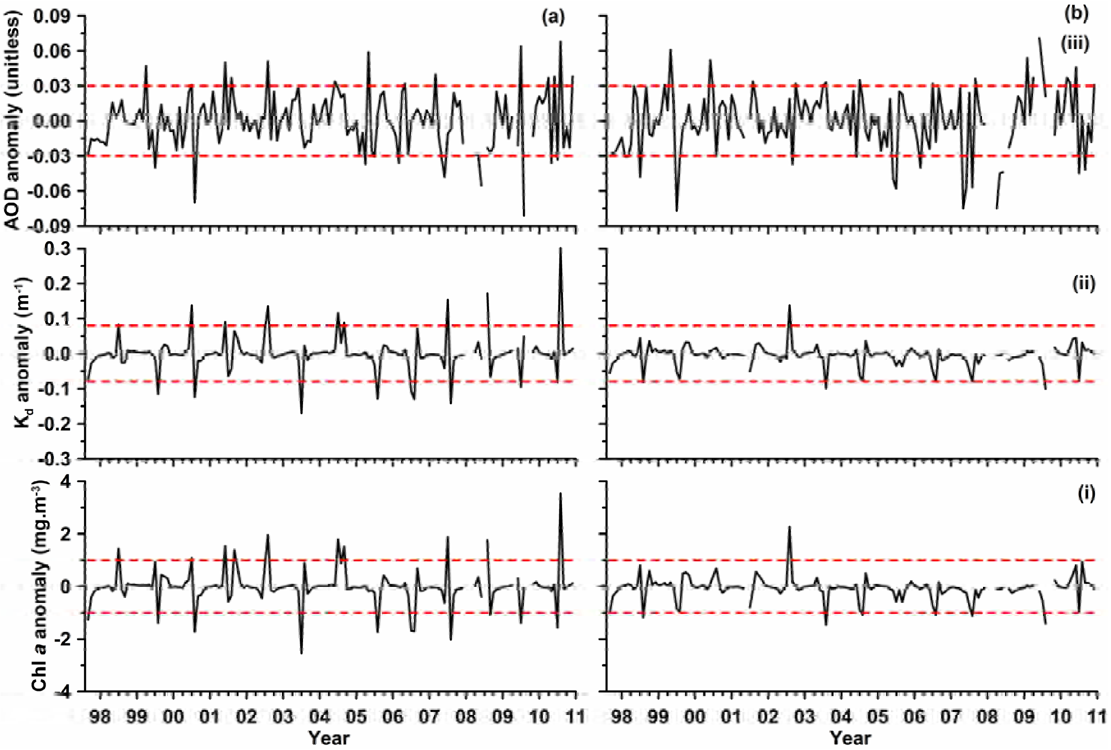

Figure 4.7. Anomalies on (i) Chl *a*, (ii) K_d and (iii) AOD in (a) Zone 1 and (b) Zone 2 during September 1997 – December 2010. Red dotted lines represent threshold line to demarcate positive and negative anomaly.

In general, Chl *a* / K_d anomaly in Zone 1 and 2 exceeded the threshold values during June – October (Figure 4.7). In Zone 2, Chl *a* / K_d showed anomalies only during September 1997, August 2006 and 2008. However, in Zone 1, Chl *a* / K_d anomaly crossed the threshold value every year in one or more months between July – September. The most significant positive Chl *a* anomalies in Zone 1 ($\geq$ 1.8 mg.m^{-3}) occurred during August 2002, July 2004, August 2008 and August 2010 and negative ($\leq$ -1.8 mg.m^{-3}) during July 2003 and August 2007.

Table 4.8. Significant Chl *a* anomalies along with the corresponding K_d and AOD in Zone 1

No	month	year	Chl *a* anomaly (mg.m^{-3})	K_d anomaly (m^{-1})	AOD anomaly (unitless)
1	7	2003	-2.5	-0.17	-0.01
2	7	2004	1.8	0.12	0.03
3	8	2002	2.0	0.14	0.05
4	8	2007	-2.0	-0.14	-0.01
5	8	2008	1.8	0.17	-0.02
6	8	2010	3.6	0.30	0.07

Table 4.9. Significant Chl *a* anomalies along with the corresponding K_d and AOD in Zone 2

No	month	year	Chl *a* anomaly (mg.m^{-3})	K_d anomaly (m^{-1})	AOD anomaly (unitless)
1	9	1997	-1.0	-0.05	-0.03
2	8	2006	-1.1	-0.08	-0.02
3	8	2007	-1.1	-0.08	-0.06

4.2.2 Indications of climatic oscillations in the anomalies of ocean colour parameters

El Nino/La Nina, popularly known as ENSO (El Niño–Southern Oscillation), is a major independent atmospheric mode originating from the Pacific Ocean, which affects the global climate (Ashok et al., 2001; Trenberth, 1997). The strength of this effect expressed in terms of Nino index. In the present work, the Nino index is calculated as the 3 month running mean of Sea Surface Temperature anomalies in the Nino 3.4 region (5° N to 5° S; 120° W to 170° W), provided by NOAA (www.nws.noaa.gov).

Saji et al. (1999) discovered an oscillating dipole mode, similar to ENSO originating from the tropical Indian Ocean and named it as the Indian Ocean Dipole (IOD). The intensity of the IOD is represented in terms of Dipole mode index (DMI), which is the difference in SST anomalies between the western tropical Indian Ocean (WTIO) (50° E to 70° E and 10° S to 10° N) and the southeastern tropical Indian Ocean (SETIO) (90° E to 110° E and 10° S to 0° N). Moreover, positive or negative values of DMI indicate whether the event during a specific year is positive IOD (PIOD) or negative IOD (NIOD). This coupled ocean - atmosphere phenomenon exerts a major impact on the climatic conditions over all the countries surrounding the Indian Ocean (Ashok et al. 2004; Saji and Yamagata 2003).

In general, ENSO / IOD significantly influence the thermocline, SST and winds, which eventually determine the intensity of upwelling in an area. The thickness of the thermocline determines the amount of nutrient supply to the mixed layer. A deep thermocline reduces the mixing rates and hence, the productivity. Similarly, weak winds reduce the productivity as vertical mixing is restricted. Moreover, warm SST lowers the dissolution of carbon dioxide in sea water, which again reduces the primary productivity (Sarma et al., 1996; Sarma et al., 2000; Weiss, 1974). Thus, weak winds, deep thermocline and warm SST during a PIOD event suppress the entrainment of nutrients into the mixed layer off the southwest coast of India. As a result, Chl *a* biomass during a PIOD event is lowered, whereas an NIOD event can enhance the Chl *a* concentration (Sarma, 2006). Thus, La Nina / El Nino events induces a typical ocean – atmosphere conditions similar to the NIOD / PIOD event in the eastern Indian Ocean. Jayaram (2011) analysed Chl *a* anomalies off the southwest coast of India for the years 1997, 1998, 2004 and 2006 respectively representing El Nino, La Nina, PIOD and NIOD modes.

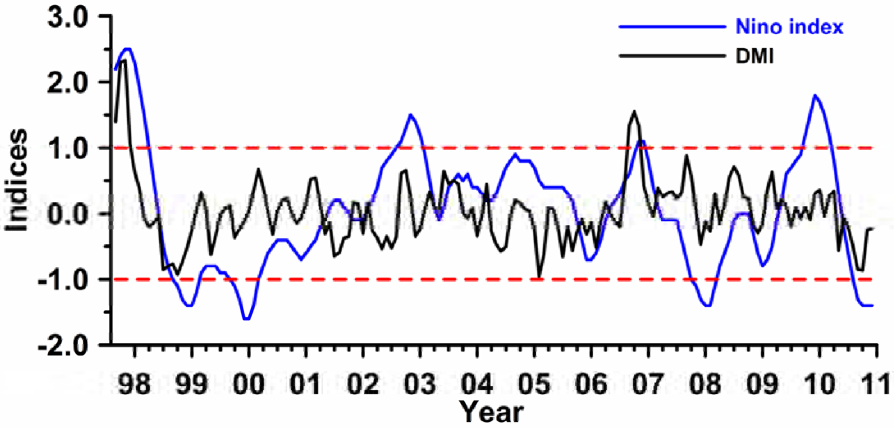

Figure 4.8. DMI and Nino indices during September 1997 – December 2010

Shalin and Sanilkumar (2013) observed a good response of ENSO / IOD on AOD over the south-eastern Tropical Indian Ocean. They attributed the changes in AOD to the incoming aerosols from Australia and Southeast Asia during El Nino, PIOD and concurrent modes of El Nino and PIOD. During the periods of La Nina, concurrent modes of La Nina and NIOD, AOD values came down due to heavy rain.

During the present study, since there were wide variations in the ENSO / IOD intensities (Figure 4.8), the responses of these modes on Chl *a* / K_d / AOD are examined in detail.

4.2.3 Results

a. Area 1

The results showed that positive Chl *a* anomaly (+ 2.9 $mg.m^{-3}$) during August 2010 coincided with the modes of La Nina / NIOD (Table 4.10). Similarly, the low values of Chl *a* / K_d (-1.0 $mg.m^{-3}$) during August 2006 co-occurred with the El Nino / PIOD event. This observation is consistent with Sarma (2006), who found that NIOD / PIOD events can enlarge / reduce the mixed layer depth which subsequently increase / decrease the Chl *a* biomass. Thus, positive anomaly of Chl *a* / K_d during a concurrent La Nina / NIOD event and negative anomaly during an El Nino / PIOD event, indicated the Chl *a* / K_d were influenced by the concurrent ENSO / IOD modes. In addition, a negative Chl *a* / K_d anomaly during July 2001 coincided with an NIOD while a high Chl *a* / K_d during August 2002 coincided with an El Nino event. Thus, the lone NIOD mode induced a negative Chl *a* anomaly.

The positive AOD anomalies during August 2002 and April 2010 and a negative anomaly during March 1998 coincided with El Nino events. Similarly, La Nina event coincided with significant negative anomaly of April 2008 and positive anomalies during February 2009 and December 2010 (Table 4. 11). Therefore, the influence of ENSO was not evident from the above observations. Similarly, positive anomaly during August 2010 coincided with concurrent La Nina / NIOD modes, implied the response of ENSO / IOD on AOD was not evident in Area 1.

b. Zone 1 and 2

In Zone 1, the positive anomalies of Chl *a* / K_d were found in July 2004 and August 2010, which coincided with the concurrent events of La Nina / NIOD and El

Nino / NIOD respectively (Table 4.12). This observation suggests that there was a possibility of co-occurring NIOD with El Nino or La Nina and led to enhance Chl *a* production. However, the negative Chl *a* anomaly of July 2003 and the positive anomaly of August 2008 were found to coincide with PIOD. Further, a positive anomaly of August 2002 matched with an El Nino event. Therefore, the influence of PIOD and El Nino events on Chl *a* production was not clear from these observations, though there might be a possible co-occurrence of NIOD with one of the phases of ENSO initiating the upwelling process, which leads to an increased production of *Chl a* in this zone.

Table 4.10. Nino and DMI indices during significant Chl *a* and K_d anomalies ($\underline{+}$1.0 mg.m^{-3}/ 0.08 m^{-1}) for Area 1

No	month	Year	Chl *a* anomaly	K_d anomaly	Nino index	DMI	Event
1	7	2001	-1.2	-0.09	0.2	-0.6	NIOD
2	8	2002	2.2	0.16	1.0	-0.4	El Nino
3	7	2006	-1.2	-0.08	0.3	-0.2	normal
4	8	2006	-1.0	-0.08	0.5	0.5	El Nino/PIOD
5	8	2010	2.9	0.25	-1.0	-0.5	La Nina/NIOD

Table 4.11. AOD anomalies ($\underline{+}$ 0.03) over Area 1 during significant ENSO / IOD events

No	Month	Year	AOD anomaly	Nino index	DMI	Events
1	3	1998	-0.03	1.5	-0.1	El Nino
2	8	2002	0.03	1.0	-0.4	El Nino
3	4	2008	-0.05	-0.8	-0.1	La Nina
4	2	2009	0.04	-0.7	0.4	La Nina
5	4	2010	0.03	0.8	0.3	El Nino
6	8	2010	0.05	-1.0	-0.5	La Nina / NIOD
7	12	2010	0.03	-1.4	-0.2	La Nina

In Zone 2, a negative anomaly on Chl *a* / K_d during September 1997 and August 2006 coincided with the concurrent modes of El Nino / PIOD (Table 4.13).

But, the strengths of El Nino and PIOD were not found to be proportional to the anomalies.

Table 4.12. Nino and DMI indices during significant Chl *a* anomalies ($\geq$ 1.8 mg.m^{-3}) for Zone 1

No	Year	month	Chl *a* anomaly	K_d anomaly	Nino index	DMI	Event
1	8	2002	2.0	0.14	1.0	-0.4	El Nino
2	7	2003	-2.5	-0.17	0.4	0.5	PIOD
3	7	2004	1.8	0.12	0.7	-0.5	El Nino / NIOD
4	8	2007	-2.0	-0.14	-0.4	0.3	normal
5	8	2008	1.8	0.17	0.0	0.6	PIOD
6	8	2010	3.6	0.30	-1.0	-0.5	NIOD / La Nina

Table 4.13. Nino and DMI indices during significant Chl *a* anomalies ($\geq$ 1.8 mg.m^{-3}) for Zone 2

No	month	year	Chl *a* anomaly	K_d anomaly	Nino index	DMI	Event
1	9	1997	-1.0	-0.05	2.2	1.4	El Nino/PIOD
2	8	2006	-1.1	-0.08	0.5	0.5	El Nino/PIOD
3	8	2007	-1.1	-0.08	-0.4	0.3	normal

The positive AOD anomaly of June 2004, July 2009, April 2010 and the negative AOD anomaly of August 2009 in Zone 1 coincided with El Nino events (Table 4.14). In addition, positive anomaly of August 2001 and June 2004 and negative anomaly of July 2005 and May 2010 coincided with NIOD. From the above results, the effect of El Nino and NIOD on the abundance of AOD is not clear. The positive anomaly of August and December 2010 corresponded to concurrent La Nina / NIOD and La Nina respectively. However, heavy rainfall during La Nina washes out aerosol (Bhatla et al., 2006) and low AOD is expected, which is contrary to the present observation. Moreover, the positive anomaly during June 2000, September 2007 and

February 2009 and negative anomaly during April 2008, May 2008, and September 2010 coincided with La Nina mode in Zone 2 (Table 4.15). Therefore, the influence of ENSO / IOD was not evident on AOD over Zone 1 and Zone 2.

Table 4.14. AOD anomalies (± 0.03) over Zone 1 during significant ENSO / IOD events

No	Month	year	AOD anomaly	Nino index	DMI	Events
1	8	2001	0.04	0.2	-0.6	NIOD
2	6	2003	0.03	0.1	0.6	PIOD
3	6	2004	0.03	0.5	-0.6	El Nino / NIOD
4	7	2005	-0.03	0.4	-0.7	NIOD
5	7	2009	0.06	0.7	-0.2	El Nino
6	8	2009	-0.08	0.8	0.1	El Nino
7	4	2010	0.04	0.8	0.3	El Nino
8	5	2010	-0.04	0.3	-0.6	NIOD
9	8	2010	0.07	-1.0	-0.5	La Nina / NIOD
10	12	2010	0.04	-1.4	-0.2	La Nina

Table 4.15. AOD anomalies (± 0.03) over Zone 2 during significant ENSO / IOD events

No	Month	year	AOD anomaly	Nino index	DMI	Events
1	6	2000	0.05	-0.5	-0.3	La Nina
2	9	2002	-0.04	1.1	0.6	El Nino / PIOD
3	9	2007	0.04	-0.7	0.9	La Nina / PIOD
4	4	2008	-0.08	-0.8	-0.1	La Nina
5	5	2008	-0.05	-0.6	0.1	La Nina
6	2	2009	0.05	-0.7	0.4	La Nina
7	3	2010	0.04	1.2	0.3	El Nino
8	9	2010	-0.04	-1.3	-0.9	La Nina / NIOD

4.2.4 Discussion

An underlying trend of the influence of ENSO / IOD was observed on monthly anomalies of Chl *a* and K_d during the southwest monsoon especially during July -

September. Hence, a detailed analysis was carried out. Values of Chl *a* during July – September were averaged and compared with the climatic events to know the over all influence of them. K_d has not been separately analysed, as it closely followed the trend of Chl *a*. Similarly, AOD has also not been presented here due to the reason that it had not shown any significant correlation with the climatic events. Chl *a* anomaly showed significant positive and negative values (Figure 4. 9). To demarcate the prominent anomalies a threshold of $\pm$ 0.5 $mg.m^{-3}$ was fixed. Positive ($\geq$ + 0.5 $mg.m^{-3}$) values were observed during the year 2002, 2004 and 2010 and negative ($\leq$ - 0.5 $mg.m^{-3}$) during 1997 and 2006. The negative values of Chl *a* coincided with concurrent modes of El Nino and PIOD. Moreover, DMI and Nino indices were stronger during 1997 (2.2 / 1.4) compared to that during 2006 (~0.5 / 0.5) and the high positive anomaly (-1.3 $mg.m^{-3}$) during 1997 and low anomaly during 2006 (-0.6 $mg.m^{-3}$), indicate strong influence of El Nino / PIOD on Chl *a* reduction in the area. Similarly, concurrent La Nina / NIOD (-1.0 / -0.5) coincided with high positive anomaly (> 1.0 $mg.m^{-3}$). It is to be noted that the above observations are in concurrence with the earlier observations of weak upwelling during El Nino events and strong upwelling during La Nina events (Jayaram, 2011; Krishna, 2008). Contrary to the above, positive anomaly was observed during 2002 and 2004, when El Nino event occurred. Therefore, the DMI event during those years was critically examined (Figure 4.8). DMI was found negative during May – July during the above years, indicating upwelling favourable condition. Therefore, the positive anomaly during 2002 and 2004 was attributed to NIOD event. Thus, the present study revealed a strong response to the climatic events viz. ENSO and IOD in regulating Chl *a* values in the study area.

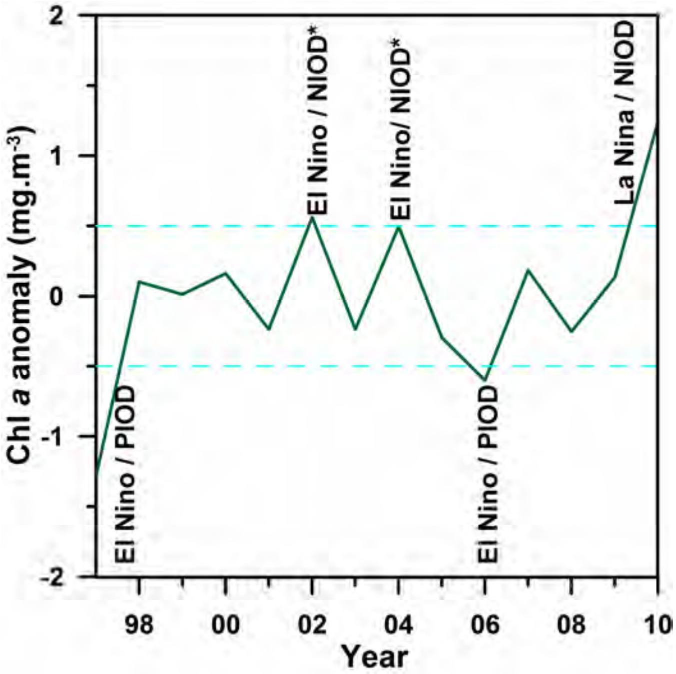

Figure 4.9. Anomalies on Chl *a* averaged in Area 1for the months of July – September during the period September 1997 – December 2010 and the corresponding climatic oscillations

4.3 Tracking aerosol trajectory using HYSPLIT model

Co-occurrences of high / low AOD with corresponding high / low values of Chl *a* / K_d during anomalous years were observed in section 4.1.3 (Table 4.6-8). In order to evaluate the influence of aerosols during these years over Area 1, HYSPLIT (Hybrid Single-Particle Lagrangian Integrated Trajectory) model was used (Draxler and Hess, 1998). Though, the experiment was carried out over the subareas also, they have not presented. To run the model, two atmospheric pressure levels viz. 700 hPa and 1000 hPa were selected as these levels are found suitable to track the aerosol source during the southwest monsoon period (Li and Ramanathan, 2002). The model was run to obtain the weekly trajectory of the aerosols so that four trajectories altogether provided the monthly picture. The weekly trajectories were selected due to the reason that the settling period of aerosols is nearly a week (Ginoux et al., 2001). Since, rainfall also determines the aerosol distribution over an area; it is prudent to select the data points with similar rainfall rate. Accordingly, only the periods matching above criteria were selected for modeling. Trajectories modeled by HYSPLIT are presented for each atmospheric level along with averaged winds during the month, to visualize the influence of winds on aerosol trajectory.

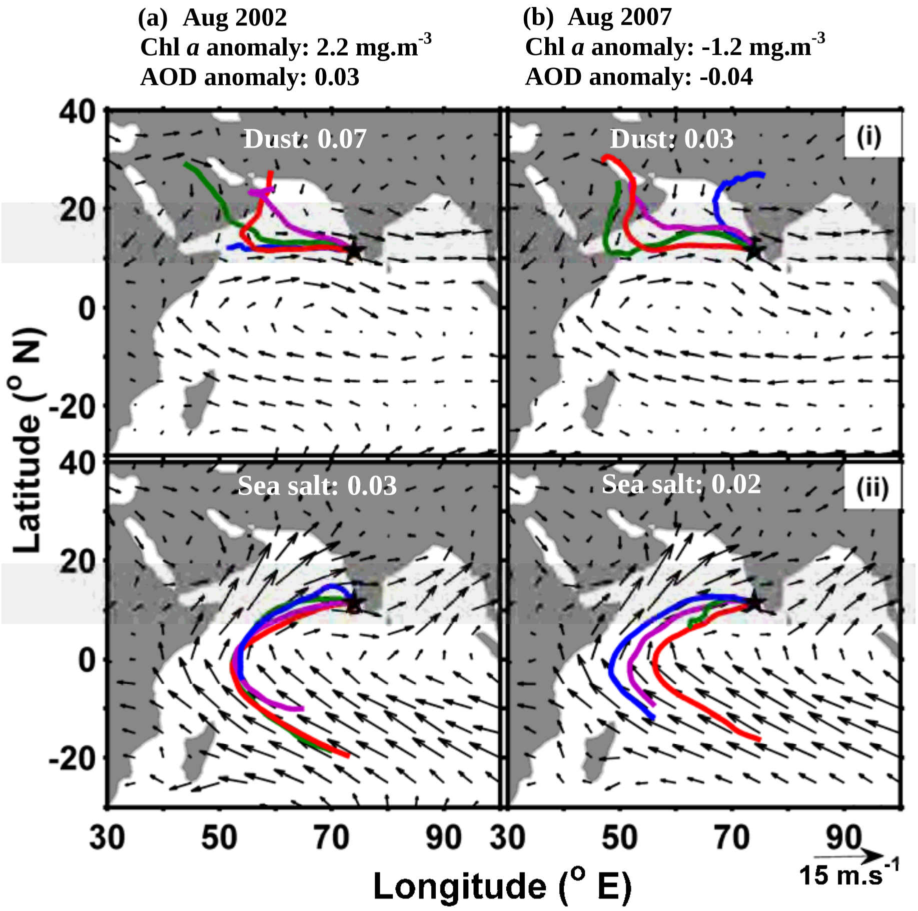

Figure 4.10. HYSPLIT aerosol trajectory for four weeks in a month from the centre point of area 1 at (i) 700 hPa and (ii) 1000 hPa during (a) August 2002 and (b) August 2007. Red, magenta, green and blue lines represent aerosol trajectories during 1st-8th, 8th – 15th, 15th-22nd and 22nd-29th of the selected month respectively.

August 2002 / August 2007 representing positive / negative anomalies were chosen to trace aerosol source over Area 1 (Table 4. 6). The trajectories at level 1 (1000 hPa) during both the periods appeared to be originated from the oceanic region and did not exhibit significant variability (Figure 4.10). It is to be mentioned here that the level 1 represents the atmosphere overlying just above the sea surface, where the component of aerosol at this level is sea salt. Moreover, salt production directly depends on wind speed (Moorthy et al., 1997) or in other words long aerosol trajectory.

At level 2 (700 hPa), all the four trajectories were found extended from Saudi Arabia and Africa during August 2002, when AOD anomaly was positive. However, during the period of negative anomaly (i.e., August 2007), one of the aerosol trajectories was originating from the Indian sub-continent. In this conjunction, it is to be noted that during the southwest monsoon period very high aerosol content exists over Saudi Arabia and northern Africa (Hsu et al., 2012; Li and Ramanathan, 2002). Strong westerly winds observed at level 2 passing through the above regions would have transported high aerosol content over Area 1 during the positively anomalous period. Thus, the enhanced sea salt content as well as aerosol supply from Saudi Arabia and Northern Africa could be the cause of positive anomaly during August 2002.

In order to quantify the constituents of the aerosol content, the output of GOCART (Goddard Global Ozone Chemistry Aerosol Radiation and Transport) model provided by Giovanni site (http://gdata1.sci.gsfc.nasa.gov/) was extracted and used. GOCART is a global model which simulates major tropospheric optical depth of major aerosol components viz. dust, sulphate, black carbon, organic carbon and sea salt (Chin et al., 2000; Chin et al., 2002; Ginoux et al., 2001; Ginoux and Torres, 2003). Among the components, sea salt and dust deserves special attention due to the following reasons. Sea salt is the main component at level 1 (Moorthy et al., 1997). Dust is an important component, as it contains iron content (Ginoux et al., 2001). Further, it is known that, the iron deposition from atmosphere is a source of nutrients in the sea surface, which influences primary productivity (Duce and Tinsdale, 1991; Eker-Develi et al., 2006; Fan et al., 2006; Jickells et al., 2005; Mahowald et al., 2005; Mahowald et al., 2009; Patra et al., 2006; Santos 2010; Sholkovitz et al., 2009; Wiggert and Murtugudde, 2007). Also, iron induced phytoplankton growth is reported in the equatorial Pacific Ocean (Behrenfeld et al., 1996; Fitzwater et al., 1996; Martin and Gordon, 1988), subarctic Pacific (Miller et al., 1991), north Atlantic Ocean (Moore et al., 2006; Santos, 2010), southern Ocean (Boyd et al., 2000), northwestern Arabian Sea (Takeda et al., 1995; Witter et al., 2000), Mediterranean Sea (Eker-Develi et al., 2006) and the coastal zone of California (Johnson et al., 2001), Peru (Hutchins et al., 2002), Oregon (Chase et al., 2002) and Gulf of Alaska (Martin et al., 1989). The above result suggests iron content also would have contributed to increase Chl *a* growth in Area 1.

The sea salt component from GOCART model showed only marginal differences on sea salt levels between August 2002 (0.03) and 2007 (0.02) (Figure 4.10). When the AOD anomaly was positive during August 2002, it is to be noted that all the trajectories were from Saudi Arabia and northern Africa, where aerosol is rich in iron content (Siefert, 1999). The above results prompt to speculate that iron content from the Arabia and Northern Africa has an important role in the growth of Chl *a* in Area 1.

4.4 Oscillatory modes – Empirical Mode Decomposition

It is understood that intra- and inter-annual variability as well as the influence of climatic oscillations exist in the study area and are reflected on the ocean colour parameters. In order to examine the oscillatory nature of that variability, EMD method was applied to Chl *a*, K_d and AOD. It is well established that most of the variabilities are non-linear in nature (Varotsos and Kirk-Davidoff, 2006). The EMD separates nonlinear oscillatory modes with their amplitude and frequency modulations from the time series distribution (Huang et al., 1998; McDonald et al., 2007). The method also provides the true representation of the trend embedded in the data. Continuous ocean colour observation is a pre-requisite for this analysis and hence, this section utilises SeaWiFS data up to December 2007. The EMD method was applied to Area 1, Zone 1, Zone 2 and Grid 1a based on the availability of continuous data.

4.4.1 Results

a. Area 1

Results of the EMD analysis on Chl *a*, K_d and AOD for Area 1 is presented in Figure 4.11. The time series signal is represented in the top panel, followed by one to four Intrinsic Mode Functions (IMF1, IMF2, IMF3 and IMF4) and residual in the bottom panel. IMF1 of Chl *a* indicated the existence of a rhythmic oscillation initially during 1998 – 2002, and then the signal was obscured with noise. The observed rhythmic oscillation during the above period had 4 crests and troughs, with an average periodicity of 1 year. The rhythmic oscillation for the IMF1 of K_d and AOD were not clear and appears to be superimposed with noises rather than signals. Such noises are common in IMF1 (McDonald et al., 2007). IMF2 of Chl *a* constituting 10 crests / troughs between January 1998 – December 2007, indicated oscillatory cycles having periodicity of one year. The amplitudes of this oscillatory cycle were low during 2001 and 2005 – 2006, which coincided with low Chl *a*. The oscillation IMF2 of K_d / AOD followed a pattern similar to that of Chl *a*. However, the general trend on K_d was disturbed during certain years viz. 1998 - 1999 and 2006 – 2007. The disturbed annual cycle of K_d during 1999 and 2006 coincided with low values of K_d. The existence of an annual cycle on Chl *a* / K_d / AOD had also been already brought out (section 4.1). IMF2 of AOD showed disturbed annual signal during the year 2002. Three oscillations were seen in IMF3 of Chl *a* during 1998 – 2003, but was disturbed after 2003. In general, IMF3 of K_d and AOD were sequenced at variable periodicities. K_d showed one year periodicity during 1998 and 2007, but during the rest of the period, the periodicity was around two years. Similarly, IMF3 of AOD showed one year periodicity during 2002 and nearly two year period during rest of the period. A four year oscillation was observed on IMF4 of Chl *a* during 2001 – 2004. IMF4 of K_d showed a nearly five year periodicity from 1998 to middle of 2003, after which, it shifted to a three year wave. However, the IMF4 of AOD showed around three year periodicity. The residual represents the absolute trend underlying in the entire datasets. An increasing trend on Chl *a* was observed up to 2002, followed by decreasing trend. K_d also showed an increasing trend up to 2002 and a decreasing trend afterwards, whereas a steady state was observed on AOD up to 2003, followed by a decreasing trend.

Thus, EMD analysis brought out the different oscillatory modes of Chl *a* / K_d / AOD. An annual cycle was common on the three parameters and various oscillations with periods ranging from one to five and half years were observed.

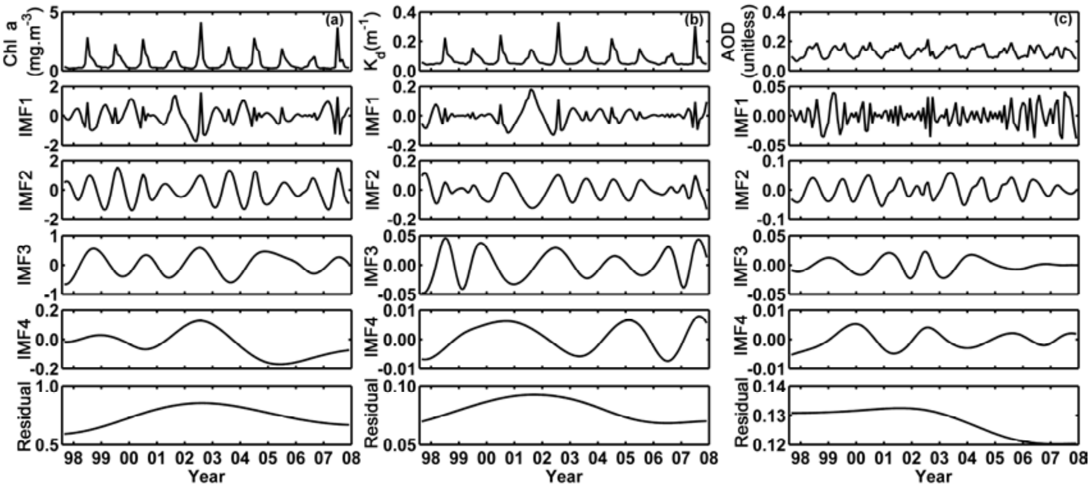

Figure 4.11. EMD on (a) Chl *a*, (b) K_d and (c) AOD in Area 1.

b. Zone 1 and 2

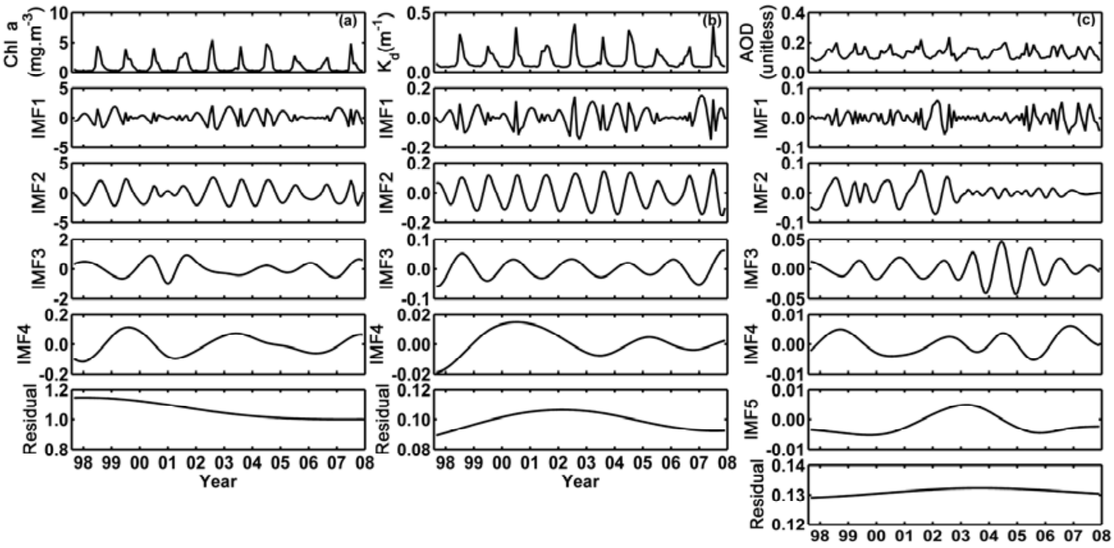

Figure 4.12. EMD on (a) Chl *a*, (b) K_d and (c) AOD in Zone 1.

EMD analysis on Chl *a* / K_d in Zone 1 brought out four IMF's and in case of AOD five IMF's (Figure 4.12). Rhythmic oscillation on IMF1 of Chl *a* / K_d / AOD was obscured, as obtained for Area 1. In general, IMF2 and IMF3 showed rhythmic oscillation. IMF2 of Chl *a* showed periodicity of one year. However, this trend was disturbed during 2000 – 2001. In case of K_d, annual oscillation prevailed on IMF2 throughout the study period. The crests and troughs of these oscillations co-occurred with maxima and minima values of K_d. Moreover, the low amplitude on IMF2 during 2005, co-occurred with the lowest value of K_d in the annual distribution. IMF2 of AOD showed high variation. Unlike IMF2 of Chl *a* / K_d, the annual oscillation on IMF2 of AOD was observed only during 1998, 2000 and 2002. The rhythmicity on IMF3 of Chl *a* was not clear, both in amplitude and period. A rhythmic oscillation was observed on IMF3 of K_d. The six troughs on IMF3 suggest a biennial oscillation. The periodicity of IMF3 of AOD varied between one / two year and amplitude between 0.02 – 0.05. In general, IMF4 of Chl *a* showed a three year oscillation during 1998 – 2001 and for the rest of the period oscillation was obscured. In the case of K_d, a five and a half year cycle was followed by three year cycle during 1998 – 2006. IMF4 of AOD exhibited varying periodicity with two – three year oscillations and IMF5 revealed an oscillatory mode with five year period. Residual on Chl *a* showed a decreasing trend. In the case of K_d, an increasing trend was observed up to 2001, and a decreasing trend afterwards. An increasing trend was observed on AOD up to 2003 and a decreasing trend after 2006.

IMF3 in Area 1 and the Zone 1 showed similar periodicities of 1-2 years. Unlike Area 1, the IMF5 of AOD over Zone 1 showed a five year oscillation.

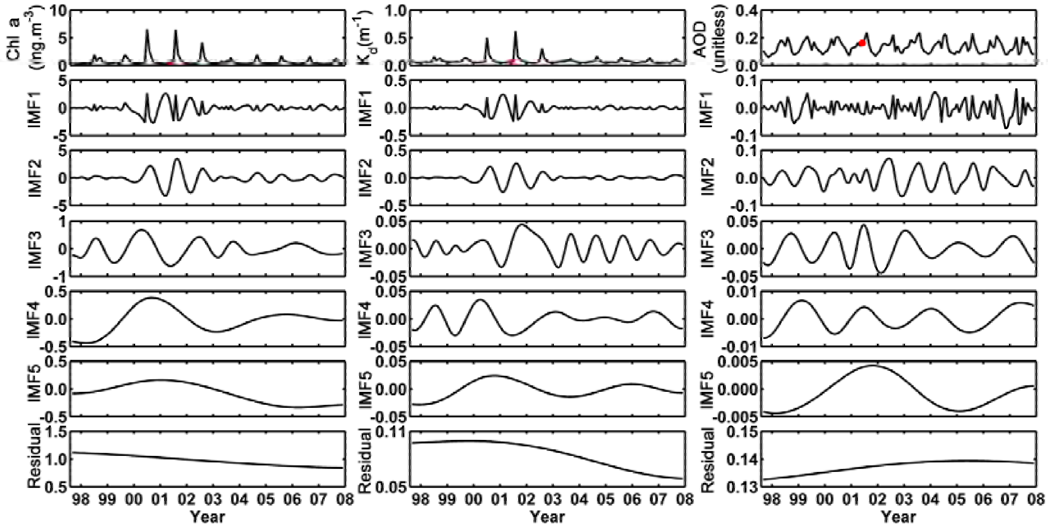

Figure 4.13. EMD on (a) Chl *a*, (b) K_d and (c) AOD in Zone 2. Red dot represents the interpolated point.

EMD analysis on Chl *a*, K_d and AOD in Zone 2 revealed five IMF's on each parameters (Figure 4.13). During the period 2000 – 2002, IMF1 and IMF 2 exhibited rhythmic oscillation and for rest of the period rhythmicity was not clear due to low amplitude waves. Similar to Chl *a*, IMF1 and IMF2 of K_d showed an oscillatory motion during 2000 - 2002. It is to be noted here that during the period 2000 – 2002, the peak value on the annual cycle of Chl *a* (> 3 $mg.m^{-3}$) / K_d (> 0.2 m^{-1}) were high compared to rest of the period. However, IMF1 of AOD did not show any prominent rhythmicity. IMF2 of AOD brought out an annual oscillation, which was disturbed during 2001. In general, IMF3 of Chl *a*, K_d and AOD varied between annual to biennial periodicities. IMF4 of Chl *a* during 1998 – 2002 revealed a six year oscillation. Periodicity and amplitude of IMF4 of K_d during the study period; showed nearly a biennial oscillation. In general, nearly two year periodic oscillation was observed on IMF4 of AOD. IMF5 of Chl *a* indicated a long period wave, however the periodicity of this oscillation was not clear. IMF5 of K_d and AOD showed five to seven year periodic oscillations. A decreasing trend was observed on Chl *a* in Zone 2. In the case of K_d, a steady state prevailed up to 2001 and a decreasing trend after 2002. However, AOD showed an increasing trend.

EMD in Zone 2 revealed six year oscillation in K_d and a seven year oscillation on AOD, which was not observed in Area 1 and Zone 1.

c. Grid 1a

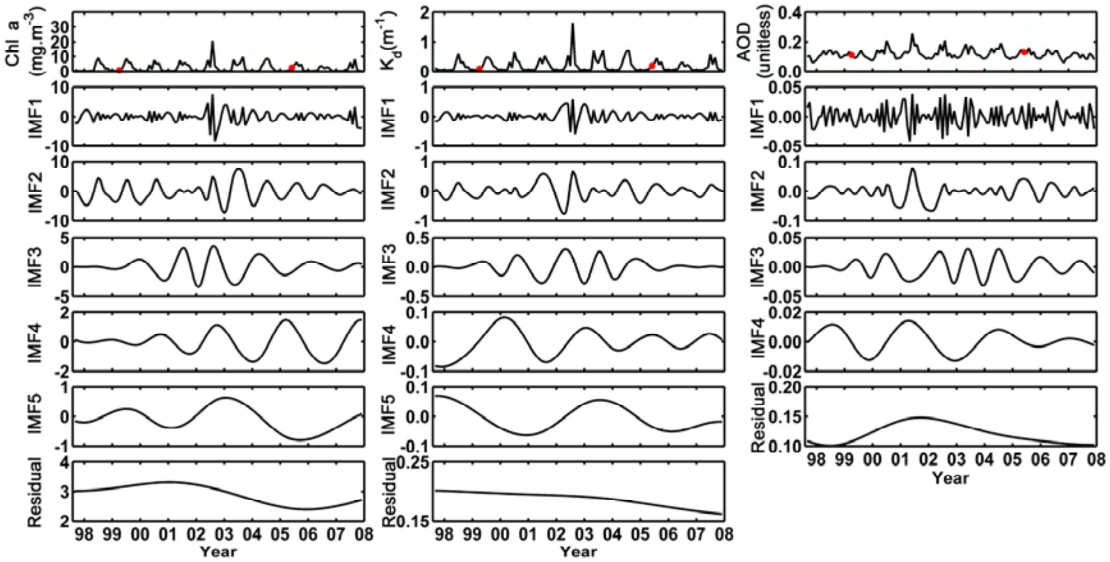

Figure 4.14. EMD on (a) Chl *a*, (b) K_d and (c) AOD in Grid 1a. Red dot represents the interpolated point.

EMD revealed five IMF's embedded on Chl *a* / K_d and four IMF's on AOD (Figure 4.14). The rhythmicity on IMF1 of Chl *a* / K_d / AOD was obscured, similar to that of the other areas. In general, IMF2 of Chl *a* indicated an annual oscillation. However, the annual signals were not clear on IMF2 of K_d. The amplitude and periodicity of IMF2 on AOD showed high variability; such that periodicities varied between semi-annual to annual. In general, during the period 2000 – 2006 oscillation varied between one to two years periodicity on IMF3 of Chl *a* / K_d / AOD. The IMF4 of Chl *a* showed varying periodicity and amplitude. However, two oscillations during

2002 – 2006 indicted a periodicity of nearly two years. Similarly, periodicity of IMF4 of K_d varied between two to three years. However, IMF4 of AOD indicated a rhythmic oscillation with three year period. The periodicity of oscillation on IMF5 varied between four to five years. A five year oscillation was observed on IMF5 of K_d. An increasing trend was observed on Chl *a* during 1997 - 2001 and 2006 – 2007 and in between these periods a decreasing trend prevailed. AOD followed an increasing trend during 1999 – 2002 and followed by a decreasing trend afterwards.

4.4.2 Discussion

EMD on Chl *a* / K_d could reveal different oscillatory modes of these parameters. An annual cycle was common for each of the parameters with periodicities ranging from one to five years. These periodic oscillations were consistent with earlier studies. For example, based on wavelet analysis, Kumar and Sanilkumar (2005) identified annual oscillations of SSH along the southwest coast of India. Using seasonal anomalies Huang and Kinter III (2002) observed inter-annual variability in the heat content, SST, surface wind stress and precipitation anomalies in the tropical Indian Ocean. This analysis demonstrates that a coupled ocean–atmosphere oscillation with a periodicity of 2 to 5 years is the major factor in the tropical Indian Ocean showing significant correlation with ENSO variability in the Pacific Ocean. Khan et al. (2008) observed an inter-annual mode of oscillations of 2-3 years and 5-6 years in the SST in the north Arabian Sea. White (2000) observed Rossby waves with periodicity three to four years in the south Indian Ocean. Brandt et al. (2002) observed seasonal fluctuations in the Arabian Sea associated with westward propagating annual Rossby waves radiated from the western side of the Indian subcontinent forced by wind-stress curl. Yang et al. (1998) used a nonlinear, 2.5 layer, reduced gravity model to establish Kelvin and Rossby wave-induced seasonal variation in the sea level in the Indian Ocean. During winter monsoon, the area is influenced by coastal Kelvin waves which propagate Rossby waves (Bruce et al., 1998; Shankar and Shetye, 1997). The downwelling of Kelvin wave in the southeastern Arabian Sea showed large inter-annual variability (Rao et al., 2009).

AOD was influenced by oscillation with periodicities of one to five years. Annual and biennial oscillations were common in selected areas. Nair et al. (2012) showed a biennial variability of AOD in the Arabian Sea due to the combined effects of wind generated sea-salt aerosols and dust transported from Arabia. Kane (1992) observed oscillatory mode in the range of 2-3 years and 3-5 years in the concentration of surface aerosols. A similar pattern of a 2-3 year oscillation was observed in the monthly mean of AOD due to quasi-biennial oscillation (Beegum et al., 2009).

Chapter 5

Correlation between SST and Chl a / K_d

High Chl *a* / K_d corresponding to low SST during the southwest monsoon period (Chapters 3 and 4) suggest the existence of an inverse relation between them. Feasibility of developing parametric equations based on the underlying relation has already been attempted in Chapter 3, utilising the climatologically averaged data sets for each month from January to December i.e. the data sets without the signals of inter-annual variability. This Chapter deals with the same concept of developing parametric equations, but in a detailed manner including for different regions. In order to achieve this, regression analysis was initially carried out using all the collocated SST from MODIS_AQUA and Chl *a* / K_d from SeaWiFS for Area 1 and thereafter all subareas (Zone 1 and 2 and Grids 1a-3a) for the entire study period available separately for each month. Subsequently, analysis was performed using collocated SST from *in situ* observations and Chl *a* / K_d from SeaWiFS and MODIS_AQUA off Kochi. An attempt was also made to derive back the SST from Chl *a* and K_d utilising all the newly developed equations. Offshore grids (Grid 1b to 3b) were not considered for the analysis, as Chl *a* / K_d (< 1.0 $mg.m^{-3}$/ < 0.08 m^{-1}) was low and intra-annual variability were not conspicuous in these grids.

5.1 Regression analysis between satellite SST and Chl *a* / K_d

5.1.1 Results

Statistical analysis revealed the existence of exponential relationship between SST and Chl *a* / K_d (Figure 5.1 - 6). Therefore, to express this relationship properly, semi-logarithmic plots are presented in this study. The equations along with number of points and coefficient of determination (r^2) are also provided.

a. Area 1

In general, there was an inverse relation between SST and Chl *a* / K_d during May - September (Figure 5.1) and weakened thereafter. The corresponding equations are as follows

Ln (Chl) = -a SST + b .... (5.1)

Ln (K_d) = -c SST + d .... (5.2).

where ‘a’ varied from -0.35 to -1.2 and ‘b’ from 8.75 to 33.6 during the period May-September. In the case of K_d, ‘c’ varied from -0.21 to -0.80 and ‘d’ from 3.15 to 19.78.

Among the equations, the maximum slopes (‘a’) and r^2 (~0.45) were found during July and August, indicated the occurrence of mature phase of correlation in those months (Figure 5.1.a). K_d also exhibited similar relationships with SST as seen with Chl *a* (Figure 5.1.b).

It is also observed wide spread on the data points in all the figures, which is attributed to inter-annual variability.

b. Zone 1 and 2

In Zone 1, though the r^2 was maximum (> 0.40) during August, the relationship between SST and Chl *a* / K_d was seen all through the months from May to September (Figure 5.2). Contrary to this, the relationship was not that evident in any of the months in Zone 2 (Figure 5.3).

c. Grids 1, 2 and 3

It is found that the correlation commenced by May and persisted up to October in Grid 1a (Figure 5.4). Unlike Grid 1a, Grid 2a and 3a showed relation only during less number of months (Figure 5.5 and 5.6) i.e., during July – October and July - August respectively. So, this observation also reconfirmed that the relationship starts at south and progresses towards north in the subsequent months.

The above analysis, thus revealed that an inverse relation exist between SST and Chl *a* / K_d during the southwest monsoon period in all the selected regions and shows both spatial and temporal variability. Among them, relation is more visible towards south and persists for longer duration.

5.1.2 Discussion

SST and Chl *a* showed inverse relationship in various oceanic regions such as north California (Hood et al., 1990), US coast (Yoder et al., 2002), Gulf of Mexico (Muller-Karger et al., 1991), Benguela and Agulhas regions (Demarcq et al., 2003), north Atlantic (Perez et al., 2005), northwest Atlantic (Stegmann and Ullman, 2004), western south Atlantic (Saraceno et al., 2005), south Atlantic Bight (Barnard et al., 1997; Miles and He, 2010), Alboran Sea (Arnone R. A., 1987), Iberia (Palenzuela et al., 2002; Smyth et al., 2001), south Java of Indonesia (Pranowo et al. 2003), south China Sea (Yuan-Jian et al., 2012), northeast Arabian Sea and Bay of Bengal (Kumari and Babu, 2009; Solanki et al., 2001), Pacific Ocean (http://disc.sci.gsfc.nasa.gov), Antarctica (Arai et al., 2005) and Sargasso sea (http://disc.sci.gsfc.nasa.gov). Among them, both logarithmic and linear relations were reported.

Goes et al. (2005) observed a linear correlation between SST and Chl *a* in the western Arabian Sea during the southwest monsoon period as follows:

Chl *a* = -0.10 SST + 3.29 .... (5.3)

Perez et al. (2005) observed a linear equation between the parameters in the eastern (20-0^{o}W; 0-10^{o}S) and western Atlantic Ocean (20-30^{o}W; 10^{o}N-10^{o}S) during summer and found the coefficient varied (Eqn. 5.6-7) as follows:

Eastern Atlantic, Chl $a = -0.12$ SST $+ 3.50$ ………………….. (5.6)

Western Atlantic, Chl $a = -0.10$ SST $+ 2.87$ ……….………… (5.7)

In addition, Yuan-Jian et al. (2012) established a linear relation in the Vietnam waters during the summer (Eqn. 5.8).

Chl $a = -0.05 *$ SST ………………………….. (5.8)

5.2 *In situ* SST and satellite Chl *a* / K$_d$

5.2.1 *In situ* SST observations

Significant correlation was observed between satellite SST and Chl *a* / K$_d$ off the southwest coast of India during the southwest monsoon period indicating its usefulness to study upwelling features. However, satellite SST has poor accuracy compared with *in situ* ones. Therefore, to improve the equations, SST from *in situ* observations off Kochi (74.0 ^{o} E – 77.0 ^{o} E, 8.5 ^{o} N – 11.5 ^{o} N) between various phases of upwelling during 1998 – 2009 were used (Figure 5.7).

In general, the contours of SST off Kochi during the southwest monsoon period were parallel and closely spaced towards the coast (Figure 5.7). Low SSTs were observed towards the coast and high SST towards offshore indicating the existence of upwelling front (Beletsky et al., 1997).

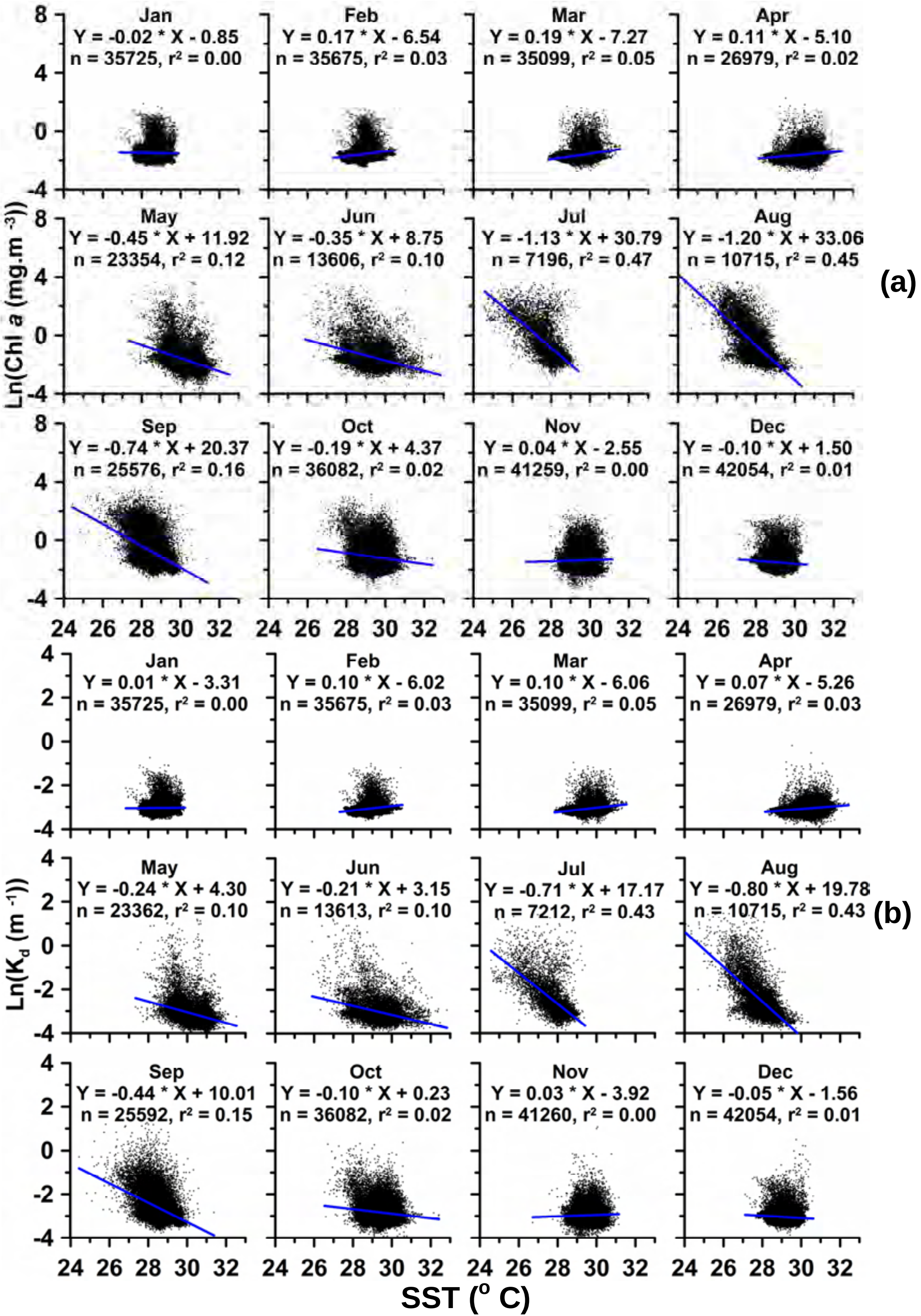

Figure 5.1. Regression analysis between SST and (a) Chl *a* and (b) K_d in Area 1.

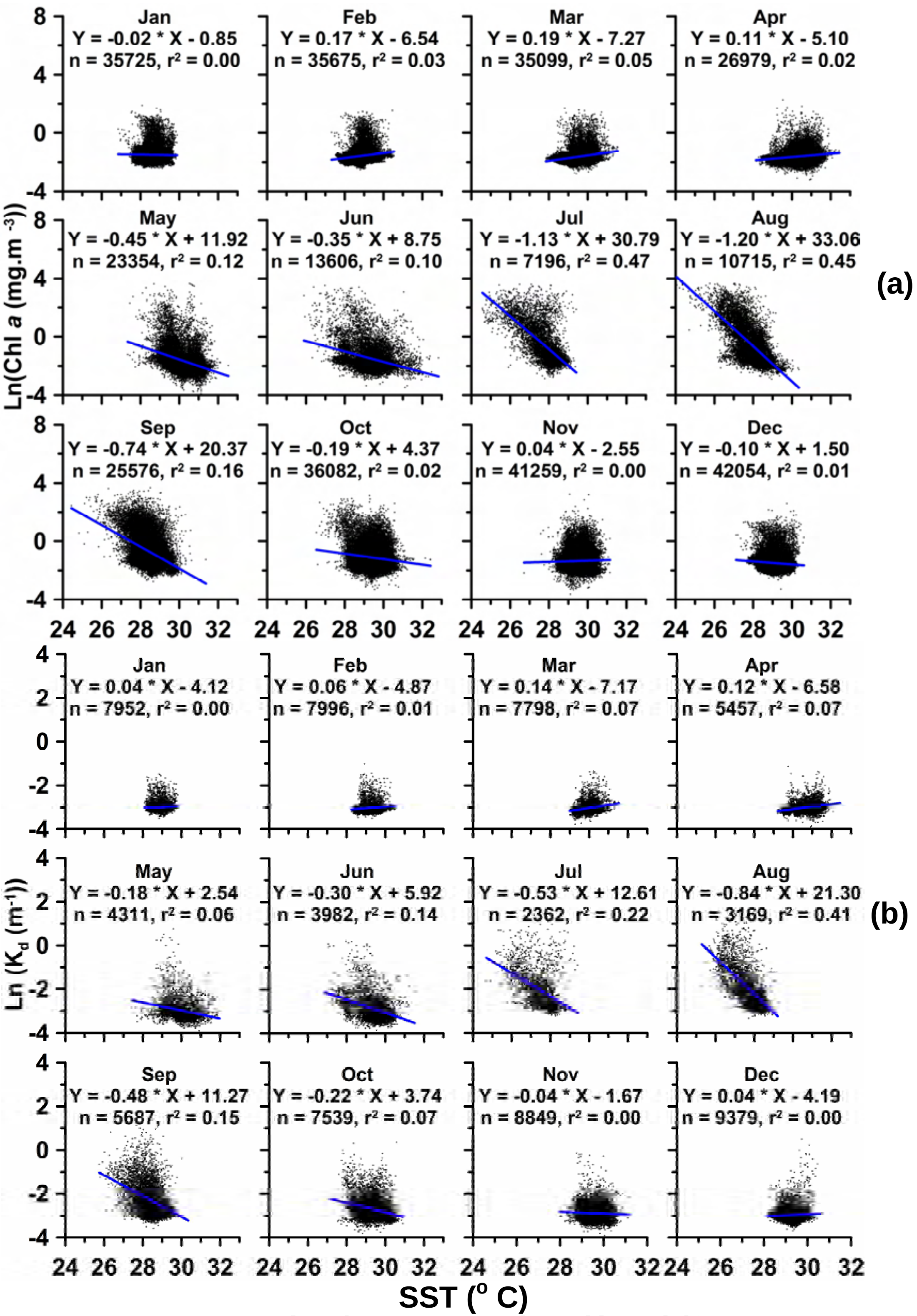

Figure 5.2. Regression analysis between SST and (a) Chl *a* and (b) K_d in Zone 1.

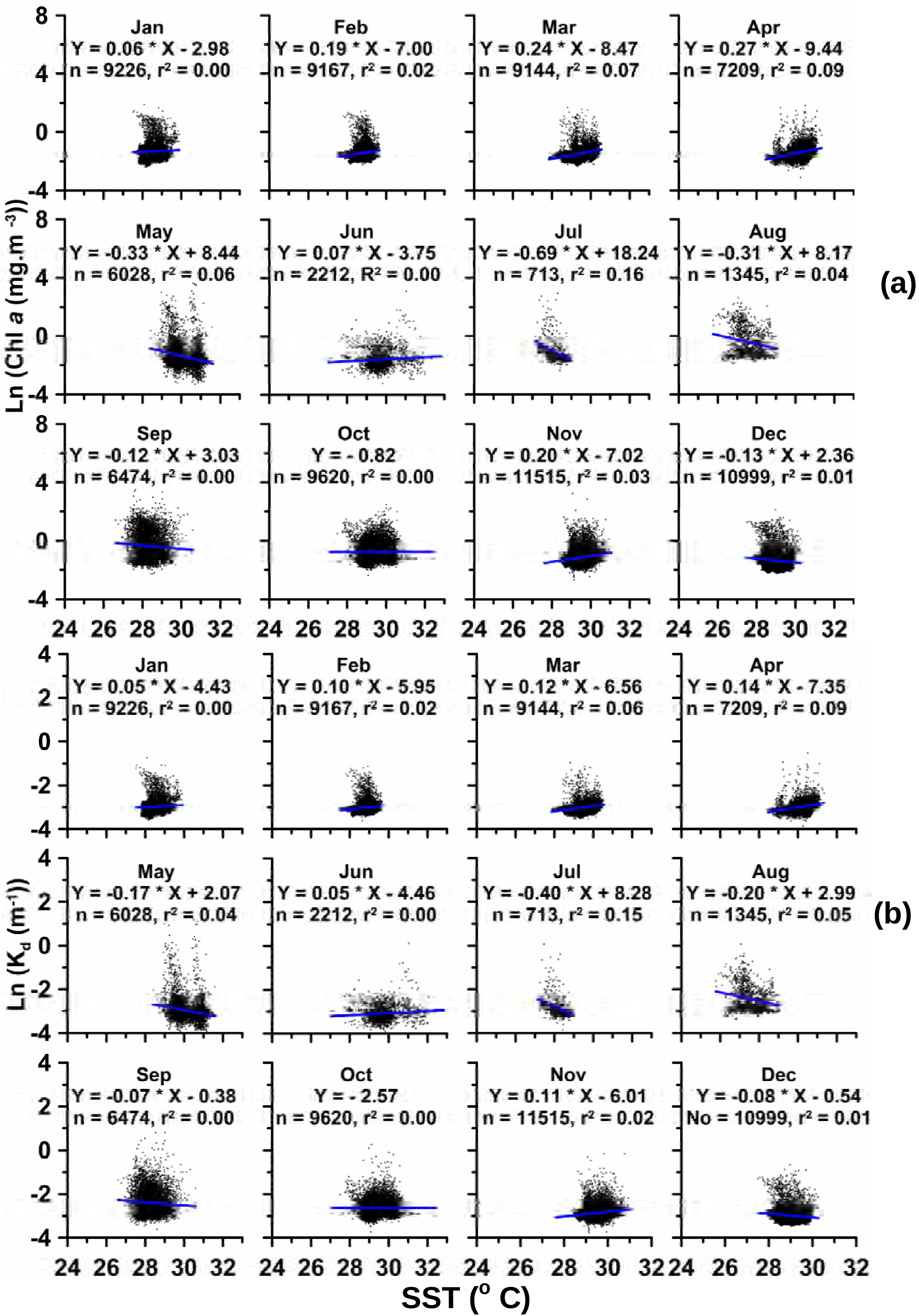

Figure 5.3. Regression analysis between SST and (a) Chl *a* and (b) K_d in Zone 2.

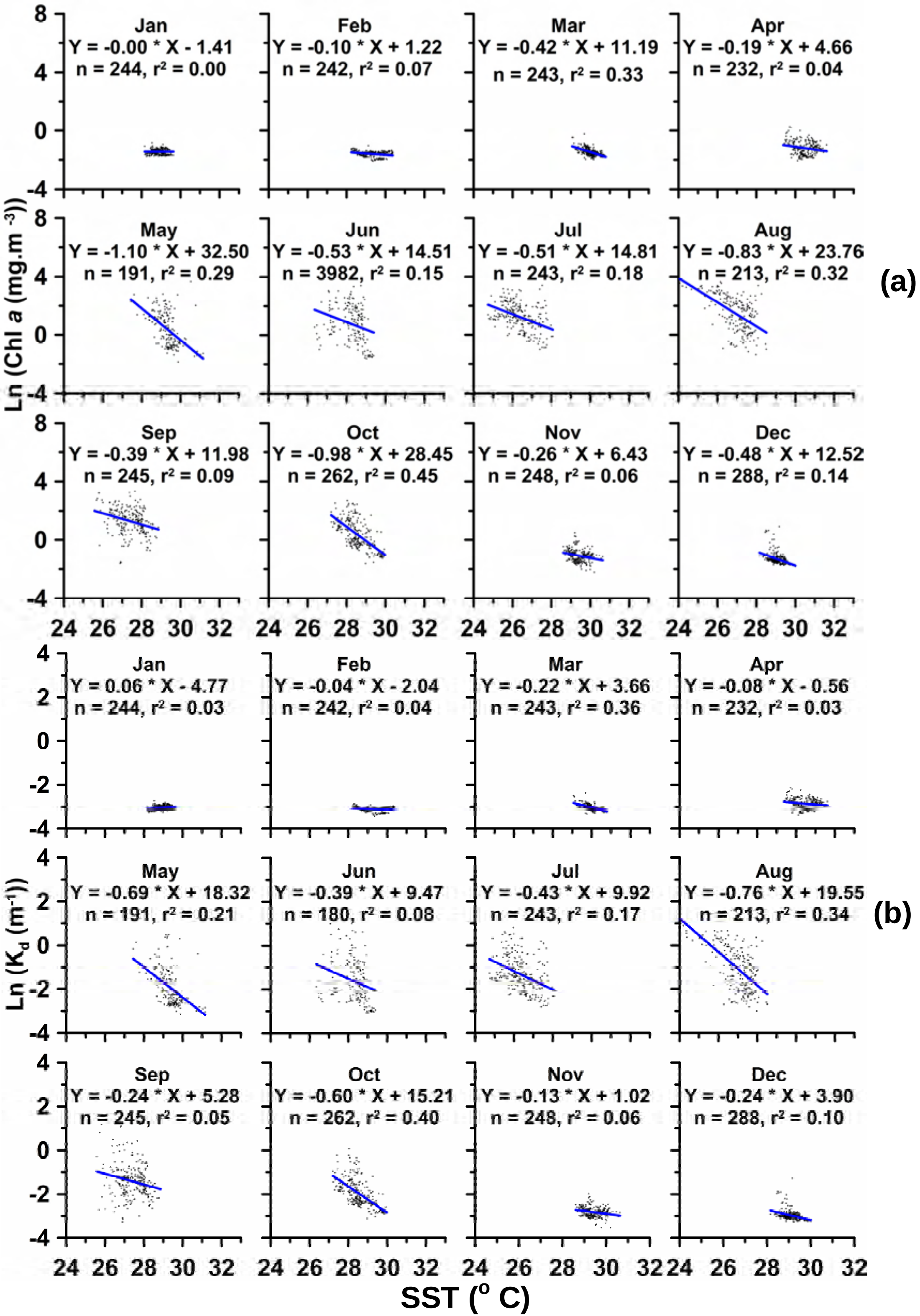

Figure 5.4. Regression analysis between SST and (a) Chl *a* and (b) K_d in Grid 1a.

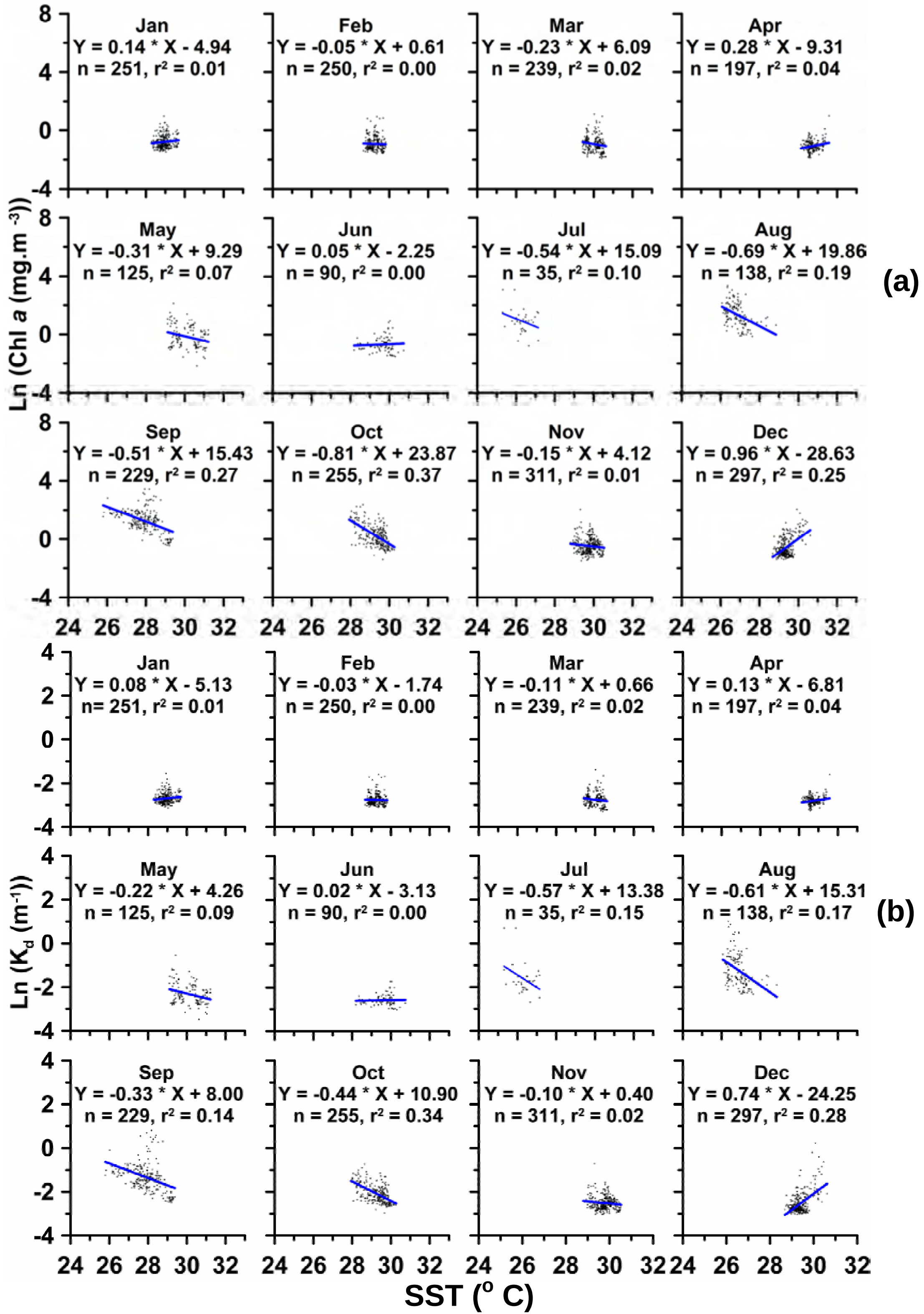

Figure 5.5. Regression analysis between SST and (a) Chl *a* and (b) K_d in Grid 2a.

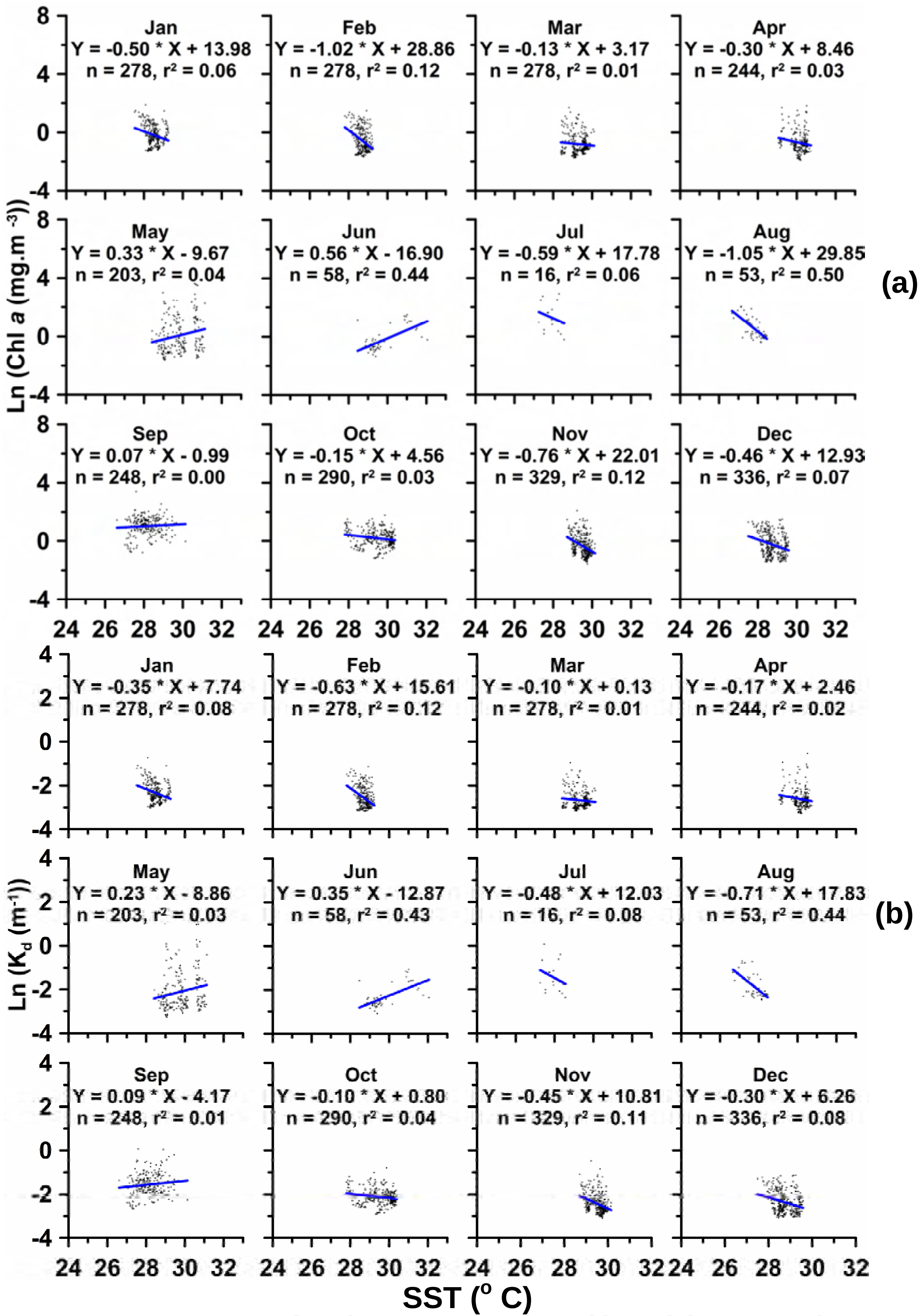

Figure 5.6. Regression analysis between SST and (a) Chl *a* and (b) K_d in Grid 3a.

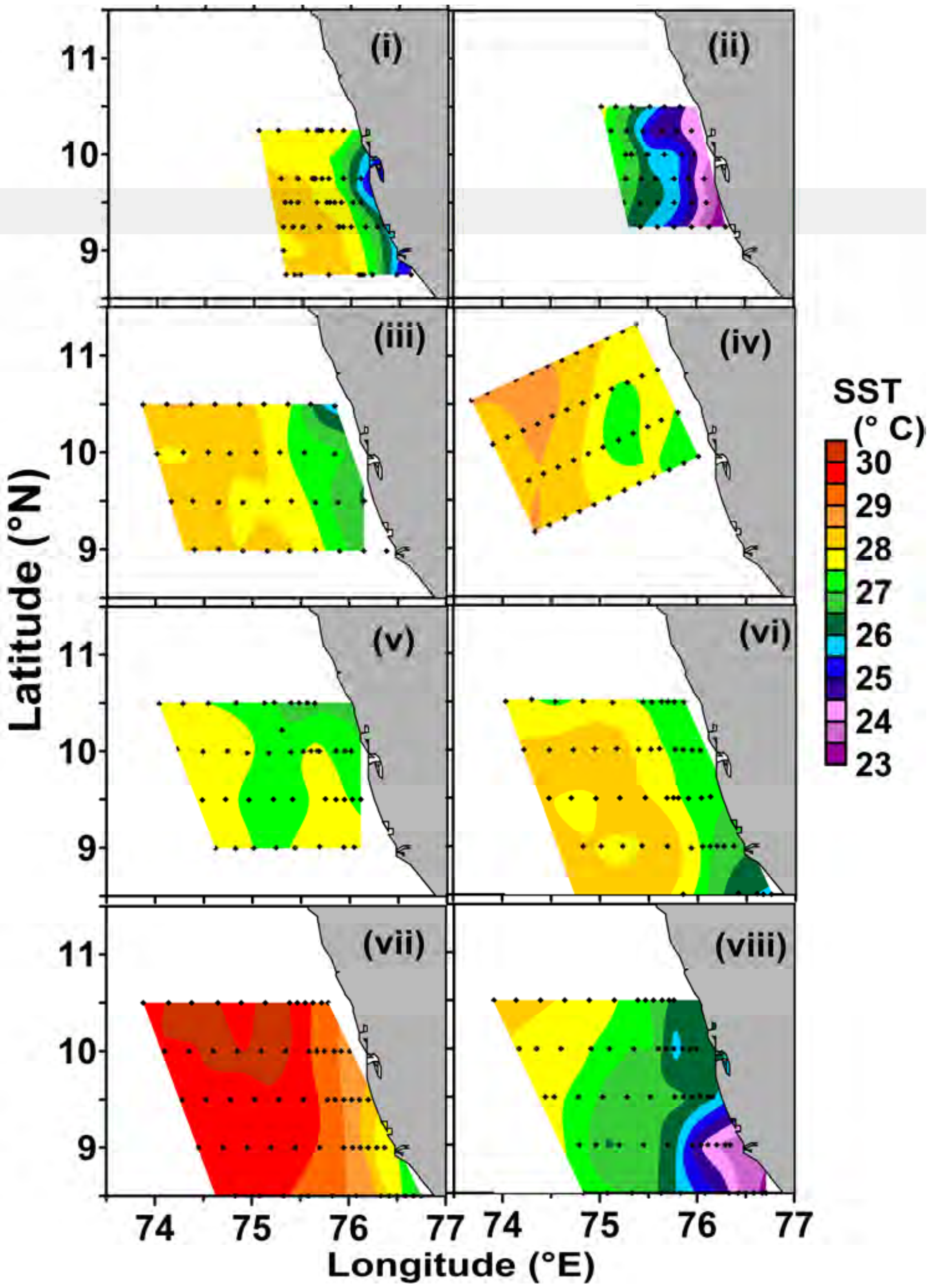

Figure 5.7. Contour maps of *in situ* SST during (i) 13 – 17 August 1998, (ii) 10 – 12 July 2000, (iii) 14 – 18 July 2003, (iv) 7 – 11 June 2004, (v) 3, 6 – 9 August 2007, (vi) 3 – 7 September 2007, (vii) 1 – 5 June 2009 and (viii) 8 – 12 July 2009.

During 13 – 17 August 1998, SST was low (< 26.5 ^{o}C) in the coastal waters, which progressively increased to greater than 27.5^{o}C beyond 110 km from the coast (Figure 5.7.i.). Thus, in general, SST gradient of ~0.015 ^{o}C/km was observed during the period. Among the selected cases, lowest temperature of the coastal waters (~ 24.0 ^{o}C) was observed during 10 – 12 July 2000 (Figure 5.7.ii), which spread along the entire coastal area up to 30 km towards offshore from the coastline producing a significant cross-shore gradient (~0.027 ^{o}C/km). Cross-shore gradient during July 2003 was found to be ~ 0.009^{o}C/km (Figure 5.7.iii). The frontal structures were not as prominent during June 2004 (Figure.5.7.iv) and August 2007 (Figure 5.7.v) as seen in the previous cases. The cross-shore gradient in SST during September 2007, June 2009 and July 2009 were very high towards south and low towards north. This indicated spatial variability in the frontal structure. Thus, among the eight observations, weaker (June 2004 and August 2007) and stronger (July 2000 and July 2009) upwelling events were observed. This inference was made based on SST gradient and lowest temperatures nearer the coast. Inter-annual variability on the upwelling features was also evident from the above observations. For example, the upwelling front was more visible and SST was higher in June 2009 compared to that of June 2004. Among the observations during July also, upwelling characteristics were significantly different for different years (2000, 2003 and 2009). Similarly, month of August also, exhibited different characteristics during different years (1998 and 2007).

5.2.2 Regression analysis

In the following section, regression analysis was carried out with the *in situ* data sets mentioned above. Ideally, this analysis has to be carried out with the collocated / matching data points within the acceptable time window from the satellite observations. However, due to cloud cover, matched Chl *a* / K_d satellite observations at the time of *in situ* measurements were found sparse. Hence, the time windows were increased to daily, 3 day, 8 day, monthly and climatology to obtain more collocated data points. Number of pixels of satellite images collocated with *in situ* observations are listed in Table 5.1. Among the eight *in situ* observations, collocated Chl *a* / K_d on all time scales i.e., daily, three day and eight day composite were obtained only for June 2009 and that too only from one satellite, MODIS_AQUA. Next higher time windows, where maximum data points were available, were the monthly and climatology scale.

Table 5.1. Number of collocated data points between *in situ* SST and Chl *a* / K_d at various time windows viz. daily (D), 3 day (3D), 8 day (8D), monthly (M) and climatology (MC) off Kochi. The data set, selected to perform regression analysis are demarcated by yellow colour.

SI No.	**Period of *in-situ* observation**	**No. of data points**	**Collocated points**									
			SeaWiFS					**MODIS_AQUA**				
			D	**3D**	**8D**	**M**	**MC**	**D**	**3D**	**8D**	**M**	**MC**
1.	13-17 Aug 1998	70	0	0	0	7	**70**	-	-	-	-	**70**
2.	10-12 Jul 2000	37	0	0	0	12	**36**	-	-	-	-	**33**
3.	14-18 Jul 2003	35	0	0	0	2	**33**	0	0	0	3	**28**
4.	7-11 Jun 2004	47	0	0	0	17	**47**	0	0	0	2	**46**
5.	3-9 Aug 2007	42	3	6	6	9	**40**	0	2	2	6	**40**
6.	3-7 Sep 2007	53	1	1	1	31	**51**	0	0	5	**25**	**53**
7.	1-5 Jun 2009	60	0	0	0	9	**59**	**9**	**22**	**24**	**36**	**58**
8.	8-12 Jul 2009	59	0	0	0	23	**57**	0	0	0	**11**	**54**

During June 2009, when data points were available in all the time windows, good correlation was found to exist between SST and Chl *a* / K_d in all the cases

(Figure 5.8). The r^2 was found decreasing, when the time windows were widened. However, it is to be noted that the slope as well as similar relationship maintained for all the time windows for both Chl *a* / K_d. This observation indicated that even with the climatology data set, one can think of to correlate the same with *in situ* observations on SST. This is useful, when sufficient data points are not available from matching real time data. However, error analysis is also to be carried out to confirm this hypothesis. Therefore, such analysis was performed subsequently in the later part of this study (Table 5.2 and 5.3).

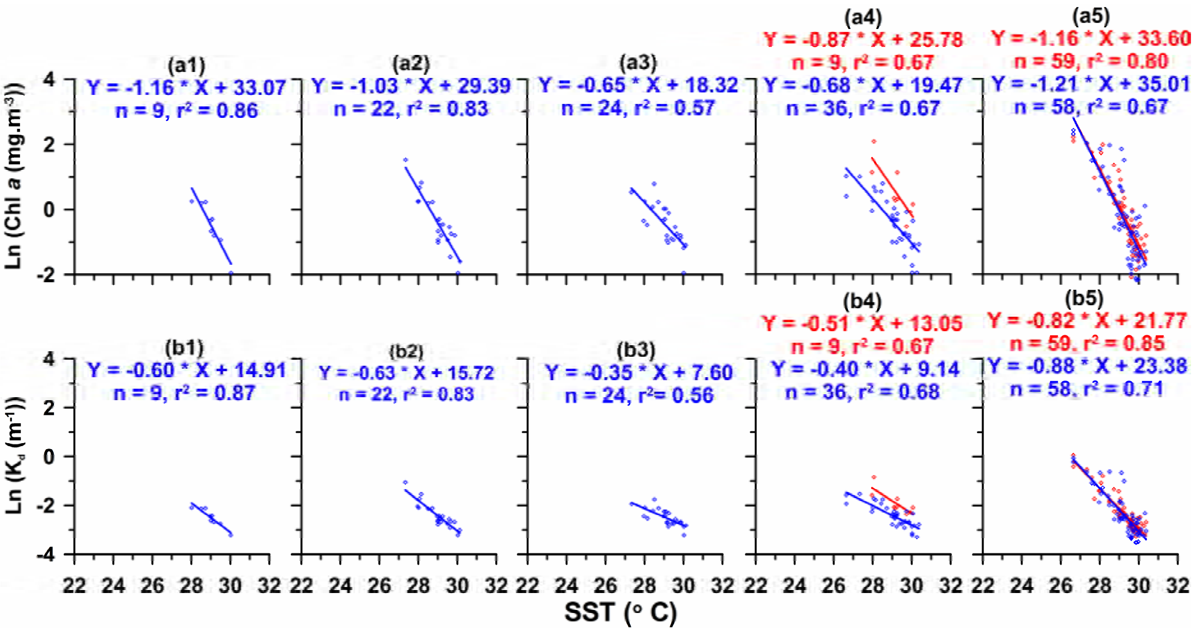

Figure 5.8. Regression analysis of *in situ* SST with (a) collocated Chl *a* and (b) K_d at various temporal scales of (1) daily, (2) 3 day, (3) 8 day, (4) monthly and (5) climatology during June 2009. Red represents SeaWiFS and blue MODIS_AQUA.

In general, the analysis utilising collocated data points on climatology of Chl *a* and K_d from both SeaWiFS and MODIS_AQUA showed good relation (Figure 5.9). However, during August 2007 the relationship was very poor. On closer look, it is very clear that upwelling was very weak during this period. Good correlation (r^2 >

0.40) was observed during July 2003, June 2004, September 2007, June 2009 and July 2009, when upwelling was strong as evident from the front and low SSTs.

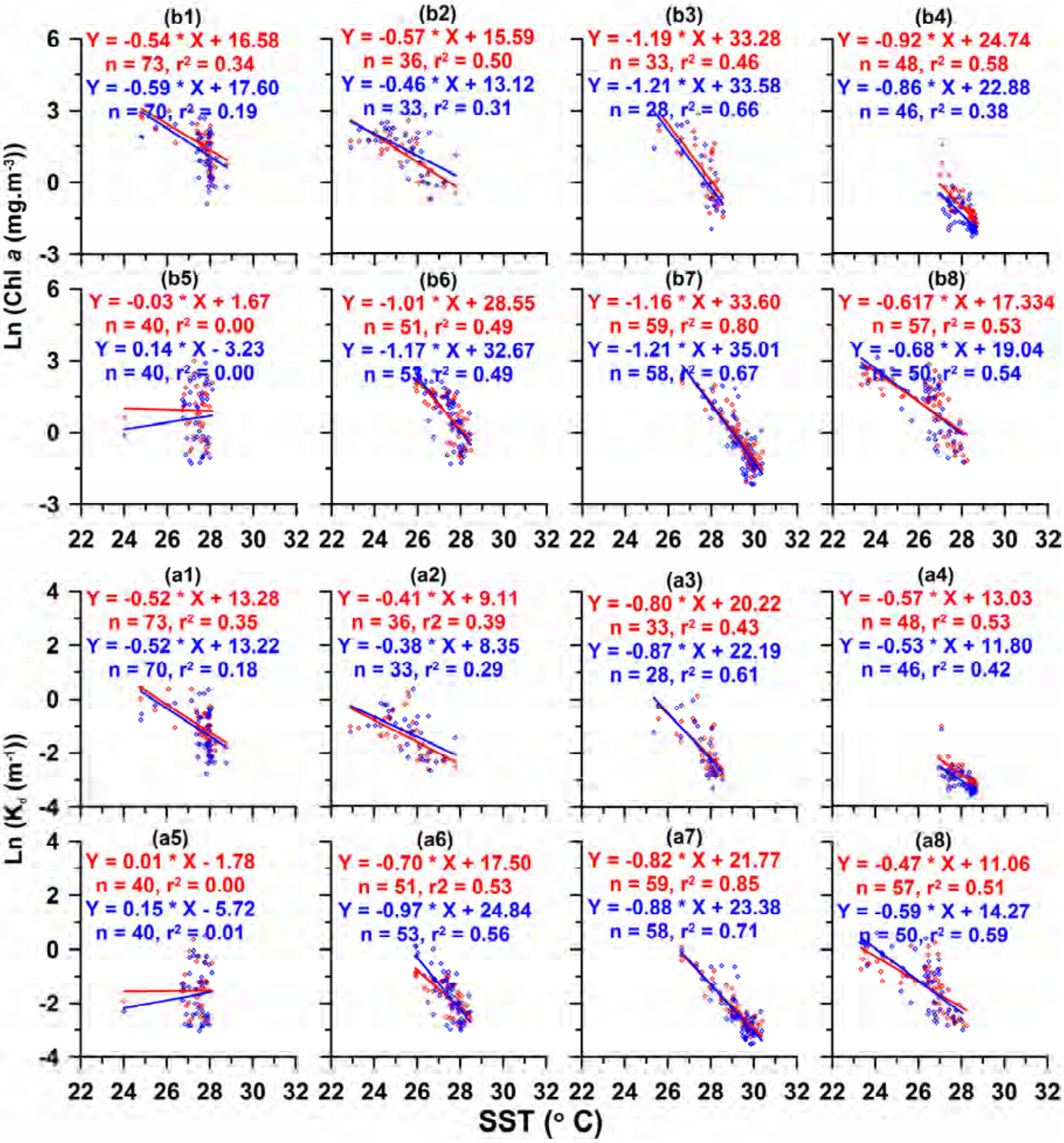

Figure 5.9. Regression analysis of *in situ* SST with collocated monthly climatology of (a) Chl *a* and (b) K_d during (1) August 1998, (2) July 2000, (3) July 2003, (4) June 2004, (5) August 2007, (6) September 2007, (7) June 2009 and (8) July 2009. Red represents SeaWiFS and blue MODIS_AQUA.

The above empirical relations were utilised to invert back SST from Chl *a* of SeaWiFS / MODIS_AQUA (Table 5.2.a / 5.3.a) and K_d (Table 5.2.b / 5.3.b) during the respective periods utilising all the newly developed empirical equations. The Root Mean Square Deviation (RMSD) and error percentage in inverting back SST were estimated from the following formulae and also included in the above Table:

$$\mathrm{RMSD} = \sqrt{\frac{\sum (X_{actual} - X)^2}{n}} \quad \ldots\ldots\ldots\ldots\ldots\ldots\ (5.9)$$

$$\text{Error Percentage} = \left| \frac{X_{actual} - X}{X_{actual}} \right| 100 \quad \ldots\ldots\ldots\ldots\ldots\ldots\ (5.10)$$

where, X_{actual} represent the *in situ* SST observation, X is the derived SST utilising the new equations, and ‘n’ number of observations.

Table 5.2. Regression analysis between *in situ* SST and Chl *a* / K_d of SeaWiFS at various time windows viz. daily (D), 3day (3D), 8 day (8D), monthly (M) and climatology (MC). ‘n’ represents the number of data points used, Chl_S and Kd_S are Chl *a* and K_d from SeaWiFS sensor, r^2 is the coefficient of determination, RMSD is Root mean square deviation of estimated SST and err % is error percentage.

Time scale		**Equation**	**n**	**r^2**	**RMSD (^{o} C)**	**Err %**	**Eqn no**
Satellite	***In situ***						
MC	13-17 Aug 98	Chl_S=$e^{(-0.54*SST +16.58)}$	73	0.34	0.62	1.57	5.11
MC	10-12 Jul 00	Chl_S=$e^{(-0.57*SST +15.59)}$	36	0.50	0.80	2.53	5.12
MC	14-18 Jul 03	Chl_S=$e^{(-1.19*SST +33.28)}$	33	0.46	0.48	1.27	5.13
MC	7-11 Jun 04	Chl_S=$e^{(-0.92*SST +24.74)}$	48	0.58	0.33	0.91	5.14
MC	3-9 Aug 07	Chl_S=$e^{(-0.03*SST +1.67)}$	40	0.00	0.65	1.55	5.15
MC	3-7 Sep 07	Chl_S=$e^{(-1.01*SST +28.55)}$	51	0.48	0.47	1.45	5.16
MC	1-5 Jun 09	Chl_S=$e^{(-1.16*SST +33.60)}$	59	0.80	0.30	1.03	5.17
MC	8-12 Jul 09	Chl_S=$e^{(-0.62*SST +17.33)}$	57	0.53	0.94	2.93	5.18
MC	13-17 Aug 98	Kd_S=$e^{(-0.52*SST +13.28)}$	73	0.35	0.62	1.58	5.19
MC	10-12 Jul 00	Kd _S=$e^{(-0.41*SST +9.11)}$	36	0.39	0.89	2.75	5.20
MC	14-18 Jul 03	Kd _S=$e^{(-0.80*SST +20.22)}$	33	0.43	0.49	1.27	5.21
MC	7-11 Jun 04	Kd_S=$e^{(-0.57*SST +13.03)}$	48	0.53	0.35	1.02	5.22
MC	3-9 Aug 07	Kd_S=$e^{(0.01*SST -1.78)}$	40	0.00	0.65	1.55	5.23
MC	3-7 Sep 07	Kd_S=$e^{(-0.70*SST +17.50)}$	51	0.53	0.45	1.40	5.24
MC	1-5 Jun 2009	Kd_S=$e^{(-0.82*SST +21.77)}$	59	0.85	0.33	0.91	5.25
MC	8-12 Jul 2009	Kd_S=$e^{(-0.47*SST +11.06)}$	57	0.51	0.96	2.92	5.26

Table 5.3. Regression analysis between *in situ* SST and Chl *a* / K_d of MODIS_AQUA at various time windows viz. daily (D), 3day (3D), 8 day (8D), monthly (M) and climatology (MC). 'n' represents the number of data points used, Chl_M and Kd_M are Chl *a* and K_d from MODIS_AQUA sensor, r^2 is the coefficient of determination, RMSD is Root mean square deviation of estimated SST and err % is error percentage.

Time scale		**Equation**	**n**	**r^2**	**RMSD (^{o} C)**	**Err %**	**Eqn no**
Satellite	***In situ***						
MC	13-17 Aug 98	$Chl\_M=e^{(-0.59*SST +17.60)}$	70	0.19	0.64	1.45	5.27
MC	10-12 Jul 00	$Chl\_M=e^{(-0.46*SST +13.12)}$	33	0.31	0.92	2.67	5.28
MC	14-18 Jul 03	$Chl\_M=e^{(-1.21*SST +33.58)}$	28	0.66	0.53	1.46	5.29
MC	7-11 Jun 04	$Chl\_M=e^{(-0.86*SST +22.88)}$	46	0.38	0.40	1.18	5.30
MC	3-9 Aug 07	$Chl\_M=e^{(0.14*SST -3.23)}$	40	0.00	0.66	1.58	5.31
MC	3-7 Sep 07	$Chl\_M=e^{(-1.17*SST +32.67)}$	53	0.49	0.47	1.40	5.32
D	1-5 Jun 09	$Chl\_M=e^{(-0.92*SST +24.74)}$	8	0.89	0.18	0.55	5.33
3D		$Chl\_M=e^{(-0.92*SST +24.74)}$	19	0.76	0.31	0.88	5.34
8D		$Chl\_M=e^{(-0.92*SST +24.74)}$	20	0.56	0.40	1.10	5.35
M		$Chl\_M=e^{(-0.92*SST +24.74)}$	30	0.60	0.41	1.07	5.36
MC		$Chl\_M=e^{(-1.21*SST +35.01)}$	58	0.60	0.48	1.30	5.37
MC	8-12 Jul 09	$Chl\_M=e^{(-0.68*SST +19.04)}$	50	0.54	0.91	3.05	5.38
MC	13-17 Aug 98	$Kd\_M=e^{(-0.52*SST +13.22)}$	70	0.18	0.64	1.44	5.39
MC	10-12 Jul 00	$Kd\_M=e^{(-0.38*SST +8.35)}$	33	0.29	0.93	2.66	5.40
MC	14-18 Jul 03	$Kd\_M=e^{(-0.87*SST +22.19)}$	28	0.61	0.56	1.50	5.41
MC	7-11 Jun 04	$Kd\_M=e^{(-0.53*SST +11.80)}$	46	0.42	0.39	1.15	5.42
MC	3-9 Aug 07	$Kd\_M=e^{(0.15*SST -5.72)}$	40	0.01	0.65	1.58	5.43
MC	3-7 Sep 07	$Kd\_M=e^{(-0.97*SST +24.84)}$	53	0.56	0.44	1.29	5.44
D	1-5 Jun 2009	$Kd\_M=e^{(-0.92*SST +24.74)}$	8	0.91	0.17	0.52	5.45
3D		$Kd\_M=e^{(-0.92*SST +24.74)}$	19	0.79	0.29	0.83	5.46
8D		$Kd\_M=e^{(-0.92*SST +24.74)}$	20	0.55	0.40	1.11	5.47
M		$Kd\_M=e^{(-0.92*SST +24.74)}$	30	0.57	0.42	1.08	5.48
MC		$Kd\_M=e^{(-0.88*SST +23.38)}$	58	0.71	0.46	1.24	5.49
MC	8-12 Jul 2009	$Kd\_M=e^{(-0.59*SST +14.27)}$	50	0.59	0.93	2.66	5.50

Altogether, the error percentage ranged from 0.20 to 3.50%. It was low (<1.50%) during June 2009, June 2004, July 2003, August 1998 and September 2007 when upwelling was strong. Even after taking the widest time window i.e. climatology, the error percentage were limited within 3.00% and that too with < 1.50% during most of the period. These results prompt to believe that monthly climatology of ocean colour data can be utilised, to derive SST when the real-time data are sparse.

5.3 Contour maps of inverted SSTs

It has already been brought out that monthly climatology of Chl *a* and K_d holds good correlation with *in-situ* SST during certain periods and absolute values of inverted SSTs fall within the error of 1.5 % in most of the cases. Further, to visually verify, whether the pattern also could be recaptured by the newly generated equations, the contour maps of the inverted SSTs for all the eight cases were generated from the respective equations (Figure 5.10 and 11). In general, all the equations, except the ones for August 2007, were capable to invert back the pattern of *in situ* SST to a great extent. Among them, the most suitable equations are the ones that developed for June 2009. In this case, it was observed that the distribution patterns of Chl *a* / K_d and *in situ* SST were more or less similar in nature. During the other cases, the inverted SSTs captured the pattern partly relative to the difference in the patterns of correlating parameters. It is to be noted that during August 2007, the inverted SSTs nearly failed to reproduce the features that were seen in the *in situ* observations. This is attributed to the totally different pattern in the distributions of *in situ* SST resulted from weak upwelling, which was evident from the absence of frontal structure in the SST pattern. Another important observation is that the inverted SST followed more of the Chl *a* pattern rather than the *in situ* SST. For example, during August 1998 and July 2000, the Chl *a* gradients were lower nearer the coast than that of in situ SST. Accordingly, the gradients in inverted SSTs were also lower nearer the coast. K_d showed the similar results as revealed from Chl *a* (Figure 5.11). Therefore, those results are not described in detail.

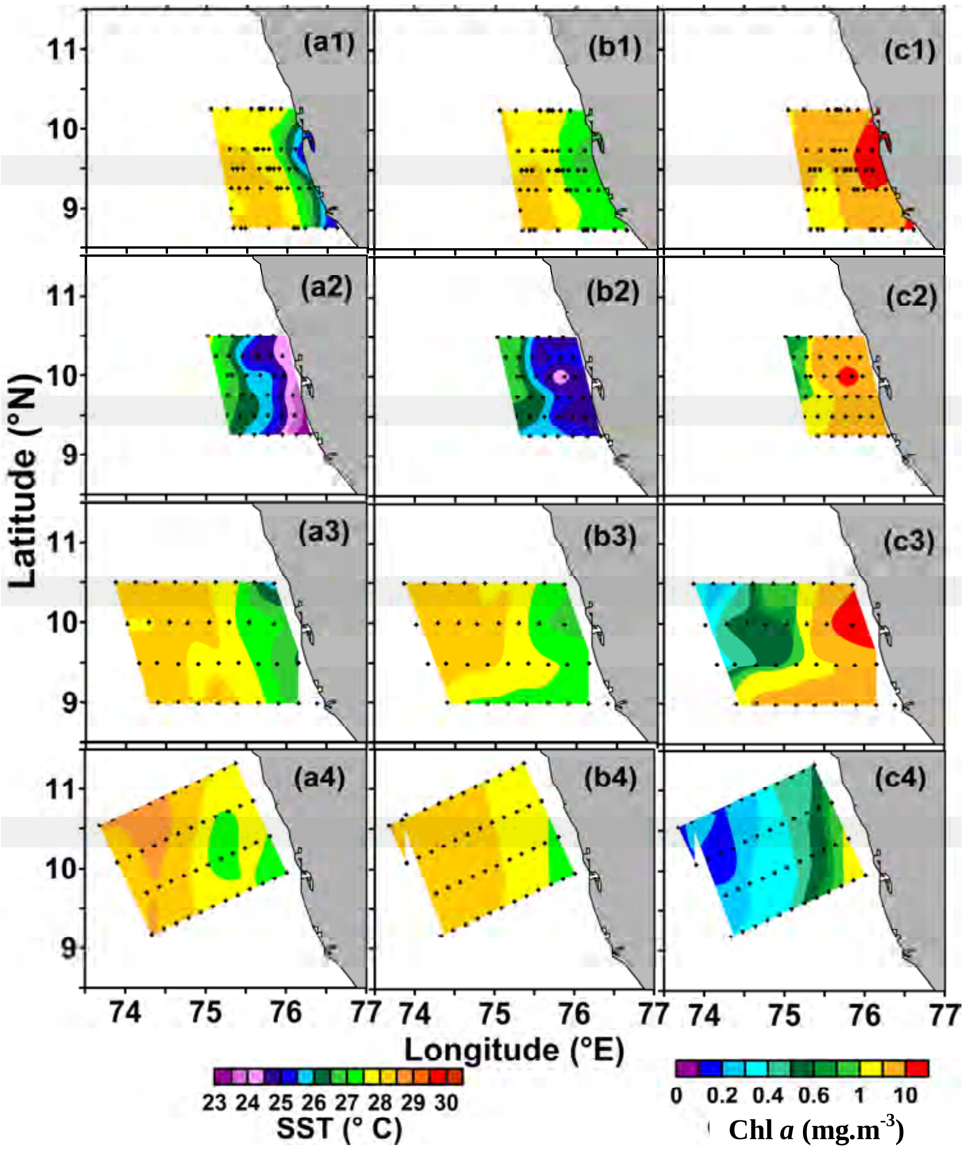

Figure 5.10.a. Contour maps of (a) *in situ* SST, (b) SST derived from Chl *a* climatology using the respective empirical equation and (c) Chl *a* climatology from SeaWiFS during (1) August 1998, (2) July 2000, (3) July 2003 and (4) June 2004

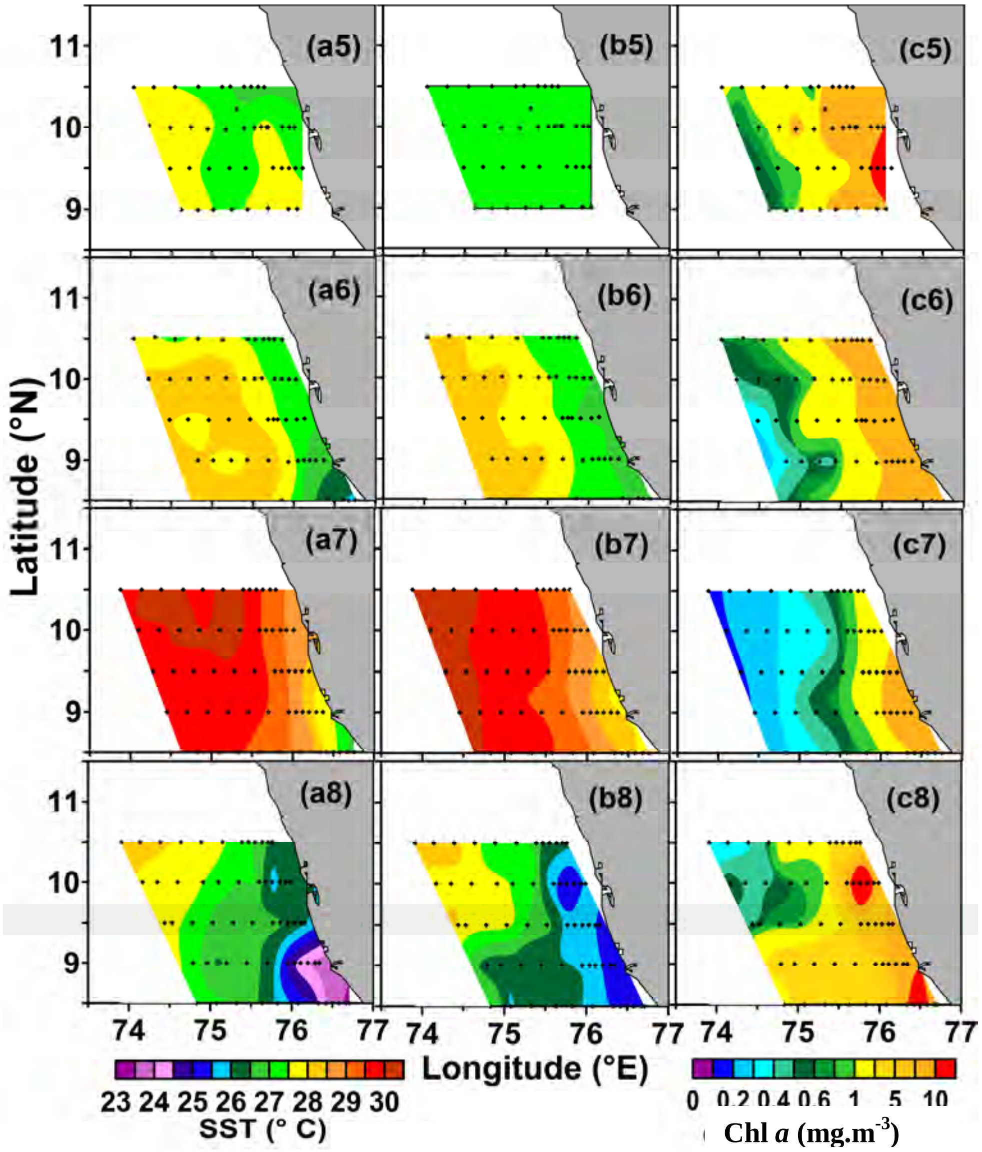

Figure 5.10.b. Contour maps of (a) *in situ* SST, (b) SST derived from Chl *a* climatology using the respective empirical equation and (c) Chl *a* climatology from SeaWiFS during (5) August 2007, (6) September 2007, (7) June 2009 and (8) July 2009.

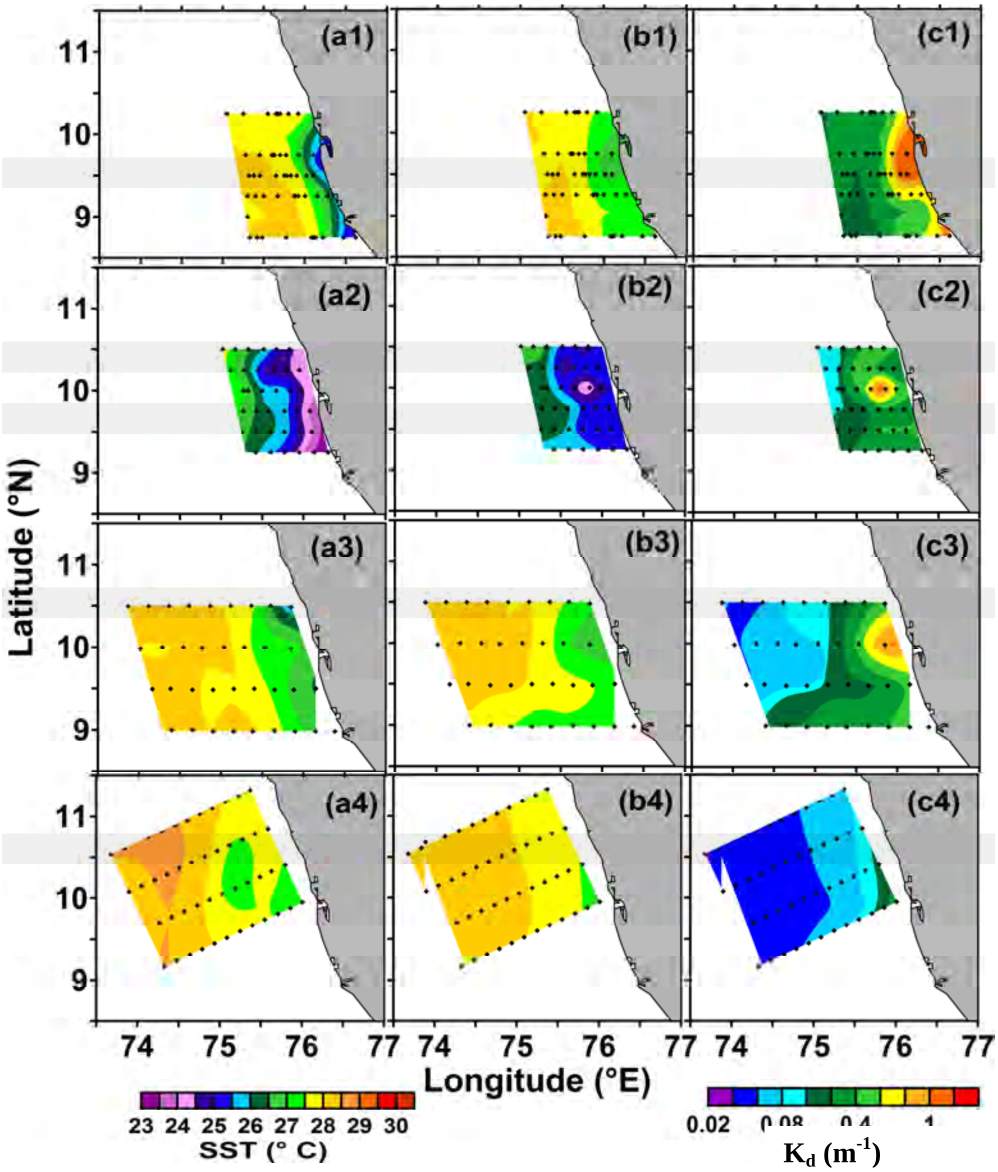

Figure 5.11.a. Contour maps of (a) *in situ* SST, (b) SST derived from K_d climatology using the respective empirical equation and (c) K_d climatology from SeaWiFS during (1) August 1998, (2) July 2000, (3) July 2003 and (4) June 2004.

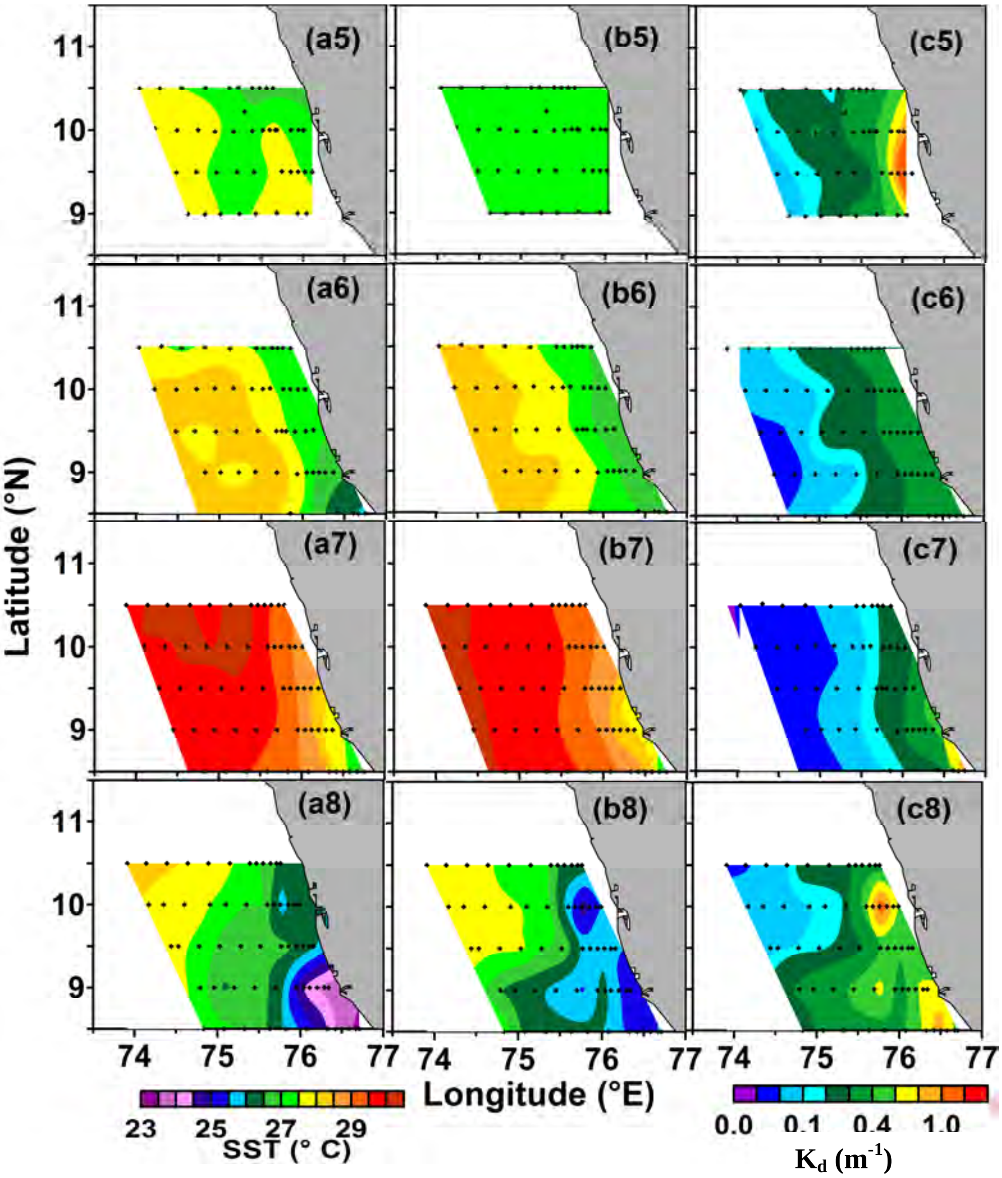

Figure 5.11.b. Contour maps of (a) *in situ* SST, (b) SST derived from K_d climatology using the respective empirical equation and (c) K_d climatology from SeaWiFS during (5) August 2007, (6) September 2007, (7) June 2009 and (8) July 2009.

The question unanswered even after the above experiment is that whether the real time data on Chl *a* / K_d will have the similar distribution pattern of *in situ* SST and if such pattern exists, whether the equations developed from these concurrent parameters will be able to reproduce the exactly similar pattern for inverted SST. The lacuna to prove this was the absence of such data sets due to cloud cover. This call for the requirement of long and very systematic data collection programs to obtain such data sets consist of simultaneous *in situ* and satellite observations. However, the present work displayed the feasibility to derive SST from satellite Chl *a* and K_d during the upwelling period off the southwest coast of India.

Chapter 6

Summary and conclusions

Earth observing satellites (EOS) continuously monitor the global oceanographic and atmospheric features and are effective in depicting environmental variability (Martin, 2004). Among all EOS sensors, ocean colour sensors make use of visible bands of electromagnetic spectrum (shorter wavelength). The shorter wavelength enables ocean colour sensor to resolve spatial features at fine resolution (~ 250 m). Hence, these datasets can be utilised to depict the oceanographic and atmospheric features at fine scale of any region having significant spatio-temporal variability.

Off the southwest coast of India (70.5-77.5^{o}E, 8.0-15^{o}N) undergoes significant spatial as well as temporal variability under the influence of seasonally reversing surface winds and currents. Consequently, the region is enriched with features like upwelling, sinking, eddies, fronts, etc. Among these features, upwelling is an important oceanographic phenomenon that occurs in the study area during the southwest monsoon period. During this process, the subsurface nutrient-rich water replaces surface warm and nutrient deficit water. Consequently, primary production enhances in the area, which are reflected in ocean colour as high values of Chl *a*. Consequently, K_d also increases proportionately.

In addition, seasonally reversing atmospheric winds and rainfall over the area induces aerosol variability in the atmospheric column, which is reflected on Aerosol

Optical Depth (AOD) of ocean colour data. The present doctoral thesis focuses the utility of ocean colour data on Chl *a*, K_d and AOD in depicting the oceanographic and atmospheric features off the southwest coast of India.

Data on seasonal composites on Chl *a*, K_d and AOD archived by NASA from SeaWiFS are utilised to study the global scale variability. In addition, Chl *a*, K_d and AOD at various temporal scales viz. daily, weekly, monthly and monthly climatology from SeaWiFS (September 1997 – December 2010) and MODIS_AQUA (July 2002 – March 2012) are extracted and analysed to understand the variability in the study area in detail. SST from *in situ* observations collected onboard *INS Sagardhwani* during 1998 – 2009 off Kochi and satellite observations from MODIS_AQUA and AVHRR are utilsed. Merged SSHA, ocean surface currents form ship drift observation and ECMWF model, surface winds from NCEP / NCAR and QuikSCAT provided supporting information on environmental conditions.

Climatology of ocean colour parameters on global and regional scales is carried out to understand the significance of these parameters in representing the oceanographic / atmospheric features. The seasonal climatology shows that low Chl *a* / K_d appears in mid-ocean circulation gyres, moderate values in the equatorial regions of Pacific and Atlantic Oceans and high values in high latitudes and coastal regions. Significant seasonal variability is noticed in the north India Ocean, especially in the western part of the Arabian Sea, where intense upwelling occurs. AOD concentration exhibited a zone of comparatively dense AOD lying over the tropical regions of Atlantic and Indian throughout the year, which gets maximum density during summer that too with its epicentre off the Arabian Peninsula.

In general, Chl *a*, K_d and AOD along the southwest coast of India (70.5-77.5^{o}E, 8.0-15.0^{o}N) follows an annual cycle with their maxima during the southwest monsoon period. Moreover, significant cross-shore gradient is observed on Chl *a* and K_d during the period, with high values (>1.0 mg.m^{-3}) near the coast. This gradient develops in the south by June and propagated north such that it encompasses the entire study area by August. Similarly, the decay of the gradient starts during September from south and moves north and completes the process by November. *In situ* and satellite temperature measurements brought out similar cross-shore gradients during the southwest monsoon period. The close similarity between the distribution of Chl *a*, K_d and temperature in the study area during the southwest monsoon period, tempted to believe that Chl *a* and K_d also can be utilised to study the upwelling features apart from SST. It is well known that SST will be modulated due to upwelling and the parameter is widely used to characterise the upwelling intensity.

The spatial distribution on the three parameters showed large regional variability. Therefore, two subareas of sizes 3^o longitude x 3^o latitude grids lying towards south (Zone 1) and north (Zone 2) were selected. In addition, still smaller areas of sizes i.e., 0.5^o longitude x 0.5^o latitude grids representing coastal and offshore regions of the south (off Thiruvananthapuram), central (off Kozhikode) and north (off Karwar) regions were chosen to understand their regional scale variability. These areas were named as Grid 1 to 3 and suffixed 'a' and 'b' to demarcate coastal and offshore areas. Time series analysis revealed intra- and inter-annual variability on the three parameters with significant regional scale differences. In the Grid 1a to 3a, high Chl *a* (0.50-21.0 mg.m^{-3}) / K_d (0.05-1.50 m^{-1}) persists during the southwest monsoon and the magnitude of high values decrease towards north. Chl *a* / K_d variation was not that visible in the Grid 1b-3b, compared to Grid 1a-3a. High values of AOD also occurred in conjunction with high Chl *a* / K_d, but sustain for longer period (April – August). The supporting parameters showed low values of SST and faster southward current / wind during the southwest monsoon period. These are the indicative features of intense upwelling. In most of the cases, the month of lowest SSTs and faster southward currents coincided with the month of peak Chl *a* / K_d. Therefore, the increase in Chl *a* / K_d were attributed to enhanced upwelling as evident from the supporting parameters.

Significant positive and negative anomalies observed on Chl *a*, K_d and AOD. Chl *a* and K_d anomaly in the entire study area showed good influence to the concurrent mode of ENSO and IOD during August 2006 and August 2010. However, the influence was not evident during July 2001, when NIOD existed. In the Zone 1, one of the phases of ENSO and NIOD co-occurred with positive anomaly of Chl *a* / K_d. Similarly negative Chl *a* / K_d anomaly in the Zone 2, coincided with concurrent El Nino / PIOD. However, similar response of ENSO / IOD on AOD anomaly was not evident in the two zones from the present study. The underlying trend of the influence of ENSO / IOD on monthly anomalies of Chl *a* led to a detailed analysis using averages during July – September. Negative anomaly of Chl *a* coincided with concurrent El Nino / PIOD and positive with La Nina / NIOD modes. Thus, a strong response of ENSO and IOD in regulating Chl *a* values in the study area is observed.

The cases of co-occurrences of high / low AOD with corresponding high / low values of Chl *a* / K_d during certain years (August 2002 and 2007), were separated out and critically analysed utilising the HYSPLIT model, to understand the influence of aerosol source on these anomalies. The positive anomalies during August 2002 and negative anomalies during August 2007 were selected for the analysis. The aerosol trajectory computed from HYSPLIT model suggested that aerosols originating from Saudi Arabia and North east Africa had contributions to produce positive anomaly in the study areas. When inflow of these aerosols had come down, negative anomaly was produced. It is to be mentioned here that during the southwest monsoon period, significant iron dust prevails in the atmosphere over the Saudi Arabia and African Peninsula. Therefore, high iron content is expected over the study area during positive anomaly and low concentration during negative anomaly. This expectation was consistent with the observation from GOCART model, which simulated high iron content during positive anomaly periods. It is well known that high iron is favourable for enhancing primary production and has been already reported in various oceanic waters. The above observations suggest the importance of remote forcing of aerosol from Saudi Arabia and African Peninsula in producing high Chl *a* and thereby high productivity off the southwest coast of India.

EMD on Chl *a* / K_d /AOD brought out the existence of a few underlying oscillatory modes with periodicities ranging from nearly one to five years in the study areas.

The co-occurrence of high Chl *a* / K_d with low SST during the southwest monsoon period, strongly suggest that there exists an inverse relationship between them and this relationship can be utilised to develop empirical equations between them. Hence, regression analysis was carried out using Chl *a* / K_d from SeaWiFS and

SST from MODIS_AQUA in all the selected areas, which brought out an inverse relation between these parameters during the southwest monsoon period with significant spatial and temporal variability. Among the selected areas, relation is more visible and persists for longer duration towards south. The equations thus developed are applicable for each month and selected area during the southwest monsoon period. As the results were found encouraging ones, the experiments were repeated with *in situ* SST observations of eight data sets off Kochi (74.0^{o} E – 77.0^{o} E, 8.5 ^{o} N – 11.5 ^{o} N) representing various phases of upwelling between 1998 and 2009. However, due to cloud coverage, collocated points with respect to *in situ* SST on daily scale from satellite observations were too sparse during the southwest monsoon. Hence, time windows were widened to 3 day, 8 day, monthly and climatology to obtain sufficient number of collocated points to check the feasibility of the concept of developing empirical equations. Among the eight data sets, only during June 2009 data points were available for all these time windows. Good correlation was found to exist between SST and Chl *a* / K_d even during time windows of climatology. Moreover, error analysis revealed an error percentage < 1.5% for all these selected time windows of June 2009. The above factors suggest that even with the climatology data set, Chl *a* and K_d can be correlated with *in situ* observations on SST, when sufficient data points are not available from matching real time data. Further, the regression analysis and error estimates were carried out utilizing *in situ* SST and climatology of Chl *a* / K_d. Good inverse relation ($r^2 > 0.50$) between the parameter was observed during strong upwelling period and weak relation ($r^2 < 0.50$) during weak upwelling period. Even after taking the widest time window i.e. climatology, the error percentage in derived

SST with *in situ* were limited within 3.0 % and that too with < 1.5 % during most of the period. These results prompt to believe that monthly climatology of ocean colour data can also be utilised, when the real-time data are sparse.

The empirical relation between *in situ* SST and climatology of Chl *a* / K_d are utilised to invert SST from Chl *a* and K_d values. SSTs thus obtained showed similar pattern to that of *in situ* observations, when Chl *a* climatology (September 2007 and June 2009) also followed the pattern of *in situ* SST. Inversion of SST failed to reproduce the features when different patterns in the distributions of *in situ* SST and Chl *a* / K_d were seen (August 2007). Therefore, the present work displayed the feasibility of using even monthly climatology of Chl *a* / K_d in inverting back the SST, when similar distribution pattern exists for both the parameters. This further implies that there exists a specific equation for a specific pattern. In this case, the study brought out eight equations for eight different combinations of distribution patterns between SST and Chl *a*. In future, any of the real-time satellite ocean colour observation pattern matches with any of the observed one, already developed, respective equation can be utilized to obtain SST. Moreover, the study also encourages to develop more equations for the study area from concentrated filed programmes and satellite observations. Thus, the study implies the utilization of Chl *a* and K_d climatology to invert SST, when similar distribution pattern for *in situ* and Chl *a* prevails.

6.1. Future Scope

The present doctoral thesis reveals the possibility of using satellite ocean colour data to study the oceanographic / atmospheric features off the southwest coast of India, especially the upwelling phenomenon and its spatio-temporal variability. There is scope to refine those equations utilising systematic collection of *in situ* observations at closer spatial intervals for every month extending few years. In addition, regional variability on empirical relation can be examined utilising moored SST measurements and the collocated satellite ocean colour data. It will be worthwhile to know whether any such relation exists in other upwelling zones off the Indian coasts. Down the line, the method may find utility in fishery, weather forecasting, under water detection etc. as SST at closer spatial interval is a vital information in all the above fields.

AOD variability in the study area indicates the remote influence from the Arabian Peninsula and Saudi Arabia. This calls for further investigation with more *in situ* observations and modelling on the aerosol sources and constituents at various atmospheric levels.

It is to be noted that other oceanic feature such as fronts, eddies, meandering currents, sediment load, etc. leave signatures on ocean colour data. All these features have profound influence on the socio-economic spheres of human life. Therefore, studies on these features are required in future. The study also indicates the scope to derive high resolution SST from Chl *a* and K_d, which has profound influence on identifying potential fishing zones.

Considering finer spatial resolution of ocean colour sensors and availability of the same onboard Oceansat - 2, VIIRS, MODIS_AQUA, MODIS_TERRA etc. the study is relevant and can be thought of to utilise this sensor to understand and predict environmental dynamics, when information on closer spatial scale is required.

Reference

1. Ali M M (2003) Satellite altimetry for meteorological and oceanographic applications, *Mausam*, **54**, 205 – 214.

2. Arai Y, T Hirawake, T Odate, K Watanabe and M Fukuchi (2005) Distribution of chlorophyll a and sea surface temperature in the marginal ice zone (20^{o}E – 60^{o}E) in east Antarctica determined using summer multi-sensor remote sensing during austral summer, *Polar Bioscience*, **18**, 16 – 27.

3. Arnone R A (1987) Satellite-derived colour-temperature relationship in the Alboran Sea, *Remote Sensing of Environment*, **23**, 417 – 437.

4. Ashok K, Z Guan and Yamagata T (2001) Impact of the Indian Ocean Dipole on the relationship between the Indian Monsoon Rainfall and ENSO, *Geophysical Research Letters*, **28**, 4499 – 4502.

5. Ashok K, W L Chan, T Motoi, and T Yamagata (2004) Decadal Variability of the Indian Ocean Dipole, *Geophysical Research Letters,* **31**, doi:10.1029/2004GL021345.

6. Banse K (1959) On upwelling and bottom - trawling off the southwest coast of India, *Journal of Marine Biological Association of India*, **1**, 33 – 49.

7. Banse K (1987) Seasonality of phytoplankton chlorophyll in the central and northern Arabian Sea, *Deep Sea Research*, **34**, 713 – 723.

8. Banse K, Sumitra-Vijayaraghavan and M Madhupratap (1996) On the possible causes of seasonal phytoplankton blooms along the southwest coast of India, *Indian Journal of Marine Sciences*, **25**, 283-289.

9. Banse K and D C English (2000) Geographical differences in seasonality of CZCS derived phytoplankton pigment in the Arabian Sea for 1978-1986, *Deep-Sea Research II*, **47**, 1623-1677.

10. Barnard A H, P M Stegmann and J A Yoger (1997) Seasonal surface ocean variability in the South Atlantic Bight derived from CZCS and AVHRR imagery, *Continental Shelf Research*, **17(10)**, 1181-1206.

11. Beegum N S, K K Moorthy, S S Babu, R R Reddy, K R Gopal and Y N Ahmed (2009) Quasi-biennial oscillations in spectral aerosol optical depth, *Atmopheric Science Letters*, **10,** 279–284.

12. Behrenfeld M J, A J Bale, Z S Kolber, J Aiken and P G Falkowshi (1996) Confirmation of iron limitation of phytoplankton photosynthesis in the equatorial Pacific Ocean, *Nature*, **383**, 508 – 511.

13. Beletsky D, W P O'Connor, D J Schwab and D E Dietrich (1997) Numerical simulation of internal Kelvin waves and upwelling fronts, *Journal of Physical Oceanography*, **27**, 1197-1215.

14. Bhatla R, U C Mohanty and P V S Raju (2006) The variability of Indian Ocean surface meteorological fields during summer monsoon in El Nino / La Nina years, *Indian Journal of Marine Sciences*, **35(2)**, 93 -103.

15. Bless R C (1996) Discovering the cosmos, University Science Books, Sausalito, USA, 714 pp.

16. Boyd P W, A J Watson, C S Law, E R Abraham, T Trull, R Murdoch, D C E Bakker, A R Bowie, K O Buesseler, H Chang, M Charette, P Croot, K Downing, R Frew, M Gall, M Hadfield, J Hall, M Harvey, G Jameson, J LaRoche, M Liddicoat, R Ling, M T Maldonado, R M McKay, S Nodder, S Pickmere, R Pridmore, S Rintoul, K Safi, P Sutton, R Strzepek, K Tannenberger, S Turner, A Waite and J Zeldis (2000) A mesoscale phytoplankton bloom in the polar Southern Ocean stimulated by iron fertilization, *Nature*, **407**, 695–702.

17. Brandt P, L Stramma, F Schott, J Fischer, M Dengler and D Quadfasel (2002) Annual Rossby waves in the Arabian Sea from TOPEX / POSEIDON altimeter and *in-situ* data, *Deep Sea Research II*, **49**, 1197 – 1210.

18. Brown P C and L Hutchings (1987) The development and decline of phytoplankton blooms in the southern Benguela upwelling system. 1. Drogue movements, hydrography and bloom development, *South African Journal of Marine Science*, **5 (1)**, 357-391.

19. Bruce J G, J C Kindle, L H Kantha, J L Kerling and J F Bailey (1998) Recent observations and modeling in the Arabian Sea Laccadive high region, *Journal of Geophysical Research*, **103 (C4)**, 7593 – 7600.

20. Chandramohan P and B U Nayak (1992) Longshore sediment transport model for the Indian west coast, *Journal of Coastal Research*, **8**, 775-787.

21. Chase Z, A V Geen, P M Kosro, J Marra and P A wheeler (2002) Iron, nutrient and phytoplankton distributions in Oregon coastal waters, *Journal of Geophysical Research*, **107(C10)**, 3174, doi: 10.1029/2001JC000987.

22. Chauhan P, A Sahay, AS Rajawat, and S Nayak (2003) Remote sensing of diffuse attenuation coefficient (k490) using IRS-P4 ocean color monitor sensor, *Indian Journal of Marine Science*, **32**, 279–284,.

23. Chin M, R B Rood, S -J Lin, J -F Muller, A Thompson (2000) Atmospheric sulfur cycle simulated in the global model GOCART: model description and global properties, *Journal of Geophysical Research*, **105(D20)**, 24671–24687, doi:10.1029/2000JD900384.

24. Chin M, P Ginoux, S Kinne, O Torres, B Holben, B N Duncan, R V Martin, J Logan, A Higurashi, T Nakajima (2002) Tropospheric aerosol optical thickness from the GOCART model and comparisons with satellite and sun photometer measurements, *Journal of Atmospheric Sciences*, **59**, 461–483.

25. Conkright M E, T D O'Brien, C Stephens, R A Locarnini, H E Garcia, T P Boyer, J I Antonov, (2002) World Ocean Atlas 2001, Volume 6, Chlorophyll. Levitus S. (Ed.), NOAA Atlas NESDIS 54, U.S. Gov. Printing Office, Wash., D.C.**,** 46 pp.

26. Cox C and W Munk (1954) Measurement of the Roughness of the Sea Surface from Photographs of the Sun’s Glitter, *Journal of Optical Society of America*, **14**, 838–850.

27. Davis R E, R deSzoeke and P Niiler (1981) Variability in the upper ocean during MILE. Part II. Modeling the mixed layer response, *Deep Sea Research*, **28**, 1453 – 1475.

28. Demarcq H, R Barlow and F A Shillington (2003) Climatology and variability of sea surface temperature and surface chlorophyll in the Benguela and Agulhas regions as observed by satellite imagery, *African Journal of Marine Science,* **25**, 363-372.

29. Denman K L and M R Abbott (1994) Time scales of pattern evolution from cross-spectrum analysis of advanced very high resolution radiometer and coastal zone color scanner imagery, *Journal of Geophysical Research*, **99(C4)**, 7433 – 7442.

30. Doney S C, D M Glover, S J McCue and M Fuentes (2003) Mesoscale variability of Sea-viewing Wide Field-of-view Sensor (SeaWiFS) satellite ocean colour: global patterns and spatial scales, *Journal of Geophysical Research*, **108(C2)**, 3024, doi: 10.1029/2001JC000843.

31. Draxler R R and G D Hess (1998) An Overview of the HYSPLIT_4 Modelling System for trajectories, dispersion and deposition, *Australian Meteorological Magazine*, **47**, 295–308.

32. Duce R A and N M Tindale (1991) Atmospheric transport of iron and its deposition in the ocean, *Limnology and Oceanography*, **36**, 1715-1726.

33. Dudley B C and F J Wentz (2005) Global microwave satellite observations of sea surface temperature for numerical weather prediction and climate research, *American Meteorological Society*, doi: 10.1175/BAMS-86-8-1097.

34. Eker-Develi E, A E Kideys and S Tugrul (2006) Role of Saharan dust on phytoplankton dynamics in the northern Mediterranean, *Marine Ecology progress series*, **314**, 61 -75.

35. Evans R H and H R Gordon (1994) Coastal zone color scanner system calibration: a retrospective examination, *Journal of Geophysical*, **99,** 7293–7307.

36. Fan S, W J Moxim and H Levy II (2006) Aeolian inputs of bioavailable iron to the ocean, *Geophysical Research Letters,* **33(L07602)**, doi: 10.1029/2005GL024852.

37. Fitzwater S E, K H Coale, R M Gordon, K S Johnson, M E Ondrusek (1996) Iron deficiency and phytoplankton growth in the equatorial Pacific, *Deep Sea Research II*, **43**, 995 – 1015.

38. Frouin R, M Swindling and P Y Deschamps (1996) Spectral reflectance of sea foams in the visible and near-infrared: *in-situ* measurements and remote sensing implications, *Journal of Geophysical Research*, **101(14)**, 14361 – 14371.

39. Fu L, D B Chelton, Traon P L and R Morrow (2010) Eddy dynamics from satellite altimetry, *Oceanography*, **23(4)**, 14 – 25.

40. Ginoux P, M Chin, I Tegen, J M Prospero, B Holben, O Dubovik, S J Lin, (2001) Sources and distributions of dust aerosols simulated with the GOCART model, *Journal of Geophysical Research,* **106**, 20255-20274.

41. Ginoux P and O Torres (2003) Empirical TOMS index for dust aerosol: applications to model validation and source characterization, *Journal of Geophysical Research*, **108(D17)**, 4534, doi: 10.1029/2003JD003470.

42. Goes J I, H Gomes, A Kumar, A D Gouveia, V P Devassy, A H Parulekar and L V G Rao (1992) Satellite and ship studies of phytoplankton along the west coast of India, Oceanography of the Indian Ocean, Desai B. N. (Ed), 67 – 80.

43. Goes J I, P G Thoppil, Gomes H R and J T Fasullo (2005) Warming of the Eurasian landmass is making the Arabian Sea more productive, *Science*, **308**, 545-547.

44. Gordon H R and M Wang (1992) Surface roughness considerations for atmospheric correction of ocean colour sensors. 1: Rayleigh scattering component, Applied Optics, 31, 4247 – 4260.

45. Gordon H R and M Wang (1994) Retrieval of water-leaving radiance and aerosol optical thickness over the oceans with SeaWiFS: a preliminary algorithm, *Applied Optics*, **33 (3)**, 443-452.

46. Gordon H R (1997) Atmospheric correction of ocean color imagery in the Earth Observing System era, *Journal of Geophysical Research,* **102 (D14)**, 17081-17106.

47. Guan L and H Kawamura (2003) SST availabilities of satellite infrared and microwave measurements, *Journal of Oceanography*, **59**, 201-203.

48. Habeebrehman H, M P Prabhakaran, J Jacob, P Sabu, K J Jayalakshmi, C T Achuthankutty and C Revichandran (2008) Variability in biological responses influenced by upwelling events in the eastern Arabian Sea, *Journal of Marine Systems*, **74**, 545 – 560.

49. Haugen V E, O M Johannessen, and G Evensen (2002) Mesoscale modeling study of the oceanographic conditions off the southwest coast of India, *Proceeding of the Indian Academy of Sciences (Earth and Planetary Sciences)*, **111(3)**, 321 – 337.

50. He R, K Chen, T Moore and M Li (2010) Mesoscale variations of sea surface temperature and ocean colour patterns at the Mid-Atlantic Bight shelfbreak, *Geophysical Research Letters*, **37(L09607)**, doi: 10.1029/2010GL042658.

51. Hoepffner N and S Sathyendranath (1993) Determination of the major groups of phytoplankton pigments from the absorption spectra of total particulate matter, *Journal of Geophysical Research*, **98**, 22789 – 22803.

52. Hood R R, M R Abbott, A Huyer and P M Kosro (1990) Surface patterns in temperature, flow, phytoplankton biomass and species composition in the coastal transition zone off northern California, *Journal of Geophysical Research*, **95(C10)**, 18801 – 18094.

53. Hsu N C, R Gautam, A M Sayer, C Bettenhausen, C Li, M J Jeong, S -C Tsay and B N Holben (2012) Global and regional trends of aerosol optical depth over land and ocean using SeaWiFS measurements from 1997 to 2010, *Atmospheric Chemistry and Physics Discussions*, **12**, 8465-8501.

54. Huang B and Kinter III J L (2002) Interannual variability in the tropical Indian Ocean, *Journal of Geophysical Research*, **107(C11)**, 3199, doi: 10.1029/2001JC001278.

55. Huang N E, Z Shen, S R Long, M L C Wu, H H Shih, Q N Zheng, C C Tung and H H Liu (1998) The empirical mode of decomposition and the Hilbert spectrum for nonlinear and non-stationary time series analysis, *Proceedings of the Royal Society of London Series a – Mathematical Physical and Engineering Sciences*, **454**, 903 – 995.

56. Huang N E, M L C Wu, S R Long, S S P Shen, W D Qu, P Glersen and K L Fan (2003) A confidence limit for the empirical mode decomposition and Hilbert analysis, *Proceedings of the Royal Society of London Series a – Mathematical Physical and Engineering Sciences*, **459**, 2317 – 2345.

57. Hutchins D A, C E Hare, R S Weaver, Y Zhang, G F Firme, G R DiTullio, M B Alm, S F Riseman, J M Maucher, M E Geesey, C G Trick, G J Smith, E L Rue, J Conn and K W Bruland (2002) Phytoplankton iron limitation in the Humboldt current and Peru upwelling, *Limnology and Oceanography*, **47(4)**, 997 – 1011.

58. IOCCG (2000) Remote Sensing of ocean colour in coastal, and other optically-complex waters, Sathyendranath S. (Ed.), Reports of the International Ocean-Color Coordinating Group, No. 3, IOCCG, Darmouth, Canada.

59. IOCCG (2007) Ocean-Colour Data Merging, Grgg W. (Ed.), Reports of the International Ocean Colour Coordinating Group, no 6, IOCCG, Dartmouth, Canada.

60. Jayaram C, Neethu Chacko, Ajith Joseph K and Balchand A N (2010) Interannual Variability of Upwelling Indices in the Southeastern Arabian Sea: A Satellite Based Study, *Ocean Science Journal*, **45(1)**, 27 - 40.

61. Jayaram V C (2011) Remote sensing the signatures of upwelling in the southeastern Arabian sea, Ph. D. thesis, 159 pp.

62. Jickells T D, An Z S, Andersen K K, Baker A R, Bergametti G, Brooks N, Cao J J, Boyd P W, Duce R A, Hunter K A, Kawahata H, Kubilay N, la Roche J, Liss P S, Mahowald N, Prospero J M, Ridgwell A J, Tegen I and Torres R (2005) Global iron connections between desert dust, *Ocean Biogeochemistry and Climate Science*, **308**, 67-71.

63. Johannessen O M, G Subbaraju and J Blindheim (1987) Seasonal variation of oceanographic conditions off the southwest coast of India during 1971-1975, Fiskerdirektoratet Scripts Serial Havundersoekelser, **18**, 247 – 261.

64. Johnson G C, M J McPhaden and E Firing (2001) Equatorial Pacific ocean horizontal velocity, divergence, and upwelling, *Journal of Physical Oceanography*, **31**, 839-849.

65. Johnson K S, F P Chavez, V A Elrod, S E Fitzwater, J T Pennington, K R Buck and P M Watlz (2001) The annual cycle of iron and biological response in the central California coastal waters, *Geophysical Research Letters,* **28**, 1247 – 1250.

66. Kahru M, R M Kudela, M Manzano-Sarabia, B. G. Mitchell (2012) Trends in the surface chlorophyll of the California Current: Merging data from multiple ocean color satellites, Deep-Sea Research Part II: Topical studies in Oceanography, **77-80**, 89-98.

67. Kane R P (1992) Relationship between QBOs of stratospheric winds, ENSO variability and other atmospheric parameters, *International Journal of Climatology,* **12**, 435–447.

68. Karisiddaiah S M and M Veerayya (2002) Occurrence of pockmarks and gas seepages along the central western continental margin of India, *Current Science*, **82**, 52- 57.

69. Kelkar R R (2007) Satellite Meteorology, BS Publications, 267 pp.

70. Khan T M A, F A Khan and R Jilani (2008) Sea surface temperature variability along Pakistan coast and its relation to El Nino – Southern Oscillation, *Journal of Basic and applied Sciences,* **4(2)**, 67-72.

71. King A L and K A Barbeau (2007) Evidence for phytoplankton iron limitation in the southern California Current System, *Marine Ecology Progress Series*, **342**, 91 – 103.

72. Kirk J T O (1994) Light and photosynthesis in aquatic ecosystems, Cambridge University press, Cambridge, 509 pp.

73. Krishna K M (2008) Coastal upwelling along the southwest coast of India – ENSO modulation, *Ocean Science Discussions*, **4**, 123 – 134.

74. Kumar P V H and K V Sanilkumar (2005) Long period waves in the coastal regions of the north Indian Ocean, *Indian Journal of Marine Sciences*, **33(2)**, 150 – 154.

75. Kumar S P, J Narvekar, A Kumar, C Shaji, P Anand, P Sabu, G Rijomon, J Jossia, K A Jayaraj, A Radhika and K K C Nair (2004) Intrusion of the Bay of Bengal water into the Arabian Sea during winter monsoon and associated chemical and

biological response, *Geophysical Research Letters*, **31(L15304)**, doi: 10.1029/2004GL020247.

76. Kumari B and K N Babu (2009) Provincial nature of chlorophyll and sea surface temperature observed by satellite, *International journal of Remote Sensing*, **30(4)**, 1091 – 1097.

77. Li F and V. Ramanathan (2002) Winter to summer monsoon variation of aerosol optical depth over the tropical Indian Ocean, Journal of Geophysical Research, **107(D16)**, 4284, doi: 10.1029/2001JD000949.

78. Lluch-cota S (2000) Coastal upwelling in the eastern Gulf of California, *Oceanologica Acta*, **23(6)**, 731 – 740.

79. Luis A J and H Kawamura (2004) Air-sea interaction, coastal circulation and biological production in the eastern Arabian Sea: a review, *Journal of Oceanography*, **60**, 205 – 218.

80. Madhupratap M, K N V Nair, T C Gopalakrishnan, P Haridas, K K C Nair, P Venugopal and M Gauns (2001) Arabian Sea oceanography and fisheries of the west coast of India, *Current Science*, **81(4)**, 355-361.

81. Mahowald N, A Baker, G Bergametti, N Brooks, R Duce, T Jickells, N Kubilay, J Prospero, I Tegen (2005) Atmospheric global dust cycle and iron inputs to the ocean, *Global Biogeochemical Cycles*, **19**, GB4025, doi: 10.1029/2004GB002402.

82. Mahowald N M, S Engelstaedter, C Luo, A Sealy, P Artaxo, C Benitez-Nelson, S Bonnet, Y Chen, P Y Chuang, D D Cohen, F Dulac, B Herut, A M Johansen, N Kubilay, R Losno, W Maenhaut, A Patyan, J M Prospero, L M Shank and R L Siefert (2009) Atmospheric iron deposition: global distribution, variability and human perturbations, *Annual Review of Marine Science*, **1**, 245-278.

83. Mandal T K, A Khan, Y N Ahammed, R S Tanwar, R S Parmar, K S Zalpuri, P K Gupta, S L Jain, R Singh, A P Mitra, S C Garg, A Suryanarayana, V S N Murty, M D Kumar and A J Shepherd (2006) Observations of trace gases and aerosols over the Indian Ocean during the monsoon transition period, *Journal of Earth System Science*, **115(4)**, 473–484.

84. Martin J H, and R M Gordon (1988) Northeast Pacific iron distributions in relation to phytoplankton productivity, *Deep Sea Research*, **35**, 177– 196.

85. Martin J H, R M Gordon, S Fitzwater and W W Broenkow (1989) VERTEX: phytoplankton / iron studies in the Gulf of Alaska, *Deep Sea Research*, **36(5)**, 649 – 680.

86. Martin S (2004) An introduction to ocean remote sensing, Cambridge University press, Cambridge, 427 pp.

87. Mathew B (1983) Studies on upwelling and sinking in the seas around India, Ph. D. thesis, Cochin University of Science and Technology, 159 pp.

88. Matondkar S P G, R M Dwivedi, S Parab, S Pednekar, E S Desa, A Mascarenhas, M Raman and S K Singh (2006) Satellite and ship studies of phytoplankton in the northeastern Arabian during 2000-2006 period, *Proceedings of SPIE*, **6406**, doi: 10.1117/112.693693.

89. McCreary J P, P K Kundu and R Molinari (1993) A numerical investigation of dynamics, thermodynamics and mixed-layer processes in the Indian Ocean, *Progress in Oceanography*, **31**, 181–244.

90. McDonald A J, A J G Baumgaertner, G J Fraser, S E George and S Marsh (2007) Empirical Mode Decomposition of the atmospheric wave field, *Annales Geophysicae*, **25**, 375 – 384.

91. Miles T N and R He (2010) Temporal and spatial variability of Chl ‘a’ and SST on the south Atlantic Bight: revisiting with cloud-free reconstructions of MODIS satellite imagery, *Continental Shelf Research*, **30**, 1951 – 1962.

92. Miller C B, B W Frost, P A Wheeler, M R Landry, N Welschmeyer and T M Powell (1991) Ecological dynamics in the subartic Pacific, a possibly iron-limited ecosystem, *Limnology and Oceanography*, **36**, 1600 – 1615.

93. Mobley C D (1994) Light and water: radiative transfer in natural waters, Academic press, 592 pp.

94. Moore C M, M M Mills, A Milne, R Langlois, E P Achterberg, K Lochte, R J Geider and Roche J L (2006) Iron limits primary productivity during spring bloom development in the central North Atlantic, *Global Change Biology*, **12(4)**, 626 – 634.

95. Moorthy K, S K Satheesh and B V K Murthy (1997) Investigation of marine aerosol over the tropical Indian Ocean, *Journal of Geophysical Research,* **102**, 18827-18842.

96. Muller J L, G S Fargion and C R McClain (Eds.) (2003) Ocean optics protocols for satellite ocean colour sensor validation, special topics in ocean optics protocols and appendices, Ocean optics protocols for satellite ocean colour sensor validation, revision 4, volume VI, Greenbelt, Maryland.

97. Muller-Karger F E, J J Walsh, Evans R H and M B Meyers (1991) On the seasonal phytoplankton concentration and sea surface temperature cycles of the gulf of Mexico as determined by satellite, *Journal of Geophysical Research,* **96(C7)**, 12645 – 12665, doi: 10.1029/91JC00787.

98. Nair S K, S Sijikumar and S S Prijith (2012) Impact of continental meteorology and atmospheric circulation in the modulation of Aerosol Optical Depth over the Arabian Sea, *Journal of Earth System Science,* **121(2)**, 263 – 272.

99. Palenzuela J M T, M M S Cuadrado, T L Doval (2002) Remote Sensing of Chlorophyll and Temperature in Coastal Upwelling System, In: Observing our Environment from Space: New Solutions for a New Millennium. G Begni and A. A. Balkema (Eds.), ISBN 9058092542, 73-77.

100. Patra P K, M. D. Kumar, N Mahowald, V V S S Sarma (2006) Atmospheric deposition and surface stratification as controls of contrasting chlorophyll abundance in the north Indian Ocean, *Journal of Geophysical Research*, **112(C05029)**, doi: 10.1029/2006JC003885.

101. Patti B, C Guisande, A R Vergara, I Riveiro, I Maneiro, A Barreiro, A Bonanno, G Buscaino, A Cuttitta, G Basilone and S Mazzola (2008) Factors responsible for the differences in satellite-based chlorophyll a concentration between the major global upwelling areas, *Estuarine Coastal and Shelf Science*, **76**, 775 – 786.

102. Perez V, E Fernandez, E Maranon, P Serret and C Garcia-Soto (2005) Seasonal and inter-annual variability of chlorophyll a and primary production in the equatorial Atlantic: *in-situ* and remote sensing observations, *Journal of Plankton Research*, **27(2)**, 189-197.

103. Polovina J L, E A Howell and M Abecassis (2008) Ocean’s least productive waters are expanding, *Geophysical Research Letters*, **35**, L03618, doi: 10.1029/2007GL031745.

104. Pond S and G L Pickard (2007) Introductory dynamical oceanography, second edition, Pergamon Press, 329 pp.

105. Pradhan Y, A S Rajawat and S Nayak (2004) Application of IRS-P4 OCM data to study the impact of tidal propagation on sediment dynamics in the Gulf of Kachchh, *Indian Journal of Marine Sciences,* **33(2)**, 129-137.

106. Pranowo W S, B Hendrajana, A Supangatm (2003) Temperature and Ocean Primary Productivity Correlation in the Indian Ocean (South Java Sea). Presented at 1st Argo Science Workshop. Principal sponsors JAMSTEC and NOAA. Tokyo, November 12 – 14.

107. Prasad J S, A S Rajawat, Y Pradhan, O S Chauhan and S R Nayak (2002) Retrieval of sea surface velocities using sequential ocean colour Monitor (OCM) data, *Journal of Earth System Science*, **111(3)**, 189 – 195.

108. Priju C P and A C Narayana (2007) Heavy and trace metals in vembanad lake sediments, *International Journal of Environmental Research*, **1**, 280-289.

109. Rajeev K, V Ramanathan and J Meywerk (2000) Regional aerosol distribution and it long-range transport over the Indian Ocean, *Journal of Geophysical Research*, **105**, 2029 – 2043.

110. Rao R R, M S G Kumar, M Revichandran, A R Rao, V V Gopalakrishna and P Thadathil (2009) Inter-annual variability of Kelvin wave propagation in the wave guides of the equatorial Indian Ocean, the coastal Bay of Bengal and the southeastern Arabian Sea during 1993 – 2006, *Deep-Sea Research part I: Oceanographic Research Papers*, **57(1)**, 1-13.

111. Rao V P and B R Rao (1995) Provenance and distribution of clay minerals in the sediments of the western continental shelf and slope of India, *Continental Shelf Research*, **15**, 1757-1771.

112. Rasch P J, W D Collins and B E Eaton (2001) Understanding the Indian Ocean Experiment (INDOEX) aerosol distributions with an aerosol assimilation, *Journal of Geophysical Research*, **106(D7)**, 7337 – 7355.

113. Rees W G (2005) Physical principles of remote sensing, second edition, Cambridge University press, 343 pp.

114. Richard E T and I V Fine (2003) Estimating mixed layer depth from oceanic profile data, *Journal of Atmospheric and Oceanic Technology*, **20**, 319 – 329.

115. Rilling G, P Flandarin and P Gonclaves (2003) On Empirical Mode Decomposition and its algorithms, in IEEE-EURASIP Workshop on nonlinear signal and image processing – NSIP-03, Grado, Italy.

116. Ryther J H, J R Hall, A K Pease, A Bakun and M M Jones (1966) Primary production in relation to the chemistry and hydrography of the western Indian Ocean, *Limnology and Oceanography*, **11(3)**, 371 - 380.

117. Saji N H, B N Goswami, P N Vinayachandran and T Yamagata (1999) A Dipole Mode in the tropical Indian Ocean, *Nature*, **401**, 360–363.

118. Saji N H and T Yamagata (2003) Possible Impacts of the Indian Ocean Dipole Mode Events on global climate, *Climate Research*, **25**, 151–169.

119. Sanilkumar K V, V K Unni and V V James (2004) Upwelling characteristics off the southwest coast of India during 2003, *Proceeding of the National Symposium on emerging trends in the fields of Meteorology and Oceanography (METOC-2004)*, held at Cochin during February 2004, 137 – 143.

120. Sanilkumar K V and P V H Kumar (2005) Eddies and planetary waves in the central Arabian Sea, *Journal of the Indian Society of Remote Sensing*, **33(1)**, 137 – 146.

121. Sanilkumar K V, S Shalin, C V K P Rao, P A Umesh, A R Rao, K Mehta, K N Babu and A K Shukla (2011) Validation of OCM 2 geophysical products in the western and eastern Indian coastal waters, presented at First International conference meeting on utilisation of Oceansat – 2 held at Space Application Centre, Ahmedabad during March 2011.

122. Sankar S, M R R Kumar and C Reason (2010) On the relative roles of El Nino and Indian Ocean dipole events on the monsoon onset over Kerala, *Theoretical and Applied Climatology*, **103**, 359-374.

123. Santos A M J (2010) Influence of Saharan aerosols on phytoplankton biomass in the tropical north Atlantic Ocean, Ph. D. thesis, University of Puerto Rico, 88 pp.

124. Saraceno M, C Provost and A R Piola (2005) On the relationship between satellite-retrieved surface temperature fronts and chlorophyll a in the western South Atlantic, *Journal of Geophysical Research*, **110(C11016)**, doi: 10.1029/2004JC002736

125. Sarangi R K, P Chauhan and S R Nayak (2005) Inter-annual variability of phytoplankton blooms in the northern Arabian Sea during winter monsoon period (February – March) using IRS-P4 OCM data, *Indian Journal of Marine Sciences*, **34(2)**, 163 – 173.

126. Sarma V V S S, M D Kumar, M D George and A Rajendran (1996) Seasonal variability in inorganic carbon components in the central and eastern Arabian Sea, *Current Science*, **71,** 852–856.

127. Sarma V V S S, M D Kumar, M Gauns and M Madhupratap (2000) Seasonal controls on surface pCO2 in the central and eastern Arabian Sea, *Proceeding of Indian Academy of Science (Earth and Planetary Science)*, **109,** 471–479.

128. Sarma V V S S (2006) The influence of Indian Ocean Dipole (IOD) on biogeochemistry of carbon in the Arabian Sea during 1997 – 1998, *Journal of Earth System Science*, **115(4)**, 433 – 450.

129. Sayer A M, N C Hsu, C Bettenhausen, Z Ahmad, B N Holben, A Smirnov, G E Thomas and J Zhang (2012) SeaWiFS Ocean Aerosol Retrieval (SOAR): algorithm, validation and comparison with other data sets, *Journal of Geophysical Research*, **117(D03206)**, doi: 10.1029/2011JD016599.

130. Shaji C and A Gangopadhyay (2007) Synoptic modeling in the eastern Arabian Sea during the southwest monsoon using upwelling feature models, *Journal of Atmospheric and Oceanic Technology*, **24**, 877-893.

131. Shalin S and K V Sanilkumar (2013) Climatic oscillations in aerosol optical depth over tropical oceanic regions pertaining to genesis of the Indian Ocean Dipole, *International Journal of Remote Sensing*, **34(1)**, 86-95.

132. Shankar D and S R Shetye (1997) On the dynamics of the Lakshadweep high and low in the southeastern Arabian Sea, *Journal of Geophysical Research*, **102(C6)**, 12551 – 12562.

133. Shankar D, P N Vinayachandran and A S Unnikrishnan (2002) The monsoon currents in the north Indian Ocean, *Progress in Oceanography*, **52**, 63-120.

134. Sharma GS (1978) Upwelling off the southwest coast of India, *Indian Journal of Marine Science*, **7**, 8-19.

135. Shetye S R (1984) Seasonal variability of the temperature field off the southwest coast of India, *Proceedings of Indian Academy of Sciences (Earth and Planetary Sciences)*, **93**, 399 – 411.

136. Shetye S R, S S C Shenoi, M K Antony and V Krishna Kumar (1985) Monthly mean wind stress along the coasts of the Indian Ocean, *Proceedings of Indian Academy of Sciences (Earth and Planetary Sciences)*, **97**, 53 – 62.

137. Shetye S R and S S C Shenoi (1988) Seasonal cycle of surface circulation in the coastal northern Indian Ocean, *Proceedings of Indian Academy of Sciences (Earth and Planetary Sciences)*, **97**, 53 – 62.

138. Shetye S R, A D Gouveia, S S C Shenoi, D Sundar, G S Michael, A M Almeida and K Santanam (1990) Hydrography and circulation off the west ocast of India during the southwest monsoon 1987, *Journal of Marine Research*, **48**, 359 – 378.

139. Sholkovitz E R, P N Sedwick and T M Church (2009) Influence of anthropogenic combustion emissions on the deposition of soluble iron to the ocean: empirical estimates for island sites in the north Atlantic, *Geochimica et Cosmochimia Acta*, **73**, 3981 – 4003.

140. Siefert R L, A M Johansen, M R Hoffmann (1999) Chemical characterization of ambient aerosol collected during the southwest monsoon and intermonsoon seasons

over the Arabian Sea: Labile-Fe(II) and other trace metals, *Journal of Geophysical Research*, **104(D3)**, 3511-3526.

141. Signorini S R and C R McClain (2012) Subtropical gyre variability as seen from satellites, *Remote Sensing Letters*, **3(6)**, 471 – 479.

142. Smyth T J, P I Miller, S B Groom, S J Lavender (2001) Remote sensing of sea surface temperature and chlorophyll during Lagrangian experiments at the Iberian margin, *Progress in Oceanography*, **51**, 269 -281.

143. Solanki H U, R M Dwivedi, S R Nayak, J V Jadeja, D B Thakar, H B Dave and M I Patel (2001) Application of ocean colour monitor chlorophyll and AVHRR SST for fishery forecast: preliminary validation results off Gujarat coast, northwest coast of India, *Indian Journal of Marine Sciences*, **30**, 132 – 138.

144. Solanki H U, R M Dwivedi, S R Nayak, V S Somvanshi, D K Gulati and S K Pattnayak (2003) Fishery forecast using OCM chlorophyll concentration and AVHRR SST: validation results off Gujarat coast, India, *International Journal of Remote Sensing*, **24(18)**, 3691-3699.

145. Stegmann P M and D S Ullman (2004) Variability in chlorophyll and sea surface temperature fronts in the Long Island Sound outflow region from satellite observations, *Journal of Geophysical Research*, **109(C07S03)**, doi:10.1029/2003JC001984.

146. Takeda S, A Kamatani, K Kawanobe (1995) Effects of nitrogen and iron enrichments on phytoplankton communities in the northwestern Indian Ocean, *Marine Chemistry*, **50**, 229 – 241.

147. Tassan S (1994) Local algorithms using SeaWiFS data for the retrieval of phytoplankton, pigments, suspended sediment, and yellow substance in coastal waters, *Applied Optics*, **33(12)**, 2369-2378.

148. Tatavarti R and A C Narayana (2006) Hydrodynamics in a mudbank regime during non-monsoon and monsoon seasons, *Journal of Coastal Research*, **22(6)**, 1463 – 1473.

149. Taylor J R and R Ferrari (2011) Ocean fronts trigger high latitude phytoplankton blooms, *Geophysical Research Letters*, **38**, L23601, doi:10.1029/2011GL049312.

150. Trenberth K E (1997) The definition of El Nino, *Bulletin of the American Meteorological Society*, **78**, 2771 – 2777.

151. Varma P U and P G Kurup (1969) Formation of the Chakara (mud bank) on the Kerala coast, *Current Science*, **38**, 559- 560.

152. Varotsos C and D Kirk-Davidoff (2006) Long-memory processes in ozone and temperature variations at the region 60^oS – 60^oN, *Atmospheric Chemistry and Physics*, **6**, 4093 – 4100.

153. Walker N D, R R Leben and S Balasubramanian (2005) Hurricane-forced upwelling and chlorophyll a enhancement within cold-core cyclones in the Gulf of Mexico, *Geophysical Research Letters*, **32(L18610)**, doi: 10.1029/2005GL023716.

154. Wang M and H R Gordon (1994) A simple, moderately accurate, atmospheric correction algorithm for SeaWiFS, *Remote Sensing of Environment*, **50**, 231-239.

155. Wang M and S Bailey (2001) Correction of the sun glint contamination on the SeaWiFS ocean and atmosphere products, *Applied Optics*, **40**, 4790 – 4798.

156. Wang M (2002) The Rayleigh lookup tables for the SeaWiFS data processing: accounting for the effects of ocean surface roughness, *International Journal of Remote sensing*, **23(13)**, 2693-2702.

157. Watts L J, B Kumari and H Maass (2005) Applications of remotely-sensed ocean colour data in the Arabian Sea – a review, *Indian Journal of Marine Sciences*, **34(4)**, 396 – 407.

158. Weiss R F (1974) Carbon dioxide in water and seawater: The solubility of a non-ideal gas, *Marine Chemistry*, **2,** 23–25.

159. Wells M L, N M Price, K W Bruland (1995) Iron chemistry in sea water and its relationship to phytoplankton: a workshop report, *Marine Chemistry*, **48**, 157 – 182.

160. White W B (2000) Coupled Rossby waves in the Indian Ocean on interannual timescales, *Journal of Physical Oceanography*, **30**, 2972 – 2988.

161. Wiggert J D, R R Hood, K Banse and J C Kindle (2005) Monsoon-driven biogeochemical processes in the Arabian Sea, *Progress in Oceanography*, **65**, 176-213.

162. Wiggert J D and Murtugudde R G (2007) The sensitivity of the southwest monsoon phytoplankton bloom to variations in aeolian iron deposition over the Arabian Sea, *Journal of Geophysical Research*, **112**, doi: 10.1029/2006JC003514.

163. Wilkerson F P, A M Lassiter, R C Dugdale, A Marchi and V E Hogue (2006) The phytoplankton bloom response to wind events and upwelled nutrients during the CoOP WEST study, *Deep Sea Research Part II: Topical Studies in Oceanography*, **53**(25-26), 3023 – 3048.

164. Witter A E, B L Lewis, G W Luther III (2000) Iron speciation in the Arabian Sea, *Deep-Sea Research II*, **47**, 1517 – 1539.

165. Wu R and B P Kirtman (2007) Understanding the impacts of the Indian Ocean on ENSO variability in a coupled GCM, *Journal of Climate*, **17**, 4019–4031.

166. Wunsch C and Stammer D (1998) Satellite altimetry, the marine geoid, and the oceanic general circulation, *Annual Review of Earth and Planetary Science*, **26**, 219-253.

167. Yang J, L Yu, C J Koblinsky and D Adamec (1998) Dynamics of the seasonal variations in the Indian Ocean from TOPEX / POSEIDON sea surface and an ocean model, *Geophysical Research Letters*, **25(11)**, 1915 – 1918.

168. Yoder J A, Schollaert S E and J E O'Reilly (2002) Climatological phytoplankton chlorophyll and sea surface temperature patterns in continental shelf and slope waters off the northeast US coast, *Limnology and Oceanography*, **47(3)**, 672.

169. Young R W, K L Carder, P R Betzer, D K Costello, R A Duce, G R DiTullio, N W Tindale, E A Lawa, M Vematsu, J T Merril and R A Feely (1991) Atmospheric iron inputs and primary productivity: phytoplankton responses in the north Pacific, *Global Biogeochemical Cycles*, **5**, 119 – 134.

170. Yuan-Jian Y, X Tao, S Liang and F Yun-Fei (2012) Summer monsoon impacts on chlorophyll a concentration in the middle of the south china sea: climatological mean and annual variability, *Atmospheric and Oceanic Science Letters*, **5(1)**, 15-19.

171. Zhu A, V Ramanathan, F Li and D Kim (2007) Dust plumes over the Pacific, Indian and Atlantic oceans: climatology and radiative impact, *Journal of Geophysical Research*, **112**, D16208, doi: 10.1029/2007JD008427.

List of publications by the author

International Journal

1. **Shalin S** and K V Sanilkumar (2013) Climatic oscillations in aerosol optical depth over the tropical oceanic regions pertaining to the genesis of Indian Ocean Dipole, *International Journal of Remote Sensing*, **34(1)**, 86-95.

National Journal

2. **Shalin S**, K V Sanilkumar, C A Babu and C V K Prasada Rao (2012) Response of aerosol optical depth to the general cycle of global climate in the western and eastern Indian Ocean, *Sea Tech*, **9(1)**, 17-20.

Conference

3. **Shalin S**, K V Sanilkumar and C V K Prasada Rao (2010) Studies on regional characteristics off Kochi and Visakhapatnam utilizing the ocean colour sensors of SeaWiFS and MODIS, Presented on National symposium on 'Nowcasting to forecasting – needs and challenges for Naval operations' held on Kochi during Nov 2010.
4. K V Sanilkumar, **Shalin S**, C V K Prasada Rao, P A Umesh, A R Rao, K B Mehta, K N Babu and A K Shukla (2010) Validation of OCM 2 geophysical products in the western and eastern Indian coastal waters, Scientific report presented at International meeting on utilization of Oceansat – 2 held at Space Application Centre, Ahmedabad during March 2011.
5. **Shalin S**, K V Sanilkumar, C A Babu and C V K Prasada Rao (2011) Response of aerosol optical depth to the general cycle of global climate in the western

and eastern Indian Ocean, Presented at OSICON'11 held at NIOT, Chennai during July 2011.

6. K V Sanilkumar, **Shalin S**, G N Rao and C V K Prasada Rao (2012) Empirical relation between *in-situ* SST and Ocean Colour Sensor data off the southwest coast of India during the upwelling period, PORSEC 2012 (under submission).

7. **Shalin S** and KV Sanilkumar (2012) Variability in chlorophyll 'a' at coastal and offshore areas off the Southwest coast of India, PORSEC 2012 (under submission).

8. **Shalin S** and K V Sanilkumar (2012) Temporal variability of aerosol optical depth over coastal area off the southwest coast of India, PORSEC 2012 (under submission).

9. **Shalin S**, K V Sanilkumar and K N Babu (2012) Empirical relation between diffuse attenuation coefficient and beam attenuation coefficient off Kochi, PORSEC 2012 (under submission).

Report

10. Sanilkumar K V, **Shalin S**, C V K Prasada Rao, A K Shukla, K N Babu and K B Mehta (2010) Preparatory studies for validation of Ocean Colour Monitor-2 of Oceansat-2 with sea-truth measurement, NPOL-RR/62/2010.